

1
2

CONNECTING OBSERVED MICROBURST PRECIPITATION WITH ITS
SCATTERING MECHANISM

3

by

Mykhaylo Sergeevich Shumko

4

A dissertation submitted in partial fulfillment
of the requirements for the degree

of

Doctor of Philosophy

in

Physics

5

MONTANA STATE UNIVERSITY
Bozeman, Montana

October 2019

6

7

©COPYRIGHT

8

by

Mykhaylo Sergeevich Shumko

2019

All Rights Reserved

DEDICATION

⁹ I dedicate this to all MSU students who use L^AT_EX. Dedication is optional
¹⁰ and may be no longer than one page, single spaced, and should precede the
¹¹ acknowledgments page.

ACKNOWLEDGEMENTS

¹² I would like acknowledge the countless engineers, technicians, and scientists who
¹³ made the FIREBIRD, AC-6, and RBSP missions a success. This work was supported
¹⁴ by Montana State University and by NASA Headquarters under the NASA Earth and
¹⁵ Space Science Fellowship Program - Grant 80NSSC18K1204. **Add co-author support.**

TABLE OF CONTENTS

16	1. INTRODUCTION	1
17	Charged Particle Motion in Electric and Magnetic Fields	2
18	Particle Populations and Their Interractions in the Magnetosphere	8
19	Inner Magnetosphere Populations.....	11
20	Plasmasphere.....	13
21	Ring Current	15
22	Radiation Belts.....	16
23	Radiation Belt Particle Sources and Sinks	20
24	Adiabatic Heating	20
25	Wave Resonance Heating	21
26	Particle Losses	23
27	Microbursts	26
28	Scope of Reserach	29
29	2. CHAPTER TWO	
30	EVIDENCE OF MICROBURSTS OBSERVED NEAR THE EQUA-	
31	TORIAL PLANE IN THE OUTER VAN ALLEN RADIATION	
32	BELT	31
33	Contribution of Authors and Co-Authors	31
34	Manuscript Information	32
35	Key Points	33
36	Abstract	33
37	Introduction	33
38	Spacecraft Instrumentation	35
39	Observations	37
40	Analysis	41
41	Microburst and Source PSD	41
42	Motion of resonant electrons in phase space	43
43	Comparing the microburst PSD to diffusion theory	46
44	Discussion and Conclusions	47
45	Acknowledgments	49
46	3. CHAPTER THREE	
47	MICROBURST SCALE SIZE DERIVED FROM MULTIPLE BOUNCES	
48	OF A MICROBURST SIMULTANEOUSLY OBSERVED WITH	
49	THE FIREBIRD-II CUBESATS	50
50	Contribution of Authors and Co-Authors	50

TABLE OF CONTENTS – CONTINUED

51	Manuscript Information	51
52	Key Points	52
53	Abstract	52
54	Introduction	53
55	Spacecraft and Observation	55
56	Analysis.....	58
57	Electron Bounce Period	58
58	Microburst Energy Spectra	61
59	Microburst Scale Sizes	61
60	Discussion and Conclusions	64
61	Acknowledgments	66
62	4. CONCLUSION	67
63	REFERENCES CITED.....	68
64	APPENDIX: Appendix A	77
65	APPENDIX: Appendix B	80
66	Time and position correction	80

LIST OF FIGURES

Figure	Page
67 1.1 The three periodic motions of charged particles 68 in Earth's dipole magnetic field. These motions 69 are: gyration about the magnetic field line, bounce 70 motion between the magnetic poles, and azimuthal 71 drift around the Earth. Figure from (Baumjohann 72 and Treumann, 1997).	2
73 1.2 Charged particle motion in a uniform magnetic field 74 \vec{B} . Panel (A) shows the geometry defining the 75 pitch angle, α . Panel (B) and (C) show two helical 76 electron trajectories with dashed lines assuming a 77 large and small α (corresponding to a small and large 78 parallel velocity $v_{ }$), respectively.	6
79 1.3 Contours of constant gyration, bounce, and drift 80 frequencies for electrons and protons in a dipole field. 81 Figure from Schulz and Lanzerotti (1974).	7
82 1.4 Macroscopic structures in the outer magnetosphere. 83 The solar wind with its frozen-in interplanetary 84 magnetic field is shown on the left and is traveling 85 supersonically towards the right. The solar wind 86 envelops Earth's magnetic field to create the mag- 87 netosphere cavity. Since the solar wind is traveling 88 supersonically, it creates a bow shock up stream. 89 Downstream of the bow shock the shocked solar wind 90 plasma inside the magnetosheath flows around the 91 magnetopause, a boundary between the solar wind 92 and magnetosphere. Figure from Baumjohann and 93 Treumann (1997).	9
94 1.5 Macroscopic structures in the inner magnetosphere 95 most relevant to this dissertation. The plasmas- 96 sphere, and the radiation belts are shown and ring 97 current is co-located there as well. Sun is to the left. 98 Figure from Baumjohann and Treumann (1997).	10
99 1.6 The series of steps involved in magnetic reconnection 100 with a southward IMF. Figure from Baumjohann 101 and Treumann (1997).	12

LIST OF FIGURES – CONTINUED

Figure	Page
102 1.7 Equipotential lines and electric field arrows due to 103 the superposition of the co-rotation and convection 104 electric fields. Electrons in the shaded region execute 105 closed orbits. Outside of the shaded regions the 106 electrons are not trapped and will escape. The 107 region separating the two regimes is called the Alfvén 108 layer. Figure from Baumjohann and Treumann (1997).....	14
109 1.8 The DST index during the St. Patrick's Day 2015 110 storm. This storm was caused by a coronal mass 111 ejection on March 15th, 2015. The storm phases 112 are: initial phase, main phase, and recovery phase. 113 The initial phase occurred when the Dst peaked at 114 +50 nT on March 17th during which the ring current 115 was eroded by the coronal mass ejection during the 116 interval shown by the red bar. Then the rapid 117 decrease to ≈ -200 nT was during the main phase 118 where many injections from the magnetotail pumped 119 up the ring current which reduced Earth's magnetic 120 field strength at the ground and is shown with the 121 green bar. Lastly, the recovery phase lasted from 122 March 18th to approximately March 29th during 123 which the ring current particles were lost and the 124 ring current returned to its equilibrium state. The 125 recovery phase is shown with the blue bar.....	17
126 1.9 The two radiation belts with a the locations of 127 various satellites and orbits. Figure from (Horne 128 et al., 2013).	18
129 1.10 The dynamics of the outer radiation belt in 1997 130 from the POLAR satellite. Top panel shows the 1.2- 131 2.4 MeV electron flux as a function of L and 1997 day 132 of year. The middle panel shows the DST index, and 133 bottom panel shows the solar wind velocity. Figure 134 from (Reeves et al., 2003).	19

LIST OF FIGURES – CONTINUED

Figure	Page
135 1.11 The trajectories of an electron and a right-hand cir- 136 cularly polarized wave during a cyclotron resonance. 137 The electron's v_{\parallel} and the wave's k_{\parallel} are in opposite 138 directions such that the wave's frequency is Doppler 139 shifted to a integer multiple of the electron cyclotron 140 frequency. Figure from (Tsurutani and Lakhina, 1997).	22
141 1.12 Various wave modes in the magnetosphere. Ultra 142 low frequency waves occur throught the magneto- 143 sphere. Chorus waves are typically observed in 144 the 0-12 midnight-dawn region. EMIC waves are 145 typically observed in the dusk MLT sector. Hiss 146 waves are observed inside the plasmasphere. Figure 147 from Millan and Thorne (2007).	24
148 1.13 An example train of microbursts observed by FIREBIRD- 149 II unit 4 on February 2nd, 2015. The colored curves 150 show the differential energy channel count rates in 151 six channels from ≈ 200 keV to greater than 1 MeV. 152 The x-axis labels show auxiliary information such as 153 time of observation and the spacecraft position in L, 154 MLT, latitude and longitude coordinates.	27
155 1.14 Relativistic (> 1 MeV) distribution of microburst 156 occurrence rates as a function of L and MLT. The 157 three panels show the microburst occurrence rate 158 dependence on geomagnetic activity, parameterized 159 by the auroral electrojet (AE) index for (a) $AE <$ 160 100 nT, (b) $100 < AE < 300$ nT and (c) $AE > 300$ 161 nT. Figure from Douma et al. (2017)....	28

LIST OF FIGURES – CONTINUED

Figure	Page
162 2.1 Electron and wave conditions from the MagEIS-A 163 and EMFISIS WFR sensors for the microburst time 164 interval. Panels (a), (b), and (c) are from RBSP-A 165 with its position information annotated in panel (a). 166 Panels (d), (e), and (f) are from RBSP-B with its 167 position information annotated in panel (d). Panel 168 (a) is the MagEIS-A high rate timeseries. Panels (b) 169 and (e) show the evolution of the MagEIS-A J as a 170 function of α_L from the ~ 40 to ~ 60 keV channel. 171 Every 10th point is shown in panel (b). The solid 172 black line in panels (a) and (b) mark the end of 173 the time period used for the PSD fit extrapolation 174 analysis explained in section 3. The dashed black 175 lines in panels (a) and (b) show the time interval 176 used for the observed microburst PSD. Panels (c) 177 and (f) show the EMFISIS WFR spectra, with the 178 available burst data superposed. The red, green, and 179 cyan traces are equatorial f_{ce0} , $f_{ce0}/2$, and $f_{ce0}/10$, 180 respectively.	39
181 2.2 Panel (a) shows the MagEIS-A high rate timeseries. 182 Panel (b) shows the RBSPICE EBR count rate 183 timeseries for $\gtrsim 19$ keV electrons. The microbursts 184 were observed between 11:17:10 - 11:17:12 UT and 185 are indicated with the vertical black arrows in panels 186 (a) and (b) for MagEIS-A times. Panel (c) shows the 187 RBSPICE EBR (family of relatively sparse sampled 188 curves) and MagEIS-A J from the 29-41 keV energy 189 channel (single curve) as a function of α_L . The 190 vertical dashed lines show the time interval for the 191 PSD analysis.....	40

LIST OF FIGURES – CONTINUED

Figure	Page
192 2.3 The colored annulus represents $f(p_\perp, p_{\parallel})$ in normalized momentum space, parallel and perpendicular to the background magnetic field. The microburst $f(p_\perp, p_{\parallel})$ is highlighted with the white circle. The columns show different powers of the sine extrapolation, and rows show the different magnetic latitudes of the scattering. The white dotted traces represent the boundary between the data and extrapolation. The green, red, and white solid traces are the resonance curves for $\omega = 0.2\Omega_{ce}$, $0.4\Omega_{ce}$, $0.6\Omega_{ce}$, respectively. The cyan dashed traces are the diffusion curves for a $\omega = 0.4\Omega_{ce}$ wave (waves of other frequency have similar diffusion curves). The magnetic latitude of the scattering, the ratio of the plasma to the cyclotron frequency, and the power of the sine extrapolation is annotated in each panel. For the resonance and diffusion curves, the density model assumed a $n_L = 1 e^-/cm^3$ and $\psi = -1$	44
210 3.1 HiRes data of the microburst observed at February 2nd, 2015 at 06:12:53 UT, smoothed with a 150 ms rolling average. The subsequent bounces showed some energy dispersion. As discussed in Appendix B, a time correction of -2.28 s was applied to FU3. While the flux from five energy channels is shown, only channels with reasonable counting statistics were used for the spatial scale analysis. Vertical colored bars show the \sqrt{N} error every 10th data point and vertical black bars are lined up with the peaks in the 220-283 keV energy channel to help identify dispersion.	57

LIST OF FIGURES – CONTINUED

Figure	Page
222 3.2 Observed and theoretical t_b for electrons of energies 223 from 200 to 770 keV. The solid black line is t_b 224 in a dipole magnetic field, derived in Schulz and 225 Lanzerotti (1974). The red dotted and cyan dashed 226 lines are the t_b derived using the T89, and T04 227 magnetic field models with IRBEM-Lib. Lastly, 228 the blue dot-dash curve is the t_b derived using the 229 Olson & Pfitzer Quiet model. The green and purple 230 rectangles represent the observed t_b for FU3 and 231 FU4 using a Gaussian fit, respectively. The blue 232 rectangles represent the observed t_b calculated with 233 the minima between the bounces. The width of the 234 boxes represent the width of those energy channels, 235 and the height represents the uncertainty from the fit.....	60
236 3.3 The topology of the FIREBIRD-II orbit and the 237 multiple bounces of the microburst projected onto 238 latitude and longitude with axis scaled to equal 239 distance. Attributes relating to FU3 shown in red 240 dashed lines, and FU4 with blue solid lines. The 241 spacecraft path is shown with the diagonal lines, 242 starting at the upper right corner. The labels P1- 243 4 for FU4 and P1-5 for FU3 indicate where the 244 spacecraft were when the N^{th} peak was seen in 245 the lowest energy channel in the HiRes data. The 246 stars with the accompanying energy labels represent 247 the locations of the electrons with that energy that 248 started at time of P1, and were seen at the last peak 249 on each spacecraft. The rectangles represent the 250 lower bound of the microburst scale size, assuming 251 that the majority of the electrons were in the upper 252 boundary of energy channel 4.....	62

LIST OF FIGURES – CONTINUED

Figure	Page
253 A.1 Panel (A) shows the magnetic power spectral density 254 as a function of frequency and time from the EMFI- 255 SIS WFR instrument on board RBSP-A. The “hiss- 256 like” wave used for the resonant diffusion analysis 257 was observed starting at 11:17:03 UT. In the same 258 format as panel (A), panel (B) shows the polar angle 259 of the wave vector for this time period. The wave 260 of interest had a normal wave vector, $\theta_k < 30^\circ$. 261 Since the results in panel (B) are valid only for high 262 planarity, panel (C) shows planarity in the same 263 format as panels (A) and (B). The wave of interest 264 was found to have a planarity of > 0.8 . Lastly, panel 265 (D) shows the available burst mode data.	78
266 A.2 Ratio of the RBSPICE EBR at microburst times 267 indicated with the black vertical arrows in Fig. 2, 268 to the EBR at the same pitch angles one spin prior 269 (quiet time). The microburst flux was enhanced by 270 10-80% across $100^\circ < \alpha_L < 160^\circ$ PA, and appear to 271 be peaked closer to $\alpha_L = 90^\circ$	79
272 B.1 Cross-correlation time lag analysis applied to a train 273 of microbursts. Panel (a) and (b) show the count 274 rate from the lowest energy channel. Panel (c) shows 275 the cross-correlation coefficient as a function of time 276 lag. Panel (d) shows the shifted timeseries. Clock 277 difference was 2.23 s.	82
278 B.2 Same analysis as Fig. B.1 on a different time period. 279 Clock difference was 2.21 s.	83
280 B.3 Same analysis as Fig. B.1 on a different time period. 281 Clock difference was 2.25 s.	84
282 B.4 Same analysis as Fig. B.1 on a different time period. 283 Clock difference was 2.27 s.	85

LIST OF FIGURES – CONTINUED

Figure		Page
284	B.5 Same cross-correlation time lag analysis applied to	
285	stationary spatial structures. The cross-correlation	
286	lag between these events is a sum of the clock differ-	
287	ence and time lag due to the spacecraft separation.	
288	The lag derived at this time was 4.95 s.....	86
289	B.6 Same analysis as Fig. B.5 applied to a different	
290	stationary spatial feature. The lag derived at this	
291	time was 5.01 s.	87

NOMENCLATURE

L	L-Shell
MLT	magnetic local time
λ	magnetic latitude
α	pitch angle
α_L	local pitch angle at the spacecraft
α_{eq}	pitch angle maped to the magnetic equator
c	speed of light
R_E	Earth's radius
J	flux
f	phase space density
E	energy
E_0	exponential e-folding energy
p	momentum
\vec{E}	electric field
\vec{B}	magnetic field
B_w	wave amplitude
v	velocity
Ω_e	electron gyrofrequency
ω_{pe}	plasma frequency
k	wave vector
D_{xx}	diffusion coefficient
s	spacecraft separation
t_b	electron bounce period

292

293

INTRODUCTION

294 Above Earth's atmosphere are the a pair of Van Allen radiation belts, a complex
295 and dynamic plasma environment that effects our technology-driven society. These
296 effects include: a higher radiation dose for astronauts and cosmonauts, higher chance
297 of spacecraft failure due to single event upsets that can lead to catastrophic latchups,
298 degradation of silicon (changing the silicon doping) from an extended radiation dose
299 that can degrade a transistor to the point where it no longer function as a switch,
300 and the degradation of the ozone layer due to the chemical production of NO_X and
301 HO_X molecules. With these effects in mind, it is no surprise that the radiation belts
302 have been extensively studied since their discovery in the 1960s.

303 One natural phenomenon in the radiation belts that has been a topic of interest
304 in the space physics community is wave-particle intersections that, as we will explore
305 throughout this dissertation, can accelerate particles to very high energies (e.g. \approx
306 MeV for electrons) and scatter them into the atmosphere.

307 The goal of this dissertation is to study the wave-particle mechanism that
308 scatters microbursts, a sub-second impulse of electrons into Earth's atmosphere.
309 Before we dive deep into the physics of wave-particle interactions, an introduction to
310 Earth's magnetosphere is warranted. Single charged particle motion in Earth's electric
311 and magnetic fields will be described first. Then the major particle populations in
312 the magnetosphere and the coupling between them will be described. Lastly, a brief
313 overview of wave-particle interactions and their effects will be presented.

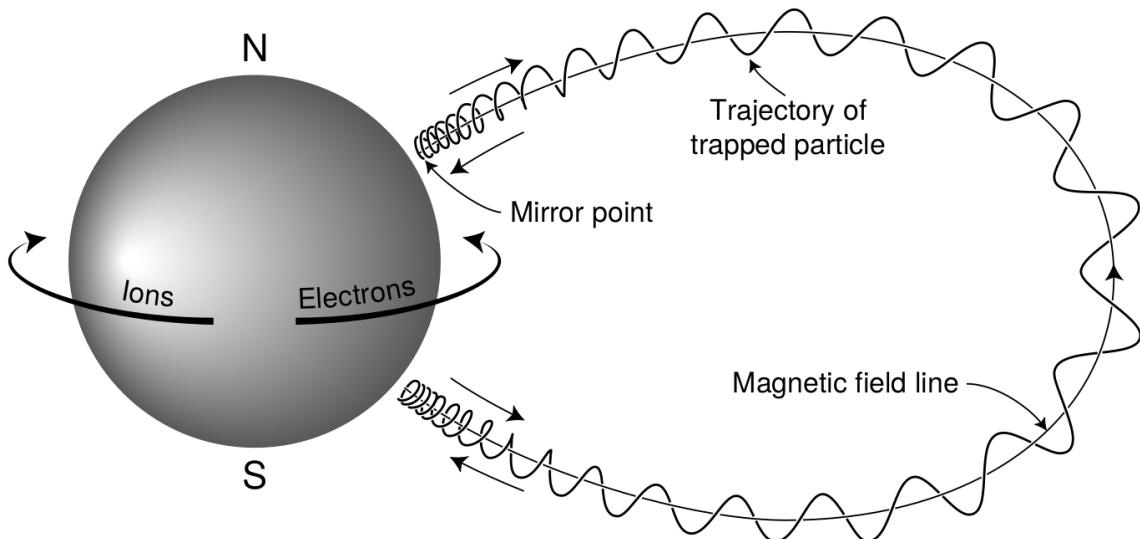


Figure 1.1: The three periodic motions of charged particles in Earth's dipole magnetic field. These motions are: gyration about the magnetic field line, bounce motion between the magnetic poles, and azimuthal drift around the Earth. Figure from (Baumjohann and Treumann, 1997).

³¹⁴

Charged Particle Motion in Electric and Magnetic Fields

A charged particle trapped in the magnetosphere will experience three types of periodic motion in Earth's nearly dipolar magnetic field. The three motions are ultimately due to the Lorentz force that a particle of momentum \vec{p} , charge q , and velocity \vec{v} experiences in an electric field \vec{E} and magnetic field \vec{B} and is given by

$$\frac{d\vec{p}}{dt} = q(\vec{E} + \vec{v} \times \vec{B}). \quad (1.1)$$

- ³¹⁵ In the magnetosphere, the three periodic motions in decreasing frequency are gyration,
- ³¹⁶ bounce, and drift and are schematically shown in Fig. 1.1. Each of these
- ³¹⁷ motions have a corresponding conserved quantity i.e. an adiabatic invariant.

The highest frequency periodic motion is gyration about a magnetic field of

magnitude B . This motion is circular with a Larmor radius of

$$r = \frac{mv_{\perp}}{|q|B} \quad (1.2)$$

where m is the mass and v_{\perp} the particle's velocity perpendicular to \vec{B} . This motion has a corresponding gyrofrequency

$$\Omega = \frac{|q|B}{m} \quad (1.3)$$

in units of radians/second. Inside the radiation belts the electron gyrofrequency, Ω_e is on the order of a kHz. The corresponding adiabatic invariant is found by integrating the particle's canonical momentum around the particle's path of gyration

$$J_i = \oint (\vec{p} + q\vec{A}) \cdot d\vec{l} \quad (1.4)$$

where J_i is the i^{th} adiabatic invariant and \vec{A} is the magnetic vector potential. This integral is carried out by integrating the first term over the circumference of the gyro orbit and integrating the second term using Stokes theorem to calculate the magnetic flux enclosed by the gyro orbit. With suitable integration, $J_1 \sim v_{\perp}^2/B$ and is conserved as the frequency of the driving force, ω satisfies $\omega \ll \Omega_e$.

The second highest frequency periodic motion is bouncing due to a parallel gradient in \vec{B} . This periodic motion naturally arises in the magnetosphere because Earth's magnetic field is stronger near the poles, and artificially in the laboratory in magnetic bottle machines. To understand this motion we first we need to define the concept of pitch angle α as the angle between \vec{B} and \vec{v} which is schematically shown in Fig. 1.2a. The pitch angle relates v with v_{\perp} , and $v_{||}$ (the component of the particles velocity parallel to \vec{B}). As shown in 1.2b and c, a larger α will tighten the

³³⁰ particle's helical trajectory and vice versa.

Assuming the particle's kinetic energy is concerned, the conservation of J_1 implies that given a particle's $v_{\perp}(0)$ and $B(0)$ at the magnetic equator (where Earth's magnetic field is usually at a minimum), we can calculate its $v_{\perp}(s)$ along the particle's path s by calculating $B(s)$ from magnetic field models. The particle's perpendicular velocity is then related via

$$\frac{v_{\perp}^2(0)}{B(0)} = \frac{v_{\perp}^2(s)}{B(s)} \quad (1.5)$$

³³¹ which can be rewritten as

$$\frac{v^2 \sin^2 \alpha(0)}{B(0)} = \frac{v^2 - v_{\parallel}^2(s)}{B(s)} \quad (1.6)$$

³³² and re-arranged to solve for $v_{\parallel}(s)$

$$v_{\parallel}(s) = v \sqrt{1 - \frac{B(s)}{B(0)} \sin^2 \alpha(0)} \quad (1.7)$$

³³³ which will tend towards 0 when the second term in the radical approaches 1.

³³⁴ The location where $v_{\parallel}(s) = 0$ is called the mirror point and is where a particle
³³⁵ stops and reverses direction. Since Earth's magnetic field is stronger towards the
³³⁶ poles, the mirroring particle will execute periodic bounce motion between its two
³³⁷ mirror points in the northern and southern hemispheres. The corresponding adiabatic
³³⁸ invariant, J_2 is

$$J_2 = \oint p_{\parallel} ds \quad (1.8)$$

where ds describes the particle path between the mirror points in the northern and southern hemispheres (see Fig. 1.1). J_2 is found by substituting Eq. 1.7 into Eq. 1.8 and defining the magnetic field strength at the mirror points as B_m where $\alpha(m) = 90^\circ$.

The J_2 integral can be written as

$$J_2 = 2p \int_{m_n}^{m_s} \sqrt{1 - \frac{B(s)}{B(m)}} ds \quad (1.9)$$

339 where m_n and m_s are the northern and southern mirror points, respectively. The
 340 bounce period can be estimated (e.g. Baumjohann and Treumann, 1997) to be

$$t_b \approx \frac{LR_e}{\sqrt{W/m}} (3.7 - 1.6 \sin \alpha(0)) \quad (1.10)$$

341 where L is the L -shell which describes the distance from the Earth's center to the
 342 location where a particular magnetic field line crosses the magnetic equator, in units
 343 of Earth radii, R_e . W is the particle's kinetic energy. As with gyration, a particle
 344 bounces as long as $\omega \ll \Omega_b$, where Ω_b is the bounce frequency.

345 At this stage it is instructional to introduce the notion of the loss cone pitch
 346 angle, α_L . A particle with $\alpha \leq \alpha_L$ will mirror at or below ≈ 100 km altitude in the
 347 atmosphere. A particle at those altitudes will encounter Earth's atmosphere and has
 348 a significant probability of Coulomb scattering with atmospheric particles and be lost
 349 to the atmosphere.

350 The slowest periodic motion experienced by charged particles in Earth's mag-
 351 netic field is azimuthal drift around the Earth. This drift results from a combination of
 352 a radial gradient in \vec{B} and the curvature of the magnetic field. The radial gradient drift
 353 arises because Earth's magnetic field is stronger near the Earth where the particle's
 354 gyroradius radius of curvature is smaller as it gyrates towards stronger magnetic field,
 355 and larger when it gyrates outward. The overall effect is the particle gyro orbit does
 356 not close on itself and negatively charged particles drift East and positively charged
 357 particles drift West. The radial gradient drift is enhanced by the centrifugal force that
 358 a particle experiences as it bounces along the curved field lines. The drift adiabatic

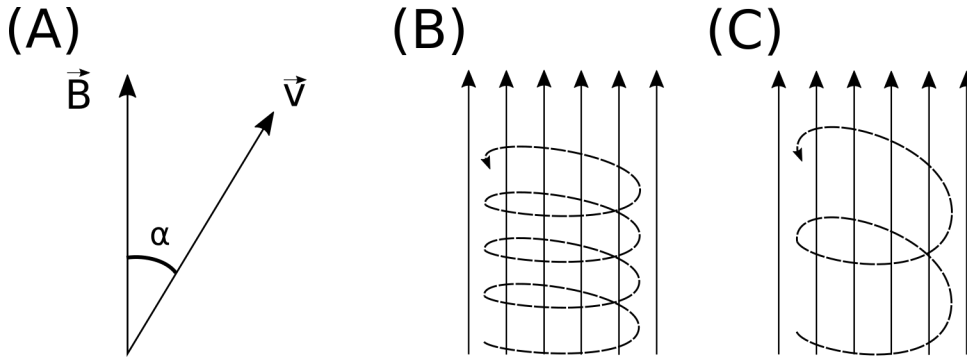


Figure 1.2: Charged particle motion in a uniform magnetic field \vec{B} . Panel (A) shows the geometry defining the pitch angle, α . Panel (B) and (C) show two helical electron trajectories with dashed lines assuming a large and small α (corresponding to a small and large parallel velocity $v_{||}$), respectively.

359 invariant, J_3 is found by integrating Eq. 1.4 over the complete particle orbit around
 360 the Earth. The shape of this drift orbit is otherwise known as a drift shell. For J_3 ,
 361 the first term is negligible and the second term is the magnetic flux enclosed by the
 362 drift shell, Φ_m i.e. $J_3 \sim \Phi_m$.

363 Figure 1.3 from Schulz and Lanzerotti (1974) shows contours of the gyration,
 364 bounce, and drift frequencies for electrons and protons in Earth's dipole magnetic
 365 field.

Up until now we have considered the three periodic motions due Earth's magnetic field and the absence of electric fields. If \vec{E} is present, a particle's center of gyration i.e., averaged position of the particle over a gyration, will drift with a velocity perpendicular to both \vec{E} and \vec{B} . The drift velocity can be solved directly from Eq. 1.1 and is

$$\vec{v}_E = \frac{\vec{E} \times \vec{B}}{B^2}. \quad (1.11)$$

366 Lastly, for more detailed derivations of these motions, see the following texts:
 367 Baumjohann and Treumann (1997); Schulz and Lanzerotti (1974); Tsurutani and
 368 Lakhina (1997).

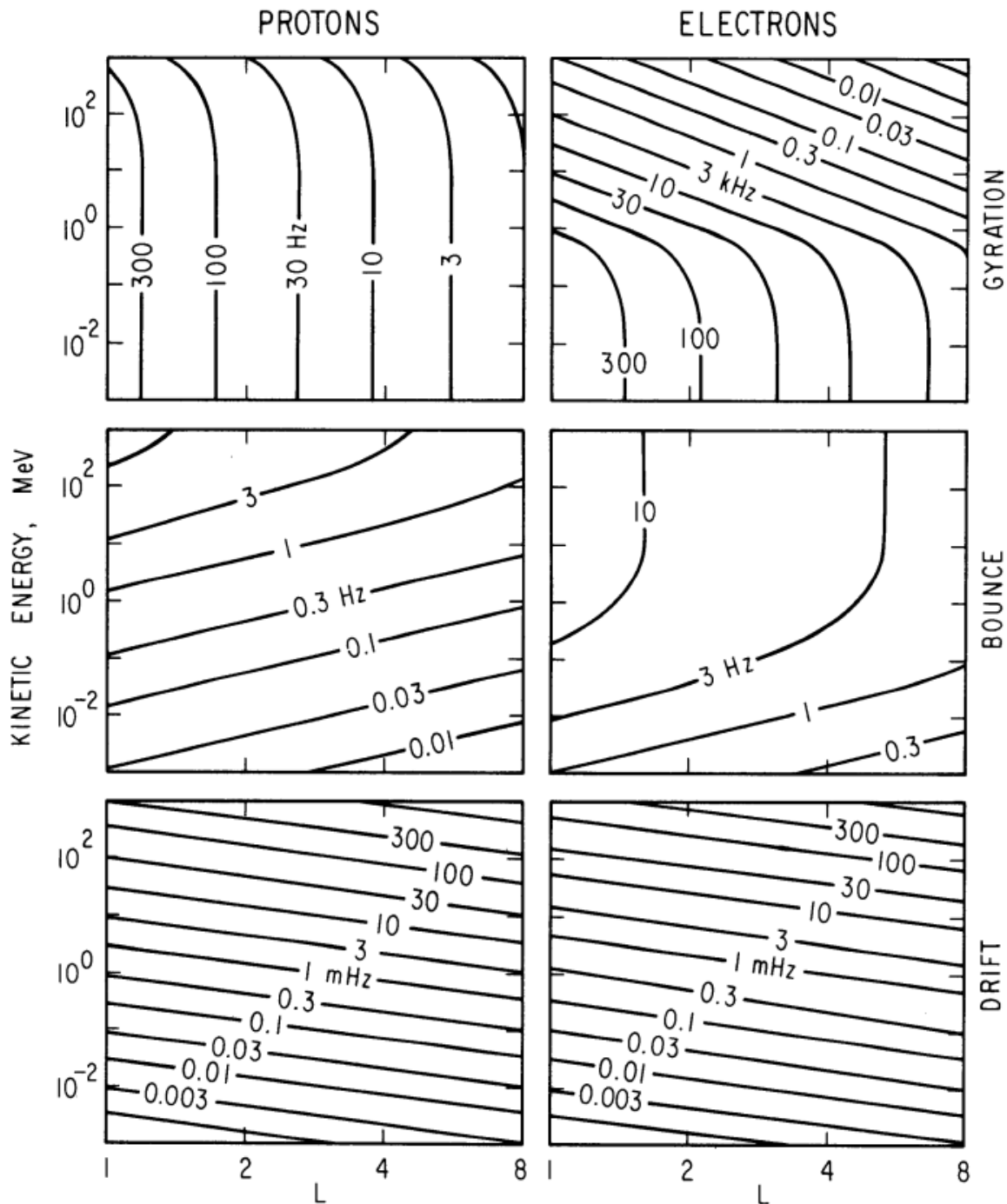


Figure 1.3: Contours of constant gyration, bounce, and drift frequencies for electrons and protons in a dipole field. Figure from Schulz and Lanzerotti (1974).

369 Particle Populations and Their Interractions in the Magnetosphere

370 The single-particle motion in Earth's magnetic field described in the previous
371 section is a prerequisite to understanding how magnetospheric particles organize into
372 macroscopic populations. The structure of the outer magnetosphere is shown in Fig.
373 1.4 and inner magnetosphere in Fig. 1.5. In this section we will introduce the various
374 particle populations in the magnetosphere and how they couple.

375 The sun and its solar wind are ultimately the source of energy input into the
376 magnetosphere. The solar wind at Earth's orbit is a plasma traveling at supersonic
377 speeds with an embedded interplanetary magnetic field (IMF). When the solar wind
378 encounters Earth's magnetic field the plasma can not easily penetrate into the
379 magnetosphere, rather it drapes around the magnetosphere forming a cavity in the
380 solar wind that is roughly shaped as shown in Fig. 1.4. Because the solar wind is
381 supersonic at 1 AU, a bow shock exists upstream of the magnetosphere. The solar
382 wind plasma, after it is shocked by the bow shock, flows around the magnetosphere
383 inside the magnetosheath. The surface where the solar wind ram pressure and Earth's
384 magnetic pressure balance is termed the magnetopause, which can be thought of as
385 a boundary between the solar wind's and Earth's plasma environments. This is
386 a slightly naive description of the magnetopause, but is nonetheless an instructive
387 conceptual picture. The shocked plasma then flows past the Earth where it shapes
388 the magnetotail. In the magnetotail the solar wind magnetic pressure balances Earth's
389 magnetic field pressure in the lobes. The magnetotail extends on the order of 100
390 R_E downstream of Earth [Add citation](#), and the tailward stretching of magnetic field
391 lines creates the plasma sheet which exists in the region of low magnetic field strength
392 near the magnetic equator [Add citation](#). The plasma sheet flows from dusk to dawn
393 (out of the page in Figs. 1.4 and 1.5) and this current is connected to a zoo of other

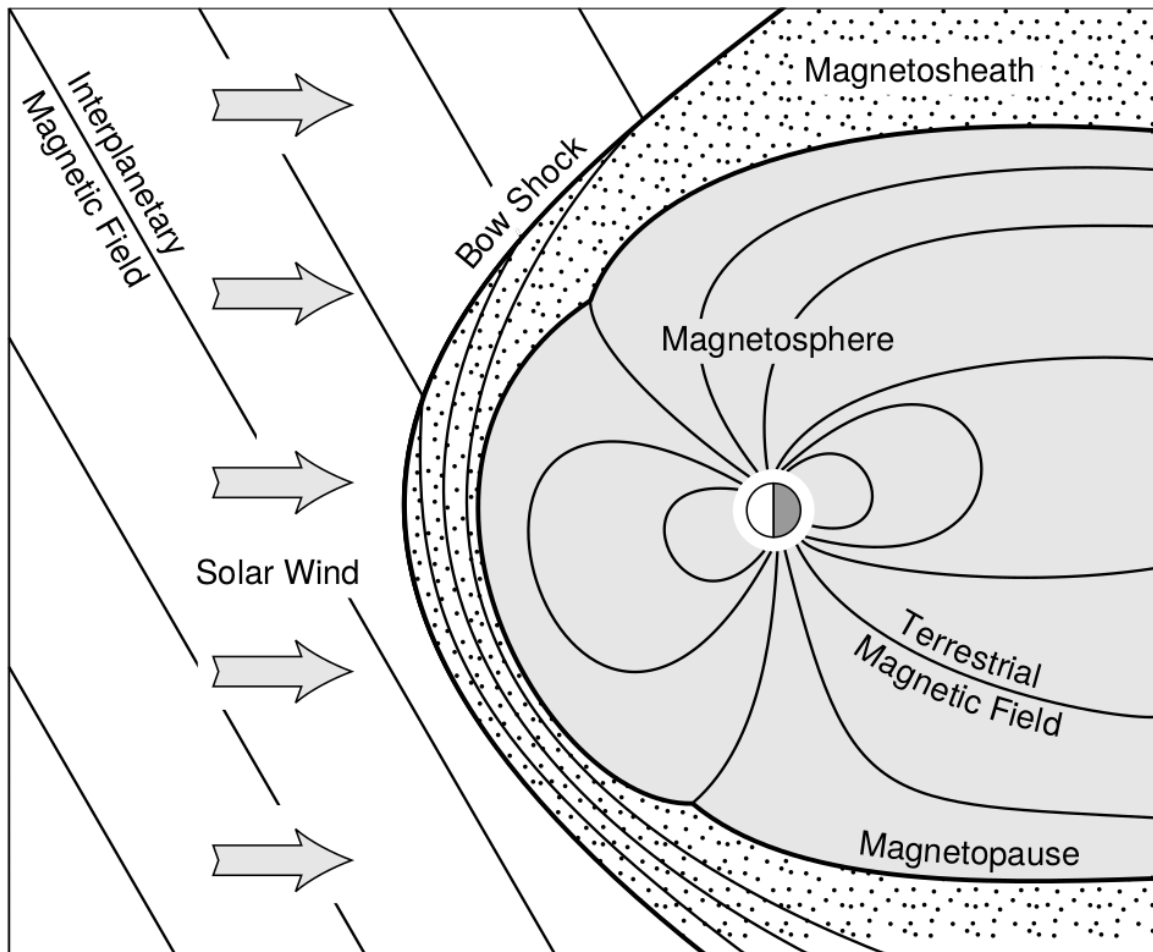


Figure 1.4: Macroscopic structures in the outer magnetosphere. The solar wind with its frozen-in interplanetary magnetic field is shown on the left and is traveling supersonically towards the right. The solar wind envelops Earth's magnetic field to create the magnetosphere cavity. Since the solar wind is traveling supersonically, it creates a bow shock up stream. Downstream of the bow shock the shocked solar wind plasma inside the magnetosheath flows around the magnetopause, a boundary between the solar wind and magnetosphere. Figure from Baumjohann and Treumann (1997).

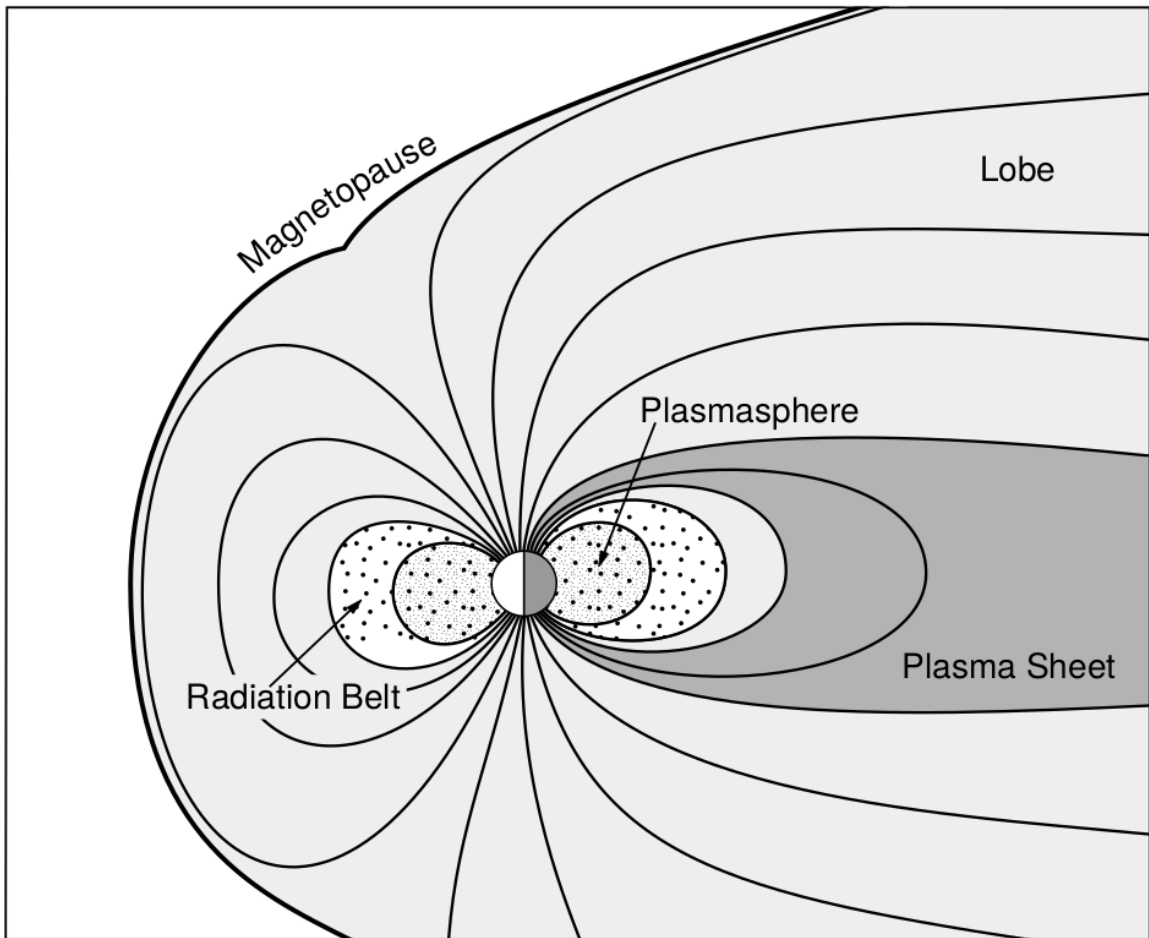


Figure 1.5: Macroscopic structures in the inner magnetosphere most relevant to this dissertation. The plasmasphere, and the radiation belts are shown and ring current is co-located there as well. Sun is to the left. Figure from Baumjohann and Treumann (1997).

394 currents in the magnetosphere which is beyond the scope of this dissertation.

395 The idea of the magnetopause as a barrier between the solar wind and
 396 the magnetosphere is not entirely accurate due to the presence of reconnection.
 397 Reconnection was first conceived by Dungey (1961) who described the convection of
 398 Earth's magnetic field between the bow and tail regions of the magnetosphere. This
 399 process is known as the Dungey cycle and is most effective when the IMF is pointing
 400 southward as is shown in Fig. 1.6 part 1. As the IMF contacts Earth's magnetic
 401 field it reconnects with it so that Earth's magnetic field is directly connected to the
 402 IMF. Then as the solar wind flows tailward the IMF drags Earth's magnetic field
 403 towards the magnetotail as shown in Fig. 1.6 parts 2-6. As more and more magnetic
 404 field lines are draped in the magnetotail, magnetic pressure increases in the lobes
 405 which squeezes the plasma sheet until Earth's magnetic field reconnects as is shown
 406 in Fig. 1.6 part 7. Lastly, Fig. 1.6 part 8 shows the newly merged magnetic field
 407 line and the plasma frozen on it moves Earthward under the magnetic tension force
 408 to become more dipolar. This is called a dipolarization of the magnetic field, and the
 409 plasma frozen on these field lines can be observed as injections (e.g. Turner et al.,
 410 2015). Injection of plasma into the inner magnetosphere is one of the drivers of inner
 411 magnetosphere dynamics. Should I talk about the K-H instability and how there
 412 could be micro reconnection? i.e. cite a paper or two that support or refute that
 413 idea.

414 Inner Magnetosphere Populations

415 Before we describe the inner magnetosphere particle populations, we first need to
 416 describe the coordinate system used to organize the inner magnetosphere populations.
 417 The first coordinate was defined in section 1 and is the L shell. L shell can be thought
 418 of as an analogue to a radius but in a dipole geometry. The azimuthal coordinate

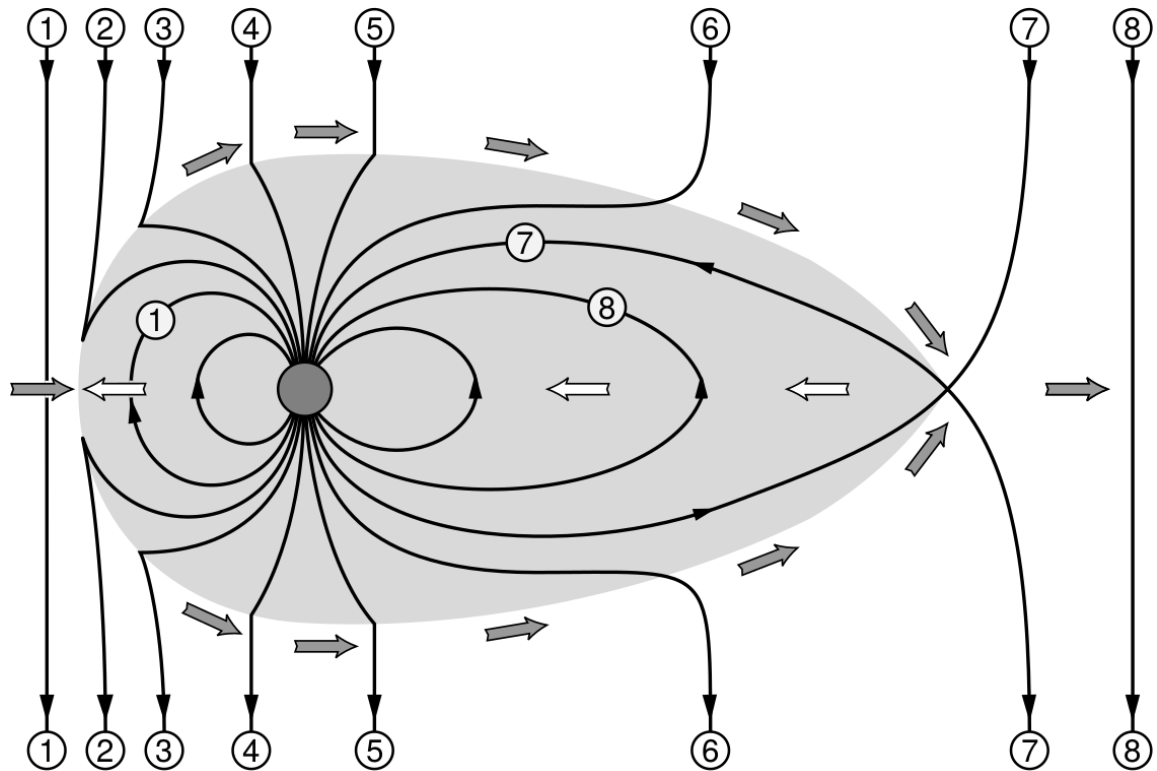


Figure 1.6: The series of steps involved in magnetic reconnection with a southward IMF. Figure from Baumjohann and Treumann (1997).

419 is the magnetic local time (MLT). For an observer above Earth's north pole looking
 420 down, MLT is defined to be 0 (midnight) in the anti-sunward direction, and increases
 421 in the counter-clockwise direction with 6 at dawn, 12 at noon (sunward direction),
 422 and 18 in dusk. The last coordinate used in this dissertation is the magnetic latitude,
 423 λ which is analogous to the latitude coordinate and is defined to be 0 at the magnetic
 424 equator.

425 The low energy particle dynamics in the inner magnetosphere are organized by
 426 two electric fields: the co-rotation and the dawn-dusk electric fields. The co-rotation
 427 electric field arises from the rotation of Earth's magnetic field. Since particles are
 428 frozen on magnetic field lines and the plasma conductivity is effectively infinite, to
 429 a non-rotating observer, Earth's rotation appears as a radial electric field that drops
 430 off as $\sim L^2$. This electric field makes particles orbit around the Earth due to the
 431 $\vec{E} \times \vec{B}$ drift. The other electric field, pointing from dawn to dusk is called the
 432 convection electric field and is formed by the Earthward transport of particles from
 433 the magnetotail that appears as an electric field to a stationary observer (with respect
 434 to Earth). The superposition of the co-rotation and convection electric fields
 435 results in a potential field shown in Fig. 1.7. The shaded area in Fig. 1.7 shows
 436 the orbits on which low energy electrons are trapped, and outside are the untrapped
 437 particles. The dynamic topology of the shaded region in Fig. 1.7 is controlled by only
 438 the convection electric field which is dependent on the solar wind speed and the IMF.
 439 The lowest energy particles, that are most effected by these electric fields, make up
 440 the plasmasphere.

441 Plasmasphere The plasmasphere is a dense ($n_e \sim 10^3/\text{cm}^3$), cool plasma
 442 ($\sim \text{eV}$) that extends to $L \sim 4$ (extent is highly dependent on the solar wind and
 443 magnetospheric conditions) and is sourced from the ionosphere. The two main

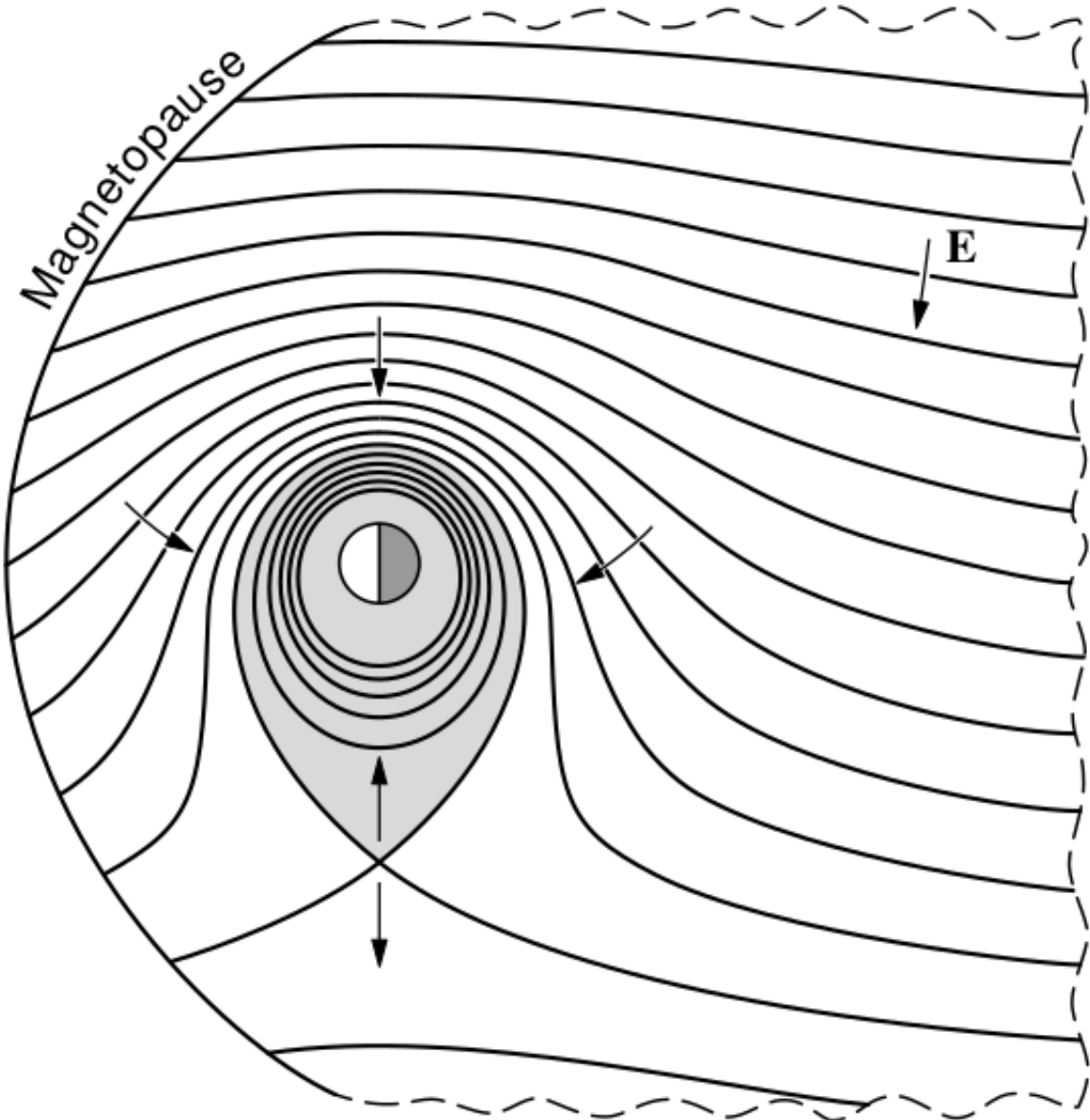


Figure 1.7: Equipotential lines and electric field arrows due to the superposition of the co-rotation and convection electric fields. Electrons in the shaded region execute closed orbits. Outside of the shaded regions the electrons are not trapped and will escape. The region separating the two regimes is called the Alfvén layer. Figure from Baumjohann and Treumann (1997).

444 mechanisms that source the cold plasma from the ionosphere are ultraviolet ionization
 445 by sunlight and particle precipitation. The ultraviolet ionization by sunlight is
 446 strongly dependent on the time of day (day vs night), latitude (more ionization near
 447 the equator). The ionization due to particle precipitation, on the other hand, is highly
 448 dependent on magnetospheric conditions, and mostly occurs at high latitudes.

449 The outer boundary of the plasmasphere is the plasmapause which is typically
 450 identified as a steep radial gradient in plasma density from $\sim 10^3/\text{cm}^3$ to $\sim 1/\text{cm}^3$. As
 451 we will see throughout this dissertation, the location of the plasmapause is important
 452 to model (e.g. O'Brien and Moldwin, 2003) and understand since the plasma density
 453 strongly controls the efficiency of particle scattering (Horne et al., 2005).

454 Ring Current The next higher energy population is the ring current. This
 455 population consists of protons and electrons between tens and a few hundred keV
 456 that drift around the Earth. The orbits of higher energy particles are not as effected
 457 by the convection and co-rotation electric field, rather they drift around the Earth
 458 due to gradient and curvature drifts. Since the direction of the drift is dependent on
 459 charge, protons drift west around the Earth and electrons drift East. This has the
 460 effect of creating a current around the Earth.

461 The ring current generates a magnetic field which decreases the magnetic field
 462 strength on Earth's surface and increases it outside of the ring current. The decrease
 463 of Earth's magnetic field strength is readily observed by a system of ground-based
 464 magnetometers and is merged into a Disturbance Storm Time (DST) index. An
 465 example of a DST index time series from a coronal mass ejection (CME) driven 2015
 466 St. Patrick's Day storm is shown in Fig. 1.8. The ring current is sometimes first
 467 depleted and DST increases slightly (initial phase or sudden storm commencement).
 468 Then the ring current is rapidly built up during which DST rapidly decreases (main

469 phase). Lastly the ring current gradually decays toward its equilibrium state over a
 470 period of a few days and DST increases towards 0 (recovery phase). The DST index
 471 along with other indicies are readily used by the space physics community to quantify
 472 the global state of the magnetosphere.

473 Radiation Belts The highest energy particle populations are in the Van Allen
 474 radiation belts. These belts were discovered by Van Allen (1959) and Vernov and
 475 Chudakov (1960) during the Cold War and are a pair of toroidally shaped populations
 476 of trapped electrons and protons usually within to $L < 8$ and are shown in Fig. 1.9.
 477 Their quiescent toroidal shape is similar to the shape of the plasmasphere and ring
 478 current and is a result of Earth's dipole magnetic field and the conservation of the
 479 three adiabatic invariants discussed in section 1.

480 The inner radiation belt is extremely stable on time periods of years, extends
 481 to $L \approx 2$, and mainly consists of protons with energies between MeV and GeV and
 482 electrons with energies up to ≈ 1 MeV (Claudepierre et al., 2019). The source of
 483 inner radiation belt protons is believed to be due to cosmic-ray albedo neutron decay
 484 (e.g. Li et al., 2017) and inward radial diffusion for electrons (e.g. O'Brien et al.,
 485 2016). The gap between the inner and outer radiation belt is called the slot, which is
 486 believed to be due to hiss waves inside the plasmasphere (described below) scattering
 487 particles into the atmosphere (e.g. Breneman et al., 2015; Lyons and Thorne, 1973).

488 The outer radiation belt, on the other hand is much more dynamic and consists
 489 of mainly electrons of energies up to a few MeV. The outer belt's spatial extent is
 490 highly variable e.g. see Fig. 1.10, and is typically observed at $4 < L < 8$. Since
 491 the outer radiation belt contains a dynamic population of energetic particles that
 492 pose a threat to human and technological presence in Earth's atmosphere and space,
 493 decades of research has been undertaken to understand and predict the outer radiation

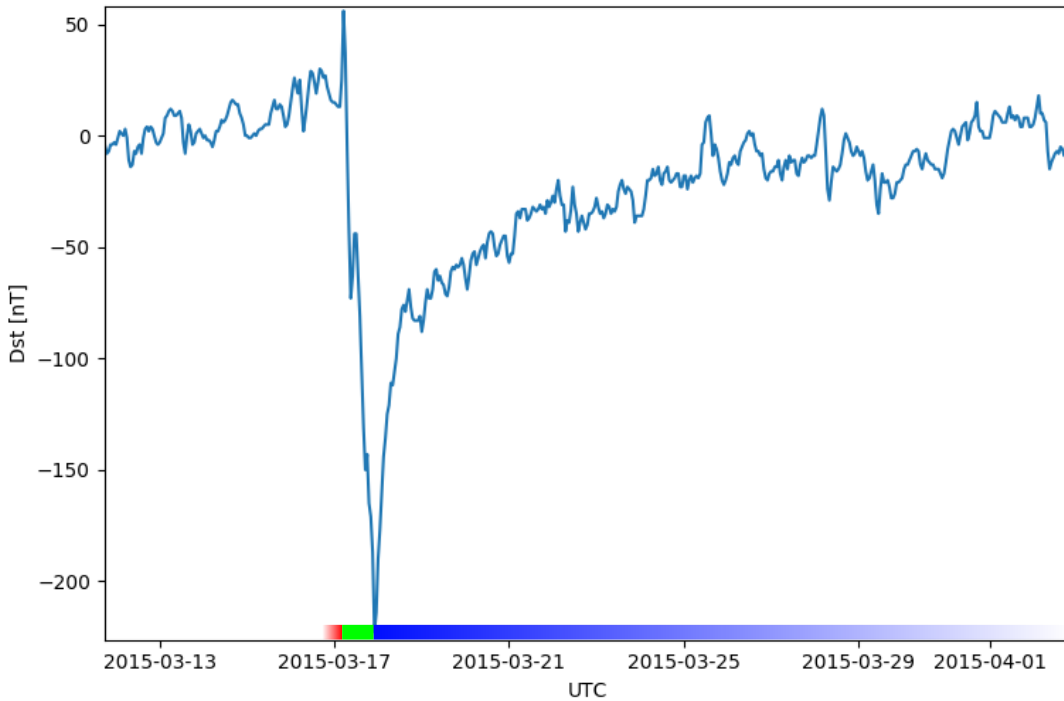


Figure 1.8: The DST index during the St. Patrick's Day 2015 storm. This storm was caused by a coronal mass ejection on March 15th, 2015. The storm phases are: initial phase, main phase, and recovery phase. The initial phase occurred when the Dst peaked at +50 nT on March 17th during which the ring current was eroded by the coronal mass ejection during the interval shown by the red bar. Then the rapid decrease to ≈ -200 nT was during the main phase where many injections from the magnetotail pumped up the ring current which reduced Earth's magnetic field strength at the ground and is shown with the green bar. Lastly, the recovery phase lasted from March 18th to approximately March 29th during which the ring current particles were lost and the ring current returned to its equilibrium state. The recovery phase is shown with the blue bar.

The Earth's Electron Radiation Belts

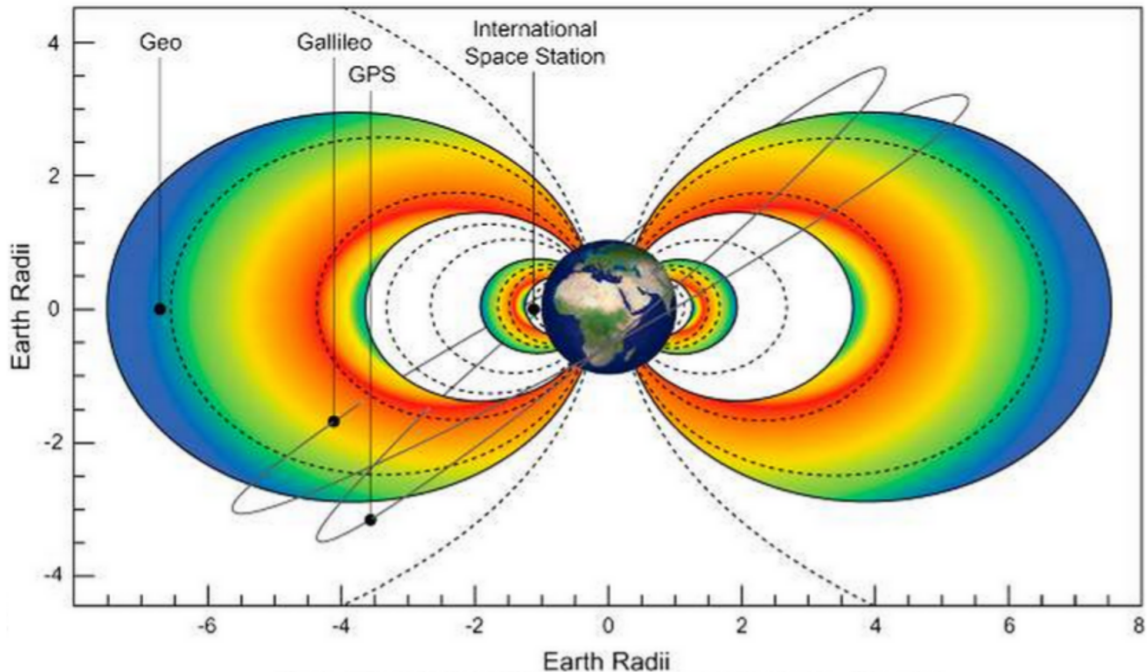


Figure 1.9: The two radiation belts with the locations of various satellites.
Figure from (Horne et al., 2013).

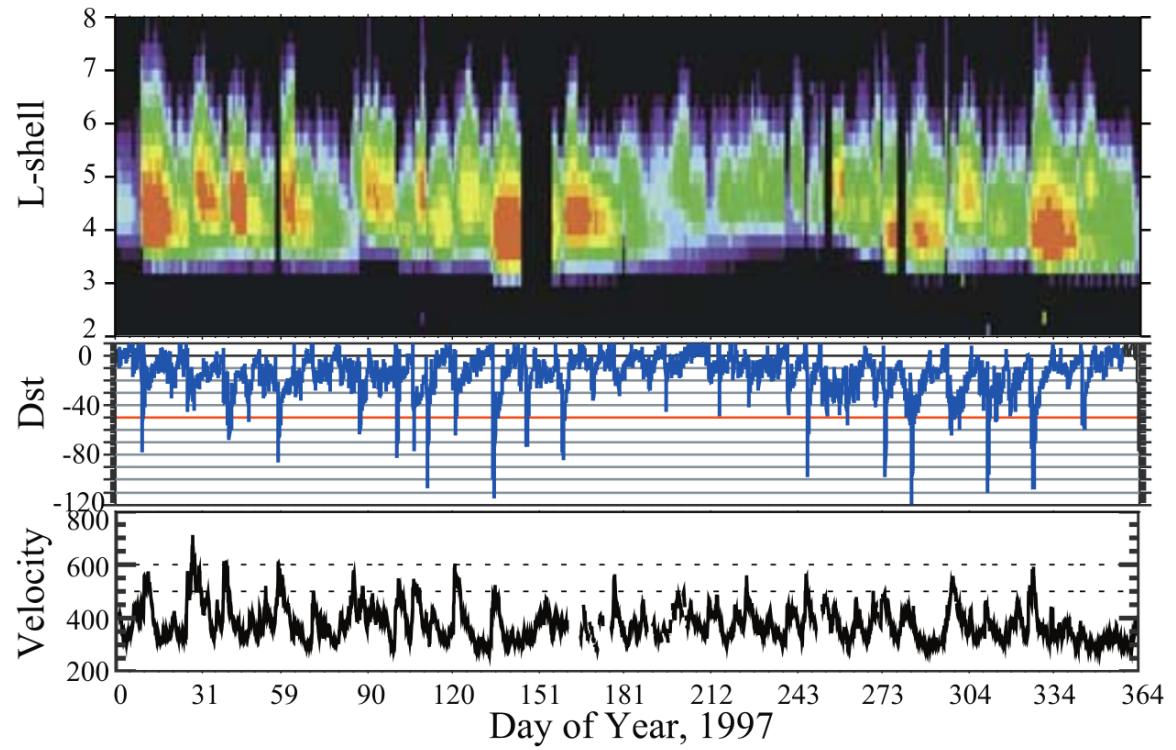


Figure 1.10: The dynamics of the outer radiation belt in 1997 from the POLAR satellite. Top panel shows the 1.2-2.4 MeV electron flux as a function of L and 1997 day of year. The middle panel shows the DST index, and bottom panel shows the solar wind velocity. Figure from (Reeves et al., 2003).

494 belt particles, waves, and wave-particle interactions. The dynamics of the outer
 495 radiation belt can be understood by considering various competing acceleration and
 496 loss mechanisms which will be described in the following sections.

497 Radiation Belt Particle Sources and Sinks

498 Adiabatic Heating

499 One of the particle heating and transport mechanisms arises from the Earthward
 500 convection of particles. The conservation of J_1 implies that the initial and final v_{\perp}
 501 depends on the change in the magnetic field amplitude

$$\frac{v_{\perp i}^2}{B_i} = \frac{v_{\perp f}^2}{B_f}. \quad (1.12)$$

502 As a particle convects Earthward, $B_f > B_i$ thus v_{\perp} must increase. The dipole
 503 magnetic field amplitude can be written as

$$B(L, \theta) = \frac{31.2 \mu\text{T}}{L^3} \sqrt{1 + 3 \cos^2 \theta} \quad (1.13)$$

504 which implies that

$$\frac{v_{\perp f}^2}{v_{\perp i}^2} = \left(\frac{L_i}{L_f} \right)^3. \quad (1.14)$$

505 .

506 In addition, as the particle convects Earthward the distance between the
 507 particle's mirror points decrease. If J_2 is conserved, the shrinking bounce path implies
 508 that $v_{||}$ must increase by

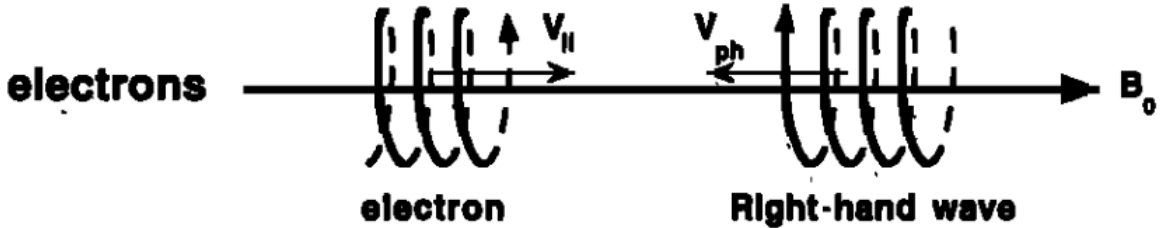
$$\frac{v_{|| f}^2}{v_{|| i}^2} = \left(\frac{L_i}{L_f} \right)^k \quad (1.15)$$

509 where k ranges from 2 for equatorial pitch angles, $\alpha_{eq} = 0^\circ$, to 2.5 for $\alpha_{eq} = 90^\circ$
 510 (Baumjohann and Treumann, 1997). Since the rate of adiabatic heating is greater in
 511 the perpendicular direction than heating in the parallel direction, an initially isotropic
 512 particle distribution will become anisotropic during its convection. These isotropic
 513 particles can then become unstable to wave growth and generate waves in order to
 514 reach equilibrium.

515 Wave Resonance Heating

516 Another mechanism that heats particles is due to particles resonating with
 517 plasma waves. A few of the electromagnetic wave modes responsible for particle
 518 acceleration (and deceleration) relevant to radiation belt dynamics are hiss, whistler
 519 mode chorus (chorus), and electromagnetic ion cyclotron (EMIC) waves. These waves
 520 are created by the loss cone instability that driven by an anisotropy of electrons
 521 for chorus waves, and protons for EMIC waves. The level of anisotropy can be
 522 quantified by the ratio of the perpendicular to parallel particle temperatures ($T_\perp/T_{||}$).
 523 A particle distribution is unstable when $T_\perp/T_{||} > 1$ which facilitates wave growth.
 524 Since electrons gyrate in a right-handed sense, the chorus waves also tend to be right
 525 hand circularly polarized (Tsurutani and Lakhina, 1997). The same argument applies
 526 to protons and left hand circularly polarized EMIC waves as well.

527 These circularly polarized waves can resonate with electrons and/or protons
 528 when their combined motion results in a static \vec{E} . One example of a resonance
 529 between a right hand circularly polarized wave and an electron is shown in Fig. 1.21
 530 and is termed the cyclotron resonance. An electron's $v_{||}$ and the wave's parallel wave
 531 vector, $k_{||}$ are in opposite directions such that the wave frequency ω is Doppler shifted
 532 to an integer multiple of the Ω_e at which point the electron feels a static electric
 533 field and is accelerated or decelerated. This acceleration happens when a resonance



$$\omega + \mathbf{k}_{\parallel} \mathbf{V}_{\parallel} = \Omega^-$$

Figure 1.11: The trajectories of an electron and a right-hand circularly polarized wave during a cyclotron resonance. The electron's v_{\parallel} and the wave's k_{\parallel} are in opposite directions such that the wave's frequency is Doppler shifted to an integer multiple of the electron cyclotron frequency. Figure from (Tsurutani and Lakhina, 1997).

534 condition is satisfied between a wave and a particle for which we will now derive an
 535 illustrative toy model.

536 Assume a uniform magnetic field $\vec{B} = B_0 \hat{z}$ with a parallel propagating ($k = k \hat{z}$),
 537 right-hand circularly polarized wave. The wave's electric field as a function of position
 538 and time can be written as

$$\vec{E} = E_0 (\cos(\omega t - kz) \hat{x} + \sin(\omega t - kz) \hat{y}) \quad (1.16)$$

which is more clearly expressed by taking the dot product to find \vec{E} in the $\hat{\theta}$ direction

$$E_{\theta} = \vec{E} \times \hat{\theta} = E_0 \cos(\omega t - kz + \theta). \quad (1.17)$$

539 Now assume that the electron is traveling in the $-\hat{z}$ direction with a velocity $\vec{v} = -v_0 \hat{z}$
 540 so its time dependent position along \hat{z} is

$$z(t) = -v_0 t \quad (1.18)$$

541 and gyrophase is

$$\theta(t) = -\Omega t + \theta(0) \quad (1.19)$$

542 where the first negative sign comes from the electron's negative charge. Now we put
543 this all together and express the electric field and the force that the electron will
544 experience

$$m \frac{dv_\theta}{dt} = qE_\theta = qE_0 \sin((\omega + kv_0 - \Omega)t + \theta(0)). \quad (1.20)$$

545 This is a relatively complex expression, but when the time dependent component,

$$\omega + kv_0 - \Omega = 0, \quad (1.21)$$

546 the electron will be in a static electric field which will accelerate or decelerate the
547 electron depending on θ_0 , the phase between the wave and the electron. **Show Bortnik**
548 **2008 plot?** The expression in Eq. 1.21 is commonly referred to as the resonance
549 condition and is more generally written as

$$\omega - k_{||}v_{||} = \frac{n\Omega_e}{\gamma} \quad (1.22)$$

550 where n is the resonance order, and γ is the relativistic correction (e.g. Millan and
551 Thorne, 2007). In the case of the cyclotron resonance, $\omega \approx \Omega_e$ thus J_1 is violated.
552 Since J_1 is violated, J_2 and J_3 are also violated since the conditions required to
553 violate J_2 and J_3 are less stringent than J_1 . It is important to remember that along
554 the particle's orbit it will encounter and experience the effects of many waves along
555 its orbit. The typical MLT extent of a handful of waves that are capable of resonating
556 with radiation belt electrons are shown in Fig. 1.12.

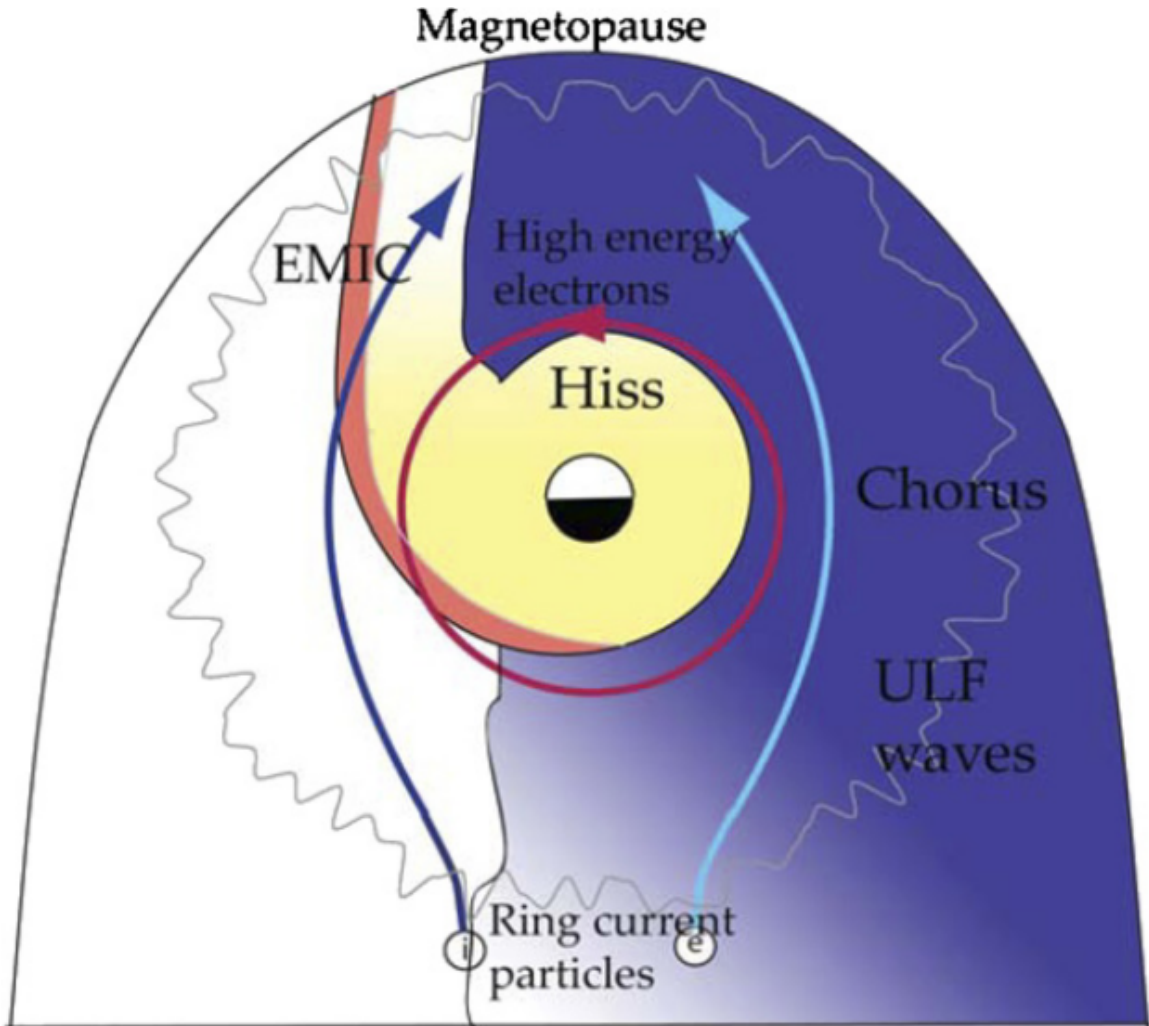


Figure 1.12: Various wave modes in the magnetosphere. Ultra low frequency waves occur through the magnetosphere. Chorus waves are typically observed in the 0-12 midnight-dawn region. EMIC waves are typically observed in the dusk MLT sector. Hiss waves are observed inside the plasmasphere. Figure from Millan and Thorne (2007).

557 Particle Losses

558 Now that we have seen two general mechanisms with which particles are
 559 accelerated and transported in the magnetosphere, we will now consider a few
 560 specific mechanisms with which particles are lost to the atmosphere or the solar
 561 wind. One particle loss mechanism into the solar wind is magnetopause shadowing
 562 (e.g. Ukhorskiy et al., 2006). Particles are sometimes lost when the ring current is
 563 strengthened and Earth's magnetic field strength is increased outside of the ring
 564 current (and reduced on Earth's surface). If the time scale of the ring current
 565 strengthening is slower than a particle drift, J_3 is conserved. Then in order to
 566 conserve J_3 while the magnetic field strength is increased, the particle's drift shell
 567 must move outward to conserve the magnetic flux contained by the drift shell. Then
 568 if the particle's drift shell expands to the point that it crosses the magnetopause, the
 569 particle will be lost to the solar wind.

570 **Move to acceleration?** Another particle loss and acceleration mechanism is driven
 571 by ultra low frequency (ULF) waves and is called radial diffusion. Radial diffusion is
 572 the transport of particles from high to low phase space density, f . If the transport is
 573 radially inward, particles will appear to be accelerated. On the other hand, radially
 574 outward radial diffusion can transport particles through the magnetopause where
 575 they will be lost to the solar wind. Reeves et al. (2013) investigated the driver of
 576 particle acceleration during the October 2012 storm and observationally found that
 577 inward radial diffusion was not dominant, rather local acceleration via wave-resonance
 578 heating (i.e. particle diffusion in pitch angle and energy which will be described below)
 579 appeared to be the dominant acceleration mechanism.

580 The loss mechanism central to this dissertation is pitch angle and energy
 581 scattering of electrons by waves. Some of the waves that scatter electrons in energy
 582 and pitch angle in the inner magnetosphere are: plasmaspheric hiss (e.g. Breneman

583 et al., 2015; O'Brien et al., 2014), EMIC waves (e.g. Capannolo et al., 2019; Hendry
 584 et al., 2017), and chorus waves (e.g. Breneman et al., 2017; Kasahara et al., 2018;
 585 Ozaki et al., 2019). These wave-particle interactions occur when the resonance
 586 condition in Eq. 1.22 is satisfied at which point the particle's energy and α is modified
 587 by the wave. More details regarding the theory of pitch angle and energy diffusion is
 588 given in Chapter X. If the wave changes α towards 0 such that $\alpha < \alpha_{LC}$, the particle's
 589 mirror point lowers to less than 100 km altitude where the particle can be lost due
 590 collisions with air. One manifestation of pitch angle scattering of particles into the
 591 loss cone are microbursts: a sub-second durtaison impulse of electrons.

592

Microbursts

593 Microbursts were first identified in high altitude balloon observations of bremsstrahlung
 594 X-rays emitted by microburst electrons impacting the atmosphere by Anderson and
 595 Milton (1964). Since then, other balloons have observed microburst X-ray signatures
 596 in the upper atmosphere (e.g. Anderson et al., 2017; Barcus et al., 1966; Brown et al.,
 597 1965; Parks, 1967; Trefall et al., 1966; Woodger et al., 2015). In addition to their X-ray
 598 signature, microbursts electrons have been directly observed in LEO with spacecraft
 599 including the Solar Anomalous and Magnetospheric Particle Explorer (SAMPEX),
 600 Focused Investigation of Relativistic Electron Bursts: Intensity, Range, and Dynamics
 601 II (FIREBIRD-II), Science Technologies Satellite (STSAT-I) (e.g. Blake et al., 1996;
 602 Blum et al., 2015; Breneman et al., 2017; Crew et al., 2016; Lee et al., 2012, 2005;
 603 Lorentzen et al., 2001a,b; Nakamura et al., 1995, 2000; O'Brien et al., 2004, 2003).
 604 An example microburst time series is shown in Fig. 1.13 and was observed by
 605 Montana State University's (MSU) FIREBIRD-II CubeSats. The prominent features
 606 of microbursts in Fig. 1.13 are their ± 1 second duration, half order of magnitude
 607 increase in count rate above the falling background, and their approximately 200-800

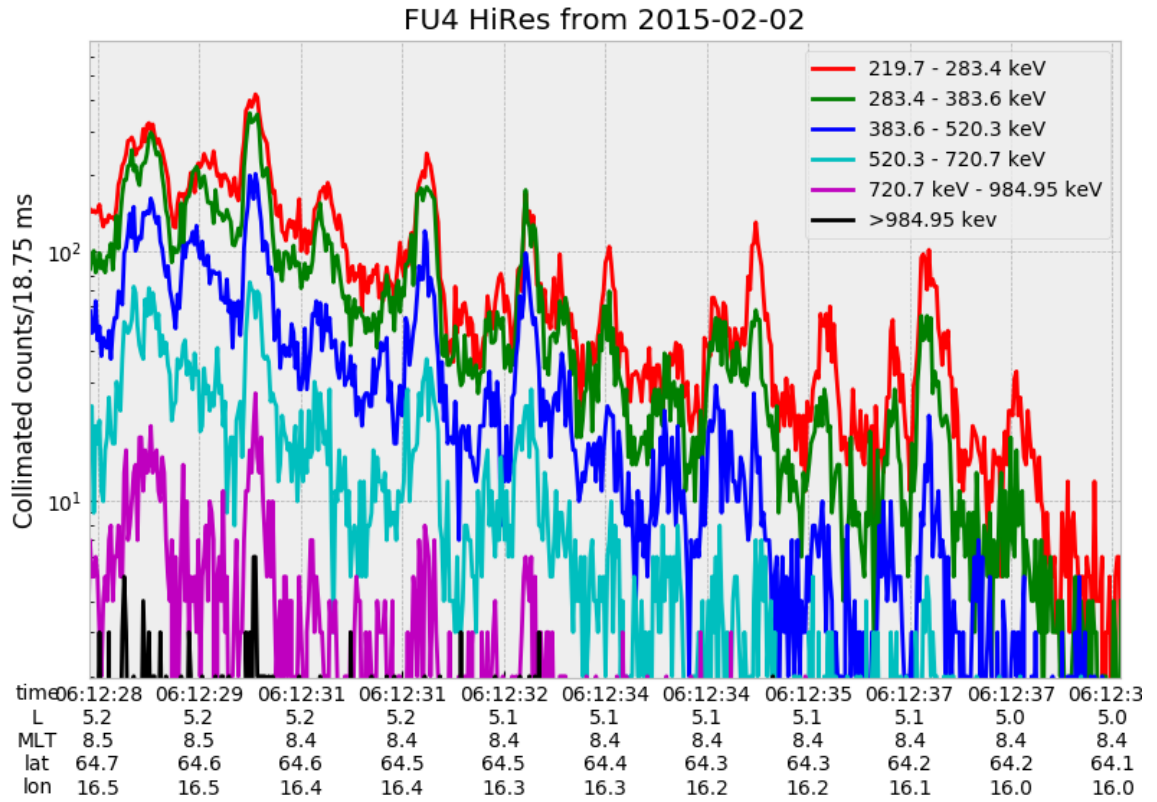


Figure 1.13: An example train of microbursts observed by FIREBIRD-II unit 4 on February 2nd, 2015. The colored curves show the differential energy channel count rates in six channels from ≈ 200 keV to greater than 1 MeV. The x-axis labels show auxiliary information such as time of observation and the spacecraft position in L, MLT, latitude and longitude coordinates.

608 keV energy extent.

609 Microbursts are observed on magnetic field footprints that are connected to the
 610 outer radiation belt (approximately $4 < L < 8$), and are predominately observed in
 611 the 0-12 MLT sector with an elevated occurrence frequency during magnetospherically
 612 disturbed times as shown in Fig. 1.14. Microbursts have been previously observed
 613 over a wide energy range from a few tens of keV (Datta et al., 1997; Parks, 1967) to
 614 greater than 1 MeV (e.g. Blake et al., 1996; Greeley et al., 2019). The microburst

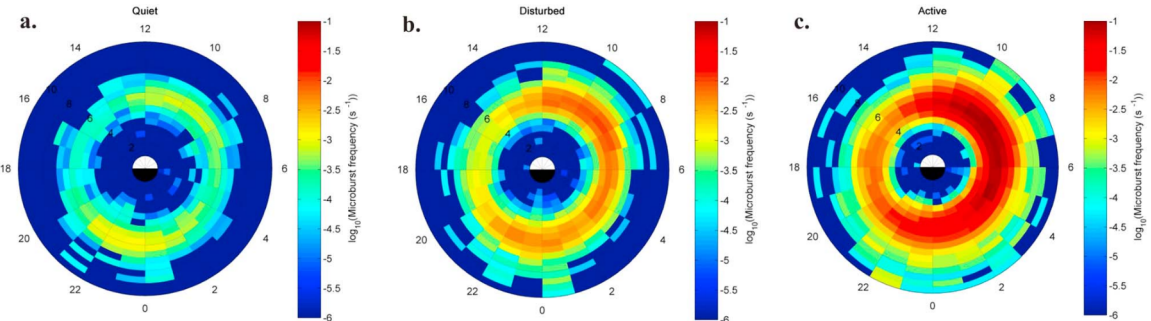


Figure 1.14: Relativistic ($> 1\text{MeV}$) distribution of microburst occurrence rates as a function of L and MLT. The three panels show the microburst occurrence rate dependence on geomagnetic activity, parameterized by the auroral electrojet (AE) index for (a) $\text{AE} < 100 \text{ nT}$, (b) $100 < \text{AE} < 300 \text{ nT}$ and (c) $\text{AE} > 300 \text{ nT}$. Figure from Douma et al. (2017).

615 electron flux (J) falls off in energy, and the microburst energy spectra is typically
 616 well fit to a decaying exponential

$$J(E) = J_0 e^{-E/E_0} \quad (1.23)$$

617 where J_0 is the flux at 0 keV (unphysical free parameter) and E_0 quantifies the
 618 efficiency of the scattering mechanism in energy (.e.g Datta et al., 1997; Lee et al.,
 619 2005; Parks, 1967). A small E_0 suggests that mostly low energy particles are scattered
 620 and a high E_0 suggests that the scattering mechanism scatters low and high energy
 621 electrons. Reality is a bit more messy and a high E_0 may be a signature of a scattering
 622 mechanism preferential to high energy electrons, but is hidden by the convolution of
 623 the source particles available to be scattered (typically with a falling energy spectrum)
 624 and the energy-dependent scattering efficiency.

625 The short duration of microbursts observed by a single LEO satellite has an
 626 ambiguity when interpreting what is exactly a microburst. The two possible realities
 627 are: a microburst is very small and spatially stationary so that the LEO spacecraft

628 passes through it in less than a second. Alternatively, microbursts are spatially large
 629 with a short duration such that the microburst passes by the spacecraft in a fraction
 630 of a second. There are a few ways to distinguish between the two possible realities,
 631 and each one has a unique set of advantages.

632 A high altitude balloon provides essentially a stationary view of the precipitating
 633 particles under the radiation belt footprints so a short-lived, temporal microburst
 634 can be unambiguously identified. Spatial structures on the other hand are difficult
 635 to identify because a balloon is essentially still on drift timescales thus a variation in
 636 the X-rays can be due to the spatial structure or an increase of precipitating particles
 637 over the whole area. Furthermore, if the stationary structure is drifting its particles
 638 are not precipitating into the atmosphere so there is no X-ray signature.

639 Another solution is multi-spacecraft missions that can determine if a microburst
 640 is spatial or temporal. As will be shown in this dissertation, if a microburst is
 641 observed simultaneously by two spacecraft then it is temporally transient and has
 642 a size greater than the spacecraft separation. On the other hand, if two spacecraft
 643 observe a microburst-like feature in the same location and at different times, then it is
 644 spatial may be a curtain (Blake and O'Brien, 2016). Both observational methods have
 645 a unique set of strengths, and this dissertation takes the multi-spacecraft approach
 646 to identify and study microbursts.

647

Scope of Research

648 This dissertation furthers our understanding of the microburst scattering
 649 mechanism by observing the scattering directly, and measuring the microburst sizes
 650 and comparing them to the size of waves near the magnetic equator where those
 651 electrons could have been scattered. Chapter X describes a microburst scattering
 652 event observed by NASA's Van Allen Probes which was studied in the theoretic

653 framework of pitch angle and energy diffusion. The following two chapters will then
654 study the size of microbursts. Chapter Y describes a bouncing packet microburst
655 observation made by MSU's FIREBIRD-II mission where the microburst's lower
656 bound longitudinal and latitudinal sizes were estimated. Then Chapter Z expands
657 the case study from Ch. Y to a statistical study of microburst sizes using The
658 Aerospace Corporation's AeroCube-6 (AC6) CubeSats. In this study, a Monte Carlo
659 and analytic microburst size models were developed to account for the compounding
660 effects of random microburst sizes and locations. Lastly, Ch. A will summarize the
661 dissertation work and make concluding remarks regarding outstanding questions in
662 microburst physics.

663

CHAPTER TWO

664

EVIDENCE OF MICROBURSTS OBSERVED NEAR THE EQUATORIAL

665

PLANE IN THE OUTER VAN ALLEN RADIATION BELT

666

Contribution of Authors and Co-Authors

667 Manuscript(s) in Chapter(s) 1

668

669 Author: [type author name here]

670 Contributions: [list contributions here, single-spaced]

671 Co-Author: [type co-author name here]

672 Contributions: [list contributions here, single-spaced]

673 Co-Author: [type co-author name here]

674 Contributions: [list contributions here, single-spaced]

675

676

Manuscript Information

677 [Type Author and Co-author(s) Names Here]

678 Geophysical Research Letters

679 Status of Manuscript: Published in a peer-reviewed journal

680 Wiley

681 Volume 45, Issue 16

682

Key Points

- 683 ● First report of direct observation of microbursts at high altitude, near the
 684 equatorial plane.
- 685 ● Microbursts' duration, flux enhancement, and energy spectra are similar to prior
 686 observations in LEO.
- 687 ● Microburst generation is not consistent with a single quasi-linear gyroresonant
 688 interaction with chorus waves.

689

Abstract

690 We present the first evidence of electron microbursts observed near the equatorial
 691 plane in Earth's outer radiation belt. We observed the microbursts on March 31st,
 692 2017 with the Magnetic Electron Ion Spectrometer and RBSP Ion Composition
 693 Experiment on the Van Allen Probes. Microburst electrons with kinetic energies
 694 of 29-92 keV were scattered over a substantial range of pitch angles, and over time
 695 intervals of 150-500 ms. Furthermore, the microbursts arrived without dispersion in
 696 energy, indicating that they were recently scattered near the spacecraft. We have
 697 applied the relativistic theory of wave-particle resonant diffusion to the calculated
 698 phase space density, revealing that the observed transport of microburst electrons is
 699 not consistent with the hypothesized quasi-linear approximation.

700

Introduction

701 Since the Van Allen radiation belts were discovered by Van Allen (1959) and
 702 Vernov and Chudakov (1960), decades of work has focused on understanding their
 703 origins and effects on the near-Earth space environment and ionosphere-thermosphere

704 system. The energy content of the outer belt is dominated by energetic electrons,
 705 with dynamics controlled by a complex interplay between various source and loss
 706 mechanisms. One important loss and acceleration mechanism is gyroresonant
 707 diffusion in energy and pitch angle (PA) due to scattering of electrons by plasma
 708 waves (e.g. Bortnik et al., 2008; Horne and Thorne, 2003; Meredith et al., 2002;
 709 Millan and Thorne, 2007; Summers et al., 1998; Thorne and Andreoli, 1981; Thorne
 710 et al., 2005; Walker, 1993).

711 Chorus waves are commonly associated with PA and energy diffusion. These
 712 waves are typically generated by substorm injections into the inner magnetosphere,
 713 which lead to a temperature anisotropy of the source electrons with energies up to
 714 tens of keV (e.g. Horne et al., 2003; Li et al., 2009a). Since these source electrons
 715 drift eastward, chorus is most frequently observed in the dawn sector, but it has
 716 been observed at all magnetic local times (MLT) (Li et al., 2009b). Chorus waves
 717 are believed to generate electron microburst precipitation through wave-particle
 718 interactions.

719 Microbursts are typically defined as an increase of electron flux in or near the
 720 atmospheric loss cone that last < 1 s (e.g. Anderson and Milton, 1964; Blake et al.,
 721 1996; Lorentzen et al., 2001a). Empirical and theoretical analyses indicate that
 722 microbursts are an important loss process since they can substantially deplete the
 723 radiation belt electrons on the order of one day (e.g. Breneman et al., 2017; Lorentzen
 724 et al., 2001b; O'Brien et al., 2004; Thorne et al., 2005). Previously, microbursts have
 725 been observed in the upper atmosphere in the form of bremsstrahlung X-rays (e.g.
 726 Anderson et al., 2017; Parks, 1967; Woodger et al., 2015) and directly in low Earth
 727 orbit (LEO) (e.g. Blake et al., 1996; Blum et al., 2015; Breneman et al., 2017; Crew
 728 et al., 2016; Lee et al., 2012, 2005; Lorentzen et al., 2001a,b; Mozer et al., 2018;
 729 Nakamura et al., 1995, 2000; O'Brien et al., 2004, 2003).

We observed for the first time, microburst-like signatures near their hypothesized origin within the heart of the outer radiation belt. The unique microburst observations we report here were possible with the Van Allen Probe-A's (RBSP-A) Magnetic Electron Ion Spectrometer's (MagEIS) fast sampling rate (~ 11 ms), and RBSP Ion Composition Experiment's (RBSPICE) PA coverage. The observed microbursts' duration, energy spectra, and energy dispersion signature were similar to microbursts previously reported from LEO. Furthermore, we simultaneously observed structureless "hiss-like" whistler mode wave power in the lower band chorus frequency range (Li et al., 2012). From previous observations in LEO (e.g. Blake et al., 1996), it is believed that microbursts result from the impulsive scattering of electrons into or near the loss cone, which is on the order of a few tens of degrees in LEO. With this assumption, high altitude microburst observations near the magnetic equator should be very difficult to make since the atmospheric loss cone there is only a few degrees wide. Thus, the loss cone is smaller than the angular resolution of most particle detectors. Even when an instrument is observing the loss cone, the instrument's field of view will include some portion of the trapped population. The trapped electron flux is typically orders of magnitude higher than that in the loss cone, so that microbursts scattered into the loss cone will be obscured. We present observational evidence that suggests that the sudden impulse of electrons studied here is consistent with the creation of microbursts. Furthermore, these microbursts were scattered over a broad PA range outside of the loss cone, though the loss cone was not directly observed by MagEIS and RBSICE.

This paper explores the properties of the observed microbursts by utilizing in-situ RBSP measurements of waves and particles. This unique high altitude point of view enables us to test whether the observed microburst scattering is consistent with a quasi-linear diffusion process. We have tested this hypothesis with in-situ electron

756 phase space density (PSD) measurements and the relativistic theory of wave-particle
 757 resonant diffusion (Summers et al., 1998; Walker, 1993) to determine if the microburst
 758 electrons diffused in PA and energy.

759 Spacecraft Instrumentation

760 NASA's RBSP mission (Mauk et al., 2013), launched on August 30th, 2012,
 761 consists of a pair of identically instrumented spacecraft. Their orbit and instru-
 762 mentation are uniquely configured to enrich our understanding of the particles and
 763 waves in the inner magnetosphere. The RBSP spacecraft are in highly elliptical, low-
 764 inclination orbit, with perigee of \sim 600 km and apogee of \sim 30,000 km altitude. Their
 765 attitude is maintained by spin-stabilization with a period of \sim 11 s and the spin axis is
 766 roughly sun-pointing. In this analysis, energetic electron measurements from MagEIS
 767 (Blake et al., 2013) and RBSPICE (Mitchell et al., 2013) were used, complemented by
 768 magnetic field and wave measurements from Electric and Magnetic Field Instrument
 769 and Integrated Science (EMFISIS) (Kletzing et al., 2013).

770 We observed these microbursts with RBSP-A's MagEIS low energy instrument
 771 (MagEIS-A) which measures 20-240 keV electrons. It has an angular acceptance
 772 of $3^\circ - 10^\circ$ in the spacecraft spin plane, and 20° perpendicular to the spin plane.
 773 MagEIS-A has a high rate data mode which samples at 1000 angular sectors per
 774 spacecraft spin (11 ms cadence). MagEIS low on RBSP-B on the other hand samples
 775 at 64 angular sectors per spacecraft spin (172 ms cadence), so it was only used for
 776 context.

777 To expand the PA coverage of MagEIS-A, we used the RBSPICE-A time-of-
 778 flight instrument. RBSPICE-A measures electron energies in the range of 19 keV -
 779 1 MeV with a fan of six telescopes (the sixth telescope is used only for calibration
 780 and was excluded from this analysis). These telescopes have an overall acceptance

781 angle of 160° by 12° which allows them to simultaneously sample a substantial part
 782 of the Pitch Angle Distribution (PAD). RBSPICE-A gathers data over 32 sectors
 783 per spacecraft spin (≈ 310 ms cadence) and each sector is divided into three sub-
 784 sectors corresponding to three measurement modes (Manweiler and Zwiener, 2018).
 785 At the time of the observation, the sub-sector used for electron measurements had
 786 an accumulation time of 77 ms. We used RBSPICE-A's Electron Basic Rate (EBR)
 787 telemetry data in this analysis which is not averaged, though it is an integral energy
 788 channel.

789 To understand the dynamics of the local magnetic field, we used the EMFISIS
 790 instrument. EMFISIS provides measurements of the DC magnetic field with flux gate
 791 magnetometers. In addition, it measures electromagnetic waves from 10 Hz to 500
 792 kHz with search coil magnetometers. The spectral matrix and burst data products
 793 used in this analysis were from the EMFISIS waveform receiver (WFR) (10 Hz - 12
 794 kHz) and the high frequency receiver (10 kHz - 500 kHz). Burst data were selectively
 795 captured at a 35 kHz sample rate, and the survey mode spectral matrix data was
 796 captured every 6s.

797

Observations

798 MagEIS-A and RBSPICE-A observed the microburst-like signatures on March
 799 31st, 2017 at $L^* \approx 6$ and $MLT \approx 19$, calculated with the Tsyganenko 2004 magnetic
 800 field model (Tsyganenko and Sitnov, 2005). The magnetosphere was in the recovery
 801 phase of a storm, with minimum Dst of -75 nT observed on March 27th. The local
 802 electron number density was on the order of 1 cm^{-3} at this time, so both RBSP
 803 spacecraft were located outside the plasmasphere. The two spacecraft were separated
 804 by 1700 km, at magnetic latitudes $\lambda \approx -19^\circ$ and $\lambda \approx -18^\circ$ for RBSP-A and RBSP-B,
 805 respectively.

806 MagEIS-A observed microburst electron flux (J) at energies ≥ 92 keV around
 807 11:17 UT as shown in panel (a) in Fig. 2.1. For directional information, panel (b)
 808 in Fig. 2.1 shows flux as a function of local pitch angle (α_L) and time for 46-66 keV
 809 electrons. Electrons that traveled towards the northern hemisphere had $\alpha_L < 90^\circ$ and
 810 southern hemisphere had $\alpha_L > 90^\circ$. The interval between the two vertical dashed
 811 black lines contain the four microbursts examined in this study. We observed these
 812 microbursts at $\alpha_L < 50^\circ$, but MagEIS-A did not sample into the 0° loss cone.

813 Figure 2.1 panel (c) shows the EMFISIS WFR data from RBSP-A. Between
 814 11:17:05 and 11:17:10 UT, we observed an isolated burst of whistler mode wave power
 815 in the frequency range $0.1 < \omega < 0.3 \Omega_{ce0}$, where Ω_{ce0} is the equatorial electron
 816 gyrofrequency. No individual rising or falling tone elements were observed during
 817 this period, and the waves appeared more “hiss-like” (e.g. Li et al., 2012). This wave
 818 was near-parallel propagating (evidence shown in Appendix A) and about 10 minutes
 819 later, weak chorus rising tone elements were observed (not shown).

820 Panels (d)-(f) in Fig. 2.1 are in the same format as panels (a)-(c), but for RBSP-
 821 B. An injection or boundary was observed with RBSP-B at 11:16:50 UT and RBSP-A
 822 observed a similar feature soon after 11:18 UT (not shown).

823 A zoomed-in version of Fig. 2.1 panels (a) and (b) is shown in Fig. 2.2. Panel
 824 (a) shows the four microburst-like signatures observed between 11:17:10 and 11:17:12
 825 UT, at energies up to 92 keV. The observed duration of the microbursts was 150
 826 - 500 ms, and they did not arrive dispersed in energy, which indicates that they
 827 were recently scattered near the spacecraft location. We use IRBEM-Lib, a library
 828 dedicated to radiation belt modeling (Boscher et al., 2012), to calculate the mirror
 829 point altitudes, which were found to be above LEO. Panel (b) shows the RBSPICE-
 830 A EBR time series with the group of microbursts observed at the same time as
 831 in panel (a). To understand the timing relationship between the MagEIS-A and

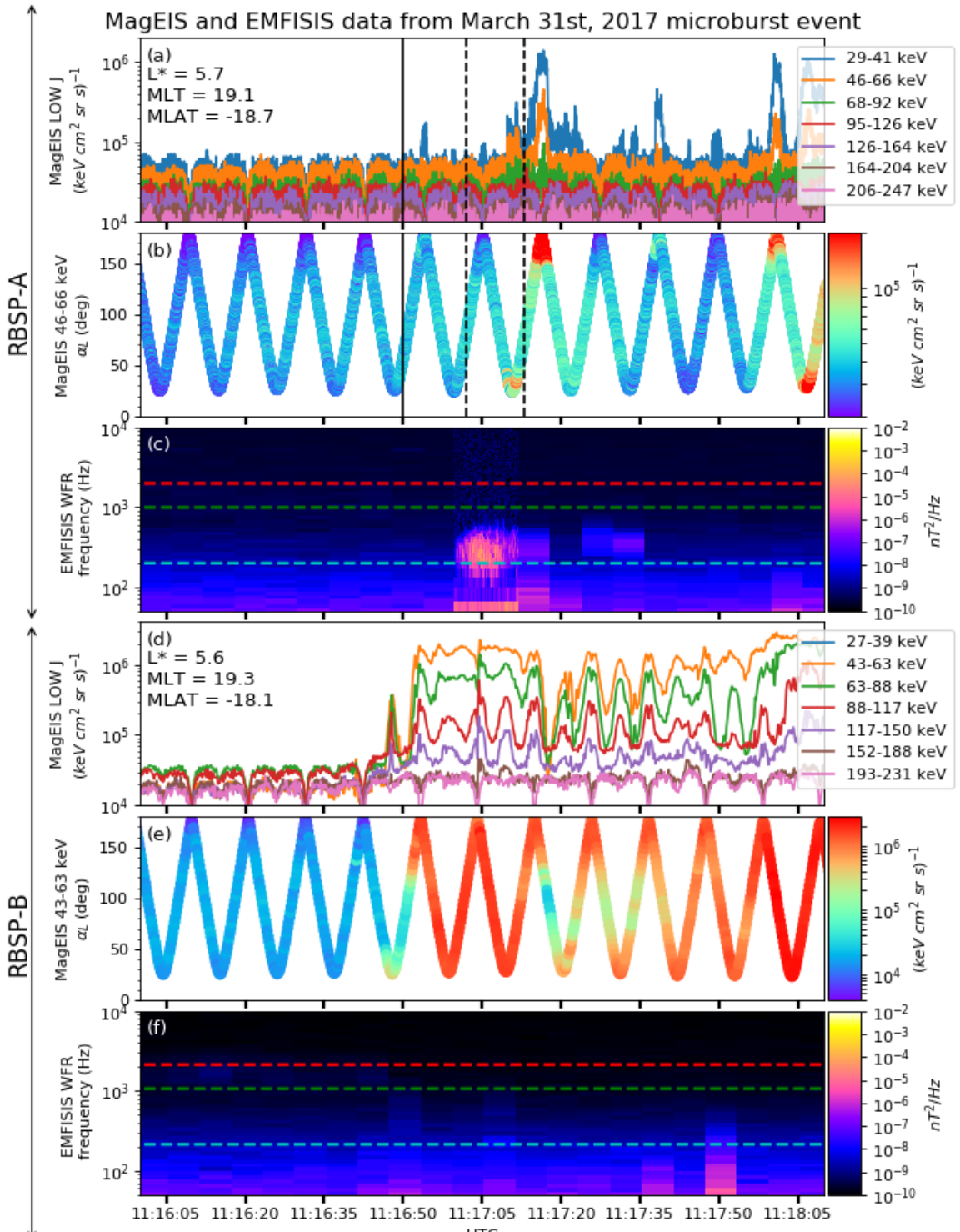


Figure 2.1: Electron and wave conditions from the MagEIS-A and EMFISIS WFR sensors for the microburst time interval. Panels (a), (b), and (c) are from RBSP-A with its position information annotated in panel (a). Panels (d), (e), and (f) are from RBSP-B with its position information annotated in panel (d). Panel (a) is the MagEIS-A high rate timeseries. Panels (b) and (e) show the evolution of the MagEIS-A J as a function of α_L from the ~ 40 to ~ 60 keV channel. Every 10th point is shown in panel (b). The solid black line in panels (a) and (b) mark the end of the time period used for the PSD fit extrapolation analysis explained in section

832 RBSPICE-A observations, we marked the times when MagEIS-A observed the four
 833 microbursts by vertical black arrows in panels (a) and (b). MagEIS-A observed the
 834 first microburst ~ 0.5 s before RBSPICE-A. The bounce period of locally mirroring,
 835 100 keV electrons was ~ 0.8 s, so this was unlikely to have been a returning bounce.
 836 This evidence confirms that these microburst signatures are packets of electrons and
 837 not a boundary moving back and forth at RBSP-A's location. To understand the
 838 PA extent of these microbursts, panel (c) shows the 29-41 keV MagEIS-A J and
 839 RBSPICE-A EBR as a function of α_L and time. The microburst J was observed
 840 by MagEIS-A between $25^\circ < \alpha_L < 50^\circ$ and RBSPICE-A between $100^\circ < \alpha_L < 160^\circ$,
 841 with the highest intensities close to $\alpha_L = 90^\circ$. RBSPICE-A observed a 10-80%
 842 enhancement in count rate over those PAs with the evidence presented in Appendix
 843 A.

844

Analysis

845 First, we estimated the microburst energy spectra. For each microburst shown in
 846 Fig. 2.2, its flux was averaged and baseline subtracted using the method from O'Brien
 847 et al. (2004) and then fit with an exponential function. The calculated exponential
 848 E-folding energy was found to vary between 25 and 35 keV, which is consistent with
 849 spectra derived from prior measurements (Datta et al., 1997; Lee et al., 2012, 2005).

850 We then tested the hypothesis that the microburst electrons were transported
 851 in energy and PA by a single chorus wave. We used a procedure similar to sections
 852 3.1 and 4.5 in Meredith et al. (2002) which we describe below.

853 Microburst and Source PSD

854 We estimated the electron PSD, $f(p_\perp, p_\parallel)$ where p_\perp and p_\parallel are the perpendicular
 855 and parallel components of the electron momentum relative to the local magnetic field,

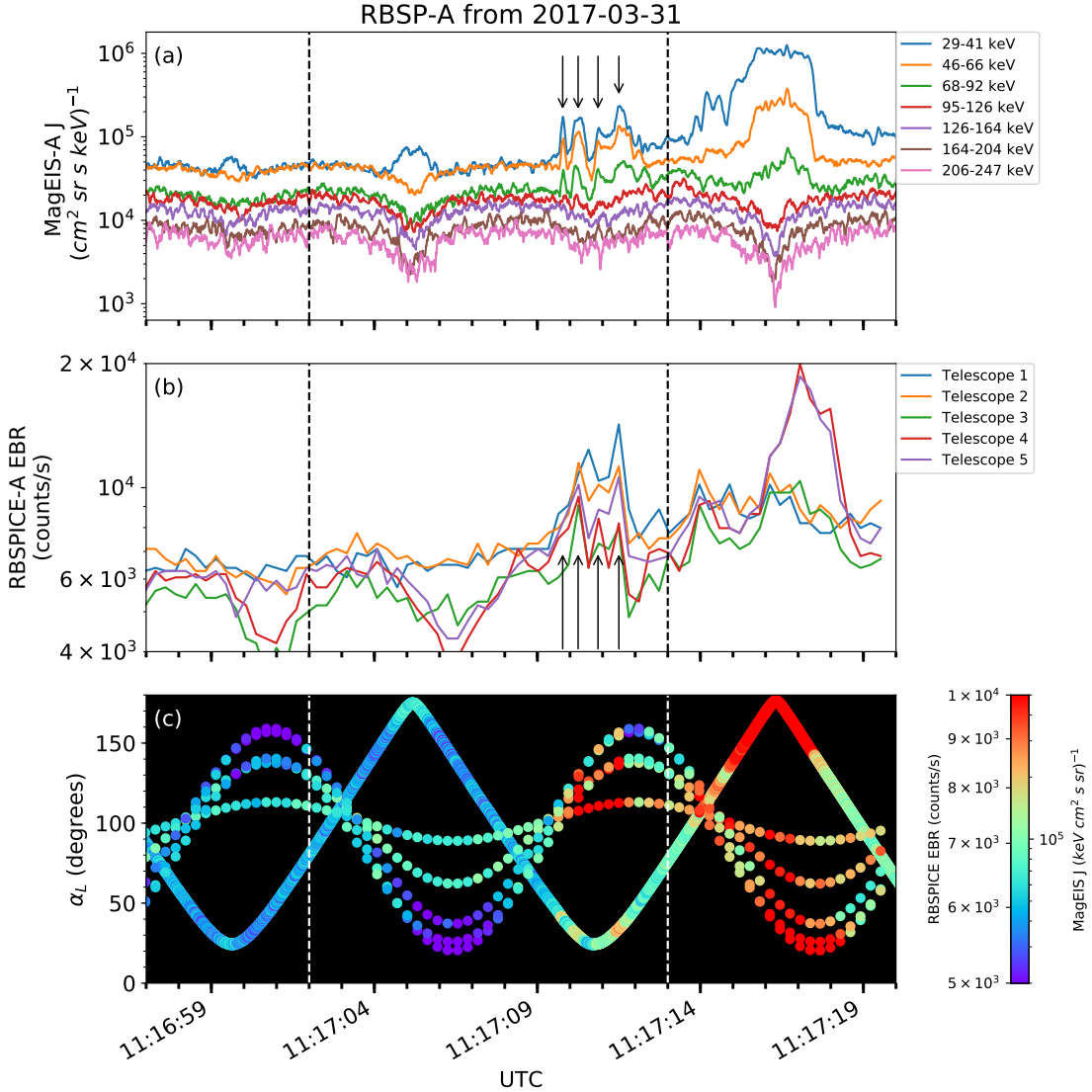


Figure 2.2: Panel (a) shows the MagEIS-A high rate timeseries. Panel (b) shows the RBSPIKE EBR count rate timeseries for $\zeta = 19$ keV electrons. The microbursts were observed between 11:17:10 - 11:17:12 UT and are indicated with the vertical black arrows in panels (a) and (b) for MagEIS-A times. Panel (c) shows the RBSPIKE EBR (family of relatively sparse sampled curves) and MagEIS-A J from the 29-41 keV energy channel (single curve) as a function of α_L . The vertical dashed lines show the time interval for the PSD analysis.

for the microburst time period. MagEIS-A $J(E, \alpha_L)$ was averaged between 11:17:02 and 11:17:13 UT and binned by α_L into 5° bins. Then, we assumed the conservation of the first adiabatic invariant and mapped α_L to equatorial PA, α_{eq} . The binned $J(E, \alpha_{eq})$ was then converted to $f(p_\perp, p_\parallel)$ via

$$f(p_\perp, p_\parallel) = \frac{J(E, \alpha_{eq})}{p^2}, \quad (2.1)$$

where $p = \sqrt{p_\perp^2 + p_\parallel^2}$. Lastly, α_{eq} was used to separate p into p_\perp and p_\parallel via

$$\frac{p_\parallel}{m_e c} = \frac{\sqrt{E(E + 2E_0)} \cos(\alpha_{eq})}{E_0} \quad (2.2)$$

$$\frac{p_\perp}{m_e c} = \frac{\sqrt{E(E + 2E_0)} \sin(\alpha_{eq})}{E_0} \quad (2.3)$$

where c is the speed of light, E is the kinetic energy, m_e is the electron mass, and E_0 is the electron rest energy. The observed $f(p_\perp, p_\parallel)$ in dimensionless momentum space is shown in Fig. 2.3 in all panels between the p_\parallel axis and the white dotted lines. The bright spot in $f(p_\perp, p_\parallel)$ in the upper p_\parallel plane represents the four microbursts. Along with the observed PSD, we use Fig. 2.3 to explore the various PSD extrapolation and diffusion model assumptions which are described below.

We proceed under the assumption that the source of the microburst electrons is not likely to be at the latitude of the observation, and is closer to the magnetic equator. To look for a source of microburst electrons, we extrapolate the unobserved $f(p_\perp, p_\parallel)$ of electrons with $|\lambda_m| < 19^\circ$ using two cases with a 90° -peaked PAD of the form

$$f(E, \alpha_{eq}) = f_0(E) \sin^n(\alpha_{eq}) \quad (2.4)$$

where $f_0(E)$ is a scaling parameter and n is a power parameter. Similarly to the

868 in-situ $f(p_{\perp}, p_{\parallel})$, the $f(E, \alpha_{eq}) \mapsto f(p_{\perp}, p_{\parallel})$ conversion was applied.

869 In the first case, we fitted Eq. 2.4 to the quiet time $J(E, \alpha_{eq})$ from 11:15:00 to
 870 11:16:50 UT (end time shown as the black vertical line in Fig. 2.1). The fitted
 871 PAD was relatively flat with $0.4 < n < 0.5$ and highest magnitude of f_0 was
 872 $0.05 c^3/(cm MeV)^3$. This extrapolated $f(p_{\perp}, p_{\parallel})$ is shown in Fig. 2.3 panels (A) and
 873 (E), between the dotted white lines for scattering at $\lambda = 0^\circ$ and 20° , respectively.
 874 To confirm the relatively low n parameter, we found times where RBSP-A was in
 875 a similar L-MLT location, but closer to the magnetic equator. At 2 and 19 UT on
 876 the same day, we fit the $J(E, \alpha_{eq})$, and the fit parameters were very similar to the
 877 pre-microburst $f(p_{\perp}, p_{\parallel})$ at 11 UT. Thus it is a reasonable assumption that $f(p_{\perp}, p_{\parallel})$
 878 was relatively flat near the equator.

879 In the other case, we estimate how large n would have to be in order to find
 880 sufficient PSD in MagEIS-A's energy range to be a source of the microburst electrons.
 881 We used $n \in \{1, 2, 4\}$ and we forced the $f_0(E)$ parameter to match the observed
 882 $f(p_{\perp}, p_{\parallel})$ at the most equatorial PAs observed by MagEIS-A. These extrapolations
 883 are shown in columns 2-4 in Fig. 2.3. There was enough source PSD anywhere in
 884 MagEIS-A's energy range only if $n \geq 2$.

885 Motion of resonant electrons in phase space

To calculate the motion of resonant electrons in momentum space, we used the relativistic theory of wave-particle resonant diffusion developed by Walker (1993) and Summers et al. (1998) and applied in Meredith et al. (2002). The chorus wave can modify $f(p_{\perp}, p_{\parallel})$ when a resonance condition is satisfied. The cyclotron resonance condition between an electron with velocity $v = \sqrt{v_{\parallel}^2 + v_{\perp}^2}$ and a parallel propagating

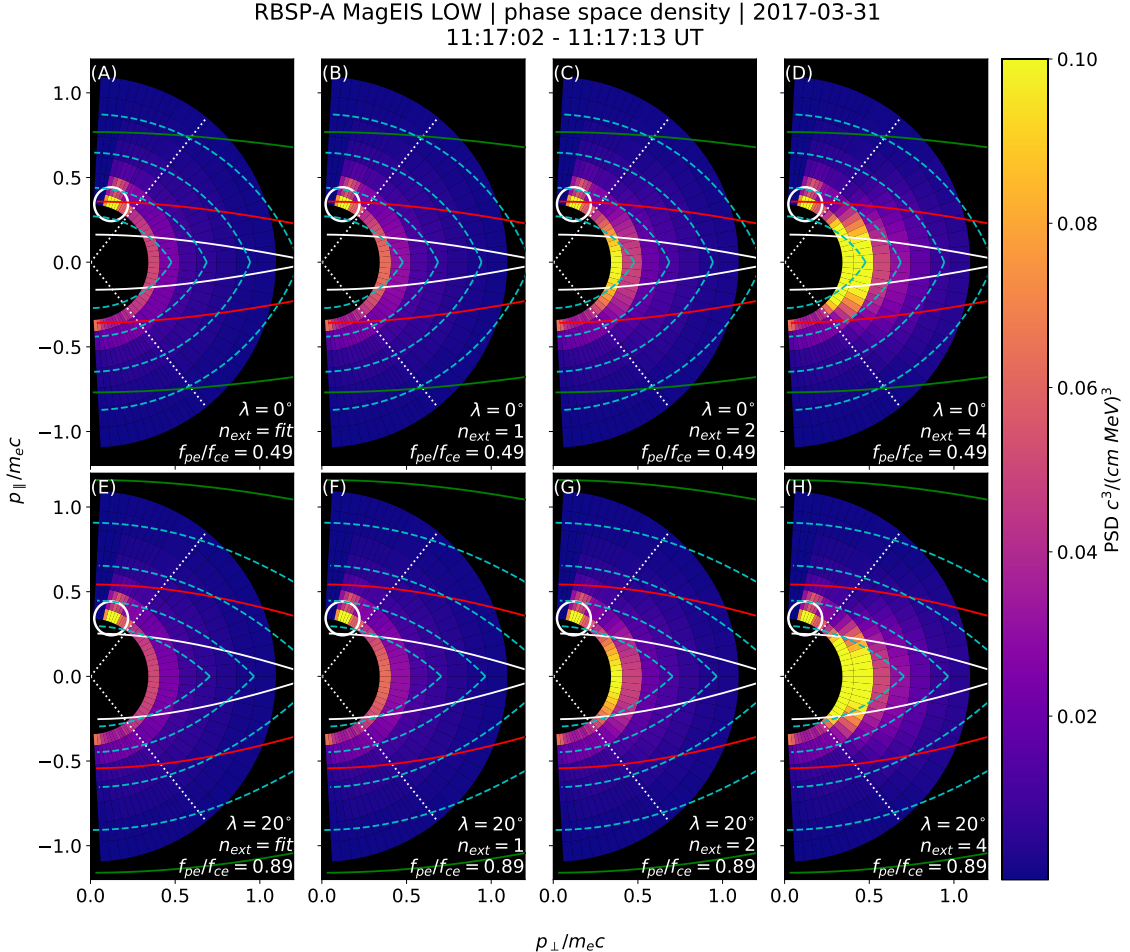


Figure 2.3: The colored annulus represents $f(p_{\perp}, p_{\parallel})$ in normalized momentum space, parallel and perpendicular to the background magnetic field. The microburst $f(p_{\perp}, p_{\parallel})$ is highlighted with the white circle. The columns show different powers of the sine extrapolation, and rows show the different magnetic latitudes of the scattering. The white dotted traces represent the boundary between the data and extrapolation. The green, red, and white solid traces are the resonance curves for $\omega = 0.2\Omega_{ce}$, $0.4\Omega_{ce}$, $0.6\Omega_{ce}$, respectively. The cyan dashed traces are the diffusion curves for a $\omega = 0.4\Omega_{ce}$ wave (waves of other frequency have similar diffusion curves). The magnetic latitude of the scattering, the ratio of the plasma to the cyclotron frequency, and the power of the sine extrapolation is annotated in each panel. For the resonance and diffusion curves, the density model assumed a $n_L = 1 e^-/cm^3$ and $\psi = -1$.

wave of frequency ω and wave number k_{\parallel} is given by

$$\omega - v_{\parallel} k_{\parallel} = \frac{\Omega_{ce}}{\gamma}, \quad (2.5)$$

where Ω_{ce} is the electron gyrofrequency at the scattering location, and γ is the relativistic correction. Assuming the cold plasma approximation,

$$k_{\parallel} = \frac{\omega}{c} \sqrt{1 - \frac{\omega_{pe}^2}{\omega(\omega - |\Omega_{ce}|)}}, \quad (2.6)$$

where ω_{pe} is the plasma frequency. For a particular set of parameters, Eq. 2.5 defines a curve in momentum space that describes which electrons will resonate with a monochromatic wave.

To calculate k_{\parallel} , we approximated the electron number density, $n_e(\lambda)$ locally and at the magnetic equator. Locally, the plasma density was approximately $n_e(\lambda = -20^\circ) = n_L \approx 1 \text{ cm}^{-3}$. We used magnetospheric seismology techniques (e.g. Takahashi and Denton, 2007) to parameterize $n_e(\lambda)$ elsewhere along the field line with

$$n_e(\lambda) = n_e(0) \left(\frac{LR_e}{R(\lambda)} \right)^{\psi} \quad (2.7)$$

where R_e is the Earth's radius, $R(\lambda)$ is the radial distance from the Earth to the spacecraft, and ψ is the exponent parameter. Assuming a dipole magnetic field for which $R(\lambda) = LR_e \cos^2 \lambda$ (e.g. Schulz and Lanzerotti, 1974), we can express Eq. 2.7 in terms of n_L via

$$n_e(\lambda) = n_L \left(\frac{\cos \lambda_L}{\cos \lambda} \right)^{2\psi} \quad (2.8)$$

where we used $\psi = -1$ (higher density at the magnetic equator) in this analysis. We chose this exponent parameter because it is a realistic best case scenario for the

896 electrons to be transported along the diffusion curves (described below).

Walker (1993) and Summers et al. (1998) argued that a resonant electron will move along diffusion curves in momentum space. A diffusion curve is derived as follows. In the reference frame moving with a monochromatic chorus wave's phase velocity (wave frame), the chorus wave is stationary and there is no electric field. Thus in the wave frame, the electron's kinetic energy is conserved, and the electron's velocity in the wave frame can be expressed in differential form as

$$v_{\parallel}dv_{\parallel} + v_{\perp}dv_{\perp} = 0. \quad (2.9)$$

After a Lorentz transformation of Eq. 2.9 into the magnetosospheric frame, kinetic energy will no longer be conserved. After integration and manipulation of Eq. 2.9, we obtain:

$$\left(1 - \frac{u_0^2 v_0^2}{c^4}\right)v_{\parallel}^2 - 2u_0\left(1 - \frac{v_0^2}{c^2}\right)v_{\parallel} + \left(1 - \frac{u_0^2}{c^2}\right)v_{\perp}^2 = v_0^2 - u_0^2 \quad (2.10)$$

897 where $u_0 = \omega/k_{\parallel}$ is the phase velocity, and v_0 is a constant of integration (Summers
898 et al., 1998; Walker, 1993). Equation 2.10 defines a family of diffusion curves in
899 momentum space on which resonant electrons will move. The distance that an
900 electron moves along a diffusion curve is a function of wave and plasma parameters,
901 and is estimated from the magnitude of the diffusion coefficients and the resonance
902 time.

903 Comparing the microburst PSD to diffusion theory

904 Superposed on the PSD plots in Fig. 2.3 are resonance curves for chorus waves
905 of $\omega = 0.2\Omega_{ce}$, $0.4\Omega_{ce}$, $0.6\Omega_{ce}$ and a few diffusion curves for a $\omega = 0.4\Omega_{ce}$ wave.
906 These curves were parameterized by λ using a dipole magnetic field for $\lambda = 0^\circ$

(Fig. 2.3, panels A-D) and $\lambda = 20^\circ$ (Fig. 2.3, panels E-H). If the transport of microburst electrons is consistent with gyro-resonant diffusion, a diffusion curve that passes through the microburst $f(p_\perp, p_\parallel)$ must also pass through another region with at least the same magnitude PSD ($f(p_\perp, p_\parallel) \geq 0.1 \text{ c}^3/(\text{cm MeV})^3$) e.g. Fig. 2.3, panel (D). With this constraint, an artificially high extrapolated $f(p_\perp, p_\parallel)$ with $n > 2$ (5 times larger than calculated from the fits) must be assumed for there to have been a sufficient source of PSD anywhere in MagEIS-A's energy range.

We now show that by comparing MagEIS observations with theory, that the minimum wave amplitude necessary to scatter these electrons is much higher than was observed by EMFISIS-A. If we assume a unrealistic PAD with enough PSD just equatorward of RBSP-A, we can use MagEIS-A observations to calculate the minimum $\Delta\alpha_{eq}$ that the electrons were transported. We then used diffusion theory to calculate the necessary wave amplitude. For microbursts with larger PAs, MagEIS-A observed a transport of $\Delta\alpha_{eq} = 9^\circ$ and for microbursts with smaller PAs, the observed transport was $\Delta\alpha_{eq} = 24^\circ$. The required wave amplitude was calculated with Eq. 3 from Thorne and Andreoli (1981) assuming a maximum resonance period of a quarter bounce. The observed change in PA requires a wave amplitude $0.2 < |B_w| < 0.5 \text{ nT}$. For a few brief moments, the EMFISIS-A WFR waveform data showed $0.1 < |B_w| < 0.15 \text{ nT}$, so a transport of 9° is plausible, but not likely for 24° .

Another source of microburst electrons may be from energies below MagEIS-A's range. The Helium, Oxygen, Proton, and Electron mass spectrometer (Funsten et al., 2013) on RBSP-A observed $f(p_\perp, p_\parallel) \geq 0.1 \text{ c}^3/(\text{cm MeV})^3$ for $\pm 23 \text{ keV}$ electrons at this time. We then assumed the wave amplitude derived above to predict the transport in energy. We used the fact that the momentum and pitch angle diffusion coefficients, D_{pp} and $D_{\alpha\alpha}$ are related via $D_{pp}/p^2 \sim D_{\alpha\alpha}$ or equivalently, $\Delta p/p \sim \Delta\alpha$. The observed PA transport corresponds to an energy transport of $6 < \Delta E < 16$

keV. Therefore, this wave can transport 23 keV electrons from smaller pitch angles to larger pitch angles and would be observed in the 29 – 41 keV MagEIS-A channel. However, this wave is insufficient to transport electrons to the 68 – 92 keV channel in one interaction. Therefore we conclude that quasi-linear diffusion cannot explain the observed microbursts.

938

Discussion and Conclusions

These novel observations of impulsive electron signatures reported here fall well within the broad definition of a microburst as described in section 3. Their properties were similar to microbursts observed in LEO, with an E-folding energy of $25 < E_0 < 35$ keV (Datta et al., 1997; Lee et al., 2012, 2005), duration of 150-500 ms (Lorentzen et al., 2001a), observed upper energy limit of 92 keV, and a lack of clear energy dispersion (Breneman et al., 2017). With MagEIS-A’s high time and energy resolution, we conclude that these dispersionless microbursts were recently scattered near the spacecraft. Furthermore, RBSPICE-A’s PA coverage suggests that these electrons were scattered over a substantial range of PAs, with the highest intensities near $\alpha_L = 90^\circ$. Overall, our observational evidence suggests that on time scales shorter than one bounce period, the chorus wave effectively accelerated trapped electrons over a broad PA range.

In the theoretical framework of wave-particle resonant diffusion applied to the observed PSD in section 3, we determine that the observed scattering is not consistent with the quasi-linear approximation. The nearest source of sufficient PSD is too far away in phase space to have been transported by the hypothesized quasi-linear process over a timescale shorter than one bounce period (one interaction). A similar conclusion was made by Mozer et al. (2018) who used quasi-linear theory constrained by RBSP wave measurements. They successfully modeled the one second average

958 precipitating flux observed with AeroCube-6 (AC-6) CubeSats during a conjunction,
 959 but they were unable to model the AC-6 fluxes on smaller time scales.

960 To put these microburst observations into a wider magnetospheric perspective,
 961 we observed them during the recovery phase of a minimum Dst of -75 nT storm, a
 962 statistically favorable time period for microbursts (O'Brien et al., 2003). Furthermore,
 963 during the same storm on March 27th, the Arase spacecraft observed highly correlated
 964 lower band chorus with 10-50 keV electron precipitation inside the loss cone. At
 965 that time, Arase's magnetic field footprint was near The Pas All-Sky Imager (part
 966 of the THEMIS mission) which simultaneously observed pulsating auroral patches
 967 (Kasahara et al., 2018). While microbursts and pulsating auroral patches have not
 968 been clearly connected, they are both believed to be a product of electron scattering
 969 by whistler mode waves (e.g. Lorentzen et al., 2001a; Nishimura et al., 2011; O'Brien
 970 et al., 2003; Ozaki et al., 2012).

971 The combined capabilities of the various RBSP wave and particle instruments
 972 enable comprehensive studies of wave-particle scattering and the resulting microburst
 973 precipitation. From a preliminary search by the authors, other microburst-like
 974 signatures have been found with RBSP. Similar to previous studies (e.g. Blum et al.,
 975 2015; O'Brien et al., 2003), a statistical study of high-altitude microbursts in L-MLT
 976 space needs to be conducted before we can verify that these microbursts are the
 977 counterpart of the microbursts observed in LEO and the upper atmosphere.

978

Acknowledgments

979 The authors acknowledge the technicians, engineers, and scientists who made the
 980 RBSP and AC-6 missions possible. One author (Shumko) would like to acknowledge
 981 Dana Longcope for his help in understanding the quasi-linear diffusion theory. Dr.
 982 Gkioulidou was supported by JHU/APL subcontract 131803 to the NJIT under NASA

983 Prime contract NNN06AA01C. EMFISIS work was supported by JHU/APL contract
984 no. 921647 under NASA Prime contract No. NAS5-01072. The MagEIS instrument
985 was funded by NASA's Prime contract no. NAS5-01072. The level 3 MagEIS-A
986 "high rate" data is available in the Supporting Information, level 1 RBSPICE EBR
987 data is archived at <http://rbspicea.ftecs.com/>, and the EMFISIS level 2 spectral
988 matrix and burst data as well as the level 3 magnetometer data is archived at
989 <http://emfisis.physics.uiowa.edu/data/index>. The IRBEM Library can be obtained
990 at irbem.sf.net.

CHAPTER THREE

991
992 MICROBURST SCALE SIZE DERIVED FROM MULTIPLE BOUNCES OF A
993 MICROBURST SIMULTANEOUSLY OBSERVED WITH THE FIREBIRD-II
994 CUBESATS

995 Contribution of Authors and Co-Authors

996 Manuscript(s) in Chapter(s) 1

997

998 Author: [type author name here]

999 Contributions: [list contributions here, single-spaced]

1000 Co-Author: [type co-author name here]

1001 Contributions: [list contributions here, single-spaced]

1002 Co-Author: [type co-author name here]

1003 Contributions: [list contributions here, single-spaced]

1004

1005

Manuscript Information

1006 [Type Author and Co-author(s) Names Here]

1007 Geophysical Research Letters

1008 Status of Manuscript: Published in a peer-reviewed journal

1009 Wiley

1010 Volume 45, Issue 17

1011

Key Points

1012

- Multiple bounces from a microburst were observed by the two FIREBIRD-II CubeSats at LEO.
- The lower bounds on the microburst scale size at LEO were 29 ± 1 km (latitudinal) and 51 ± 11 km (longitudinal).
- Deduced lower bound equatorial scale size was similar to the whistler-mode chorus source scale.

1018

Abstract

1019

We present the observation of a spatially large microburst with multiple bounces made simultaneously by the FIREBIRD-II CubeSats on February 2nd, 2015. This is the first observation of a microburst with a subsequent decay made by two co-orbiting but spatially separated spacecraft. From these unique measurements, we place estimates on the lower bounds of the spatial scales as well as quantify the electron bounce periods. The microburst's lower bound latitudinal scale size was 29 ± 1 km and the longitudinal scale size was 51 ± 1 km in low earth orbit. We mapped these scale sizes to the magnetic equator and found that the radial and azimuthal scale sizes were at least 500 ± 10 km and 530 ± 10 km, respectively. These lower bound equatorial scale sizes are similar to whistler-mode chorus wave source scale sizes, which supports the hypothesis that microbursts are a product of electron scattering by chorus waves. Lastly, we estimated the bounce periods for 200-800 keV electrons and found good agreement with four common magnetic field models.

1032

Introduction

1033 The dynamics of radiation belt electrons are complex, and are driven by
 1034 competition between source and loss processes. A few possible loss processes are
 1035 radial diffusion (Shprits and Thorne, 2004), magnetopause shadowing (Ukhorskiy
 1036 et al., 2006), and pitch angle and energy diffusion due to scattering of electrons by
 1037 plasma waves (e.g. Abel and Thorne, 1998; Horne and Thorne, 2003; Meredith et al.,
 1038 2002; Mozer et al., 2018; Selesnick et al., 2003; Summers et al., 1998; Thorne et al.,
 1039 2005). There are a variety of waves that cause pitch angle scattering, including
 1040 electromagnetic ion cyclotron waves, plasmaspheric hiss, and chorus (Millan and
 1041 Thorne, 2007; Thorne, 2010). Chorus predominantly occurs in the dawn sector (6-12
 1042 magnetic local times (MLT)) (Li et al., 2009b) where it accelerates electrons with
 1043 large equatorial pitch angles and scatters electrons with small equatorial pitch angles
 1044 (Horne and Thorne, 2003). Some of these electrons may be impulsively scattered
 1045 into the loss cone, where they result in short-duration (~ 100 ms) enhancements in
 1046 precipitating flux called microbursts.

1047 Anderson and Milton (1964) coined the term microburst to describe high altitude
 1048 balloon observations of ~ 100 ms duration enhancements of bremsstrahlung X-
 1049 rays emitted from scattered microburst electrons impacting the atmosphere. Since
 1050 then, non-relativistic (less than a few hundred keV) microbursts have been routinely
 1051 observed with other balloon missions (e.g. Anderson et al., 2017; Parks, 1967; Woodger
 1052 et al., 2015). A review of the literature shows no reports of microbursts above a few
 1053 hundred keV observed by balloons (Millan et al., 2002; Woodger et al., 2015). This
 1054 lack of observation may be explained by relatively weaker pitch angle scattering of
 1055 relativistic electrons by chorus (Lee et al., 2012).

1056 In addition to the X-ray signature for bursts of electron precipitation, the

1057 precipitating relativistic and non-relativistic electrons have been measured in situ by
 1058 spacecraft orbiting in low earth orbit (LEO). Hereinafter, we refer to these electron
 1059 signatures observed by LEO spacecraft also as microbursts. Microbursts have been
 1060 observed with, e.g. the Solar Anomalous and Magnetospheric Particle Explorer's
 1061 (SAMPEX) \gtrsim 150 keV and \gtrsim 1 MeV channels (Blake et al., 1996; Blum et al., 2015;
 1062 Lorentzen et al., 2001a,b; Nakamura et al., 1995, 2000; O'Brien et al., 2004, 2003) and
 1063 Focused Investigation of Relativistic Electron Bursts: Intensity, Range, and Dynamics
 1064 (FIREBIRD-II) with its \gtrsim 200 keV energy channels (Anderson et al., 2017; Breneman
 1065 et al., 2017; Crew et al., 2016).

1066 Understanding microburst precipitation and its scattering mechanism is impor-
 1067 tant to radiation belt dynamics. The scattering mechanism has been observationally
 1068 studied by e.g. Lorentzen et al. (2001b) who found that microbursts and chorus
 1069 waves predominantly occur in the dawn sector and Breneman et al. (2017) made
 1070 a direct observational link between individual microbursts and chorus elements.
 1071 Microbursts have been modeled and empirically estimated to be capable of depleting
 1072 the relativistic electron population in the outer radiation belt on the order of a day
 1073 (Breneman et al., 2017; O'Brien et al., 2004; Shprits et al., 2007; Thorne et al., 2005).
 1074 An important parameter in this estimation of instantaneous radiation belt electron
 1075 losses due to microbursts is their scale size. Parks (1967) used balloon measurements
 1076 of bremsstrahlung X-rays to estimate the high altitude scale size of predominantly low
 1077 energy microbursts to be 40 ± 14 km. In Blake et al. (1996) a microburst with multiple
 1078 bounces was observed by SAMPEX, and the microburst's latitudinal scale size in LEO
 1079 was estimated to have been "at least a few tens of kilometers". Blake et al. (1996)
 1080 concluded that typically microbursts are less than a few tens of electron gyroradii in
 1081 size (at $L = 5$ at LEO, the gyroradii of 1 MeV electrons is on the order of 100 m).
 1082 Dietrich et al. (2010) used SAMPEX along with ground-based very low frequency

1083 stations to conclude that during one SAMPEX pass, the observed microbursts had
1084 scale sizes less than 4 km.

1085 Since February 1st, 2015, microbursts have been observed by FIREBIRD-II, a
1086 pair of CubeSats in LEO. Soon after launch, when the two FIREBIRD-II spacecraft
1087 were at close range, a microburst with a scale size greater than 11 km was observed
1088 (Crew et al., 2016). On the same day, FIREBIRD-II simultaneously observed a
1089 microburst with multiple bounces. The microburst decay was observed over a period
1090 of a few seconds, while the spacecraft were traveling predominantly in latitude. Here
1091 we present the analysis and results of the latitude and longitude scale sizes and
1092 bounce periods of the first microburst with multiple bounces observed with the two
1093 FIREBIRD-II spacecraft.

1094 Spacecraft and Observation

1095 The FIREBIRD missions are comprised of a pair of identically-instrumented
1096 1.5U CubeSats (15 x 10 x 10 cm) that are designed to measure electron precipitation
1097 in LEO (Klumpar et al., 2015; Spence et al., 2012). The second mission, termed
1098 FIREBIRD-II, was launched on January 31st 2015. The two FIREBIRD-II CubeSats,
1099 identified as Flight Unit 3 (FU3) and Flight Unit 4 (FU4), were placed in a 632 km
1100 apogee, 433 km perigee, and 99° inclination orbit (Crew et al., 2016). FU3 and FU4
1101 are orbiting in a string of pearls configuration with FU4 ahead, to resolve the space-
1102 time ambiguity of microbursts. Each FIREBIRD-II unit has two solid state detectors:
1103 one is mounted essentially at the spacecraft surface, covered only by a thin foil acting
1104 as a sun shade, with a field of view of 90° (surface detector), and the other is beneath
1105 a collimator which restricts the field of view to 54° (collimated detector). Only FU3
1106 has a functioning surface detector, so this analysis utilizes the collimated detectors.
1107 FU3's surface and collimated detectors, as well as FU4's collimated detector observe

1108 electron fluxes in six energy channels from ~ 230 keV to > 1 MeV. FIREBIRD-II's
 1109 High Resolution (HiRes) electron flux data is gathered with an adjustable sampling
 1110 period of 18.75 ms by default and can be as fast as 12.5 ms.

1111 On February 2nd, 2015 at 06:12 UT, both FIREBIRD-II spacecraft simulta-
 1112 neously observed an initial microburst, followed by subsequent periodic electron
 1113 enhancements of diminishing amplitude shown in Fig. 3.1. This is thought to be
 1114 the signature of a single burst of electrons, some of which precipitate, but the rest
 1115 mirror near the spacecraft then bounce to the conjugate hemisphere where they mirror
 1116 again and the subsequent bounces produce a train of decaying peaks (Blake et al.,
 1117 1996; Thorne et al., 2005). This bounce signature occurred during the transition
 1118 between the main and recovery phases of a storm with a minimum Dst of -44 nT
 1119 ($K_p = 4$, and $AE \approx 400$ nT). At this time, the HiRes data was sampled at 18.75 ms.
 1120 Five peaks were observed by both spacecraft. The fifth peak observed by FU4 was
 1121 comparable to the Poisson noise and was not used in this analysis. This microburst
 1122 was observed from the first energy channel ($\approx 200 - 300$ keV), to the fourth energy
 1123 channel ($\approx 500 - 700$ keV), and FU3's surface detector observed the microburst up
 1124 to the fifth energy channel (683 - 950 keV).

1125 The HiRes data in Fig. 3.1 shows signs of energy dispersion, characterized by
 1126 higher energy electrons arriving earlier than the lower energies. This time of flight
 1127 energy dispersion tends to smear out the initial sharp burst upon each subsequent
 1128 bounce. The first peak does not appear to be dispersed, and subsequent peaks show
 1129 a dispersion trend consistent across energy channels. The black vertical bars have
 1130 been added to Fig. 3.1 to highlight this energy dispersion. This dispersion signature
 1131 and amplitude decay implies that the first peak was observed soon after the electrons
 1132 were scattered, followed by decaying bounces.

1133 At this time, in magnetic coordinates, FIREBIRD-II was at McIlwain $L = 4.7$

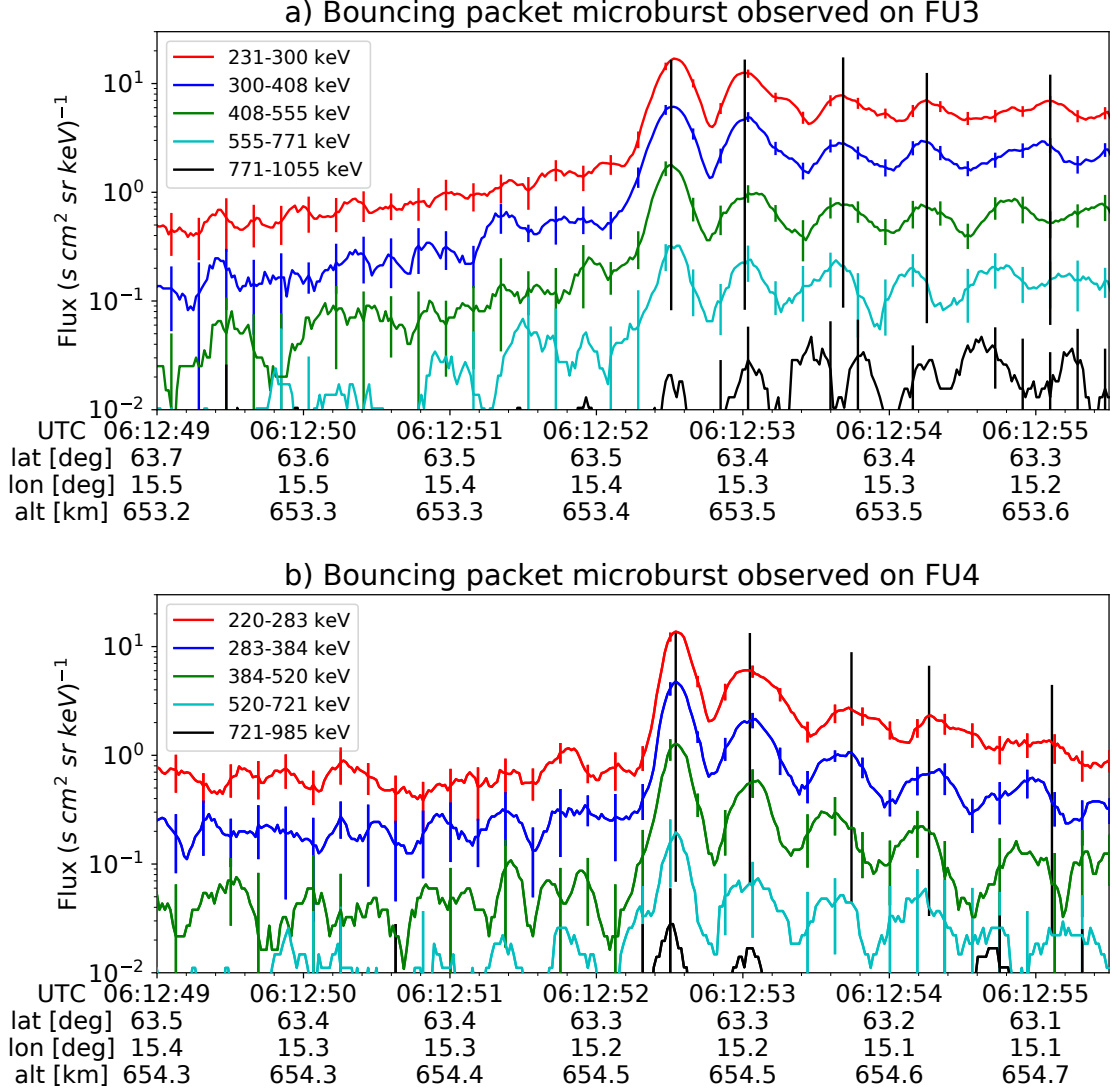


Figure 3.1: HiRes data of the microburst observed at February 2nd, 2015 at 06:12:53 UT, smoothed with a 150 ms rolling average. The subsequent bounces showed some energy dispersion. As discussed in Appendix B, a time correction of -2.28 s was applied to FU3. While the flux from five energy channels is shown, only channels with reasonable counting statistics were used for the spatial scale analysis. Vertical colored bars show the \sqrt{N} error every 10th data point and vertical black bars are lined up with the peaks in the 220-283 keV energy channel to help identify dispersion.

and MLT = 8.3, calculated with the Tsyganenko 1989 (T89) magnetic field model (Tsyganenko, 1989) using IRBEM-Lib (Boscher et al., 2012). Geographically, they were above Sweden, latitude = 63°N, longitude = 15°E, altitude = 650 km. This geographic location is magnetically conjugate to the east of the so-called South Atlantic Anomaly (SAA). The SAA is the location where the mirror points of electrons tend to occur at locations deeper in the atmosphere owing to the offset of the dipole magnetic field from the Earth's center. Electrons with pitch angles within the drift loss cone (DLC) will encounter the SAA and be removed from their eastward longitudinal drift paths (Comess et al., 2013; Dietrich et al., 2010). FU3 and FU4 are therefore both in regions where the particles in the DLC have recently precipitated, leaving only particles that were recently scattered. At the spacecraft location, locally mirroring electrons would have mirrored at 95 km in the opposite hemisphere, with more field aligned electrons mirroring at even lower altitudes. From the analysis done by Fang et al. (2010), the peak in the total ionization rate in the atmosphere for 100 keV electrons is around 80 km altitude, while the total ionization rate from 1 MeV electrons peaks around 60 km altitude. It is, therefore, expected that a fraction of the microburst electrons will survive each encounter with the atmosphere. By plotting the peak flux as a function of bounce (not shown), it was found that 40 - 60 % of the microburst electrons were lost on the first bounce, similar to the 33% loss per bounce observed for a bouncing microburst observed by SAMPEX (Thorne et al., 2005).

1154

Analysis

At the beginning of the FIREBIRD-II mission, two issues prevented the proper analysis of the microburst's spatial scale size: the spacecraft clocks were not synchronized, and their relative positions were not accurately known. We addressed these issues with a cross-correlation time lag analysis described in detail in Appendix

1159 B. From this analysis, the time correction was 2.28 ± 0.12 s (applied to Fig. 3.1) and
 1160 the separation was 19.9 ± 0.9 km at the time of the microburst observation.

1161 Electron Bounce Period

1162 We used this unique observation of bouncing electrons to calculate the bounce
 1163 period, t_b as a function of energy and compare it to the energy-dependent t_b curves
 1164 derived from four magnetic field models, the results of which are shown in Fig. 3.2.
 1165 The observed t_b and uncertainties were calculated by fitting the baseline-subtracted
 1166 HiRes flux. The baseline flux used in this analysis is given in O'Brien et al. (2004)
 1167 as the flux at the 10th percentile over a specified time interval, which in this analysis
 1168 was taken to be 0.5 seconds. The flux was fitted with a superposition of Gaussians
 1169 for each energy channel, and the uncertainty in flux was calculated using the Poisson
 1170 error from the microburst and baseline fluxes summed in quadrature. Using the fit
 1171 parameters, the mean t_b for the lowest four energy channels is shown in Fig. 3.2. The
 1172 trend of decreasing t_b as a function of energy is evident in Fig. 3.2, which further
 1173 supports the assumption that the subsequent peaks are bounces, and not a train of
 1174 microbursts scattered by bouncing chorus.

1175 The decaying peaks in the 231-408 keV electron flux observed by FU3's lowest
 1176 two energy channels (see Fig. 3.1) were right-skewed. One explanation is that there
 1177 was in-channel energy dispersion within those channels. Since t_b of higher energy
 1178 electrons is shorter, a right-skewed peak implies that higher energy electrons were
 1179 more abundant within that channel e.g. in FU3's 231-300 keV channel, the 300 keV
 1180 electrons will arrive sooner than the 231 keV electrons, but will they will be binned
 1181 in the same channel. A Gaussian fit cannot account for this in-channel dispersion,
 1182 and as a first order correction, minima between peaks was used to calculate t_b , and
 1183 is shown in Fig. 3.2. The observed energy-dependent dispersion shown in Fig. 3.2

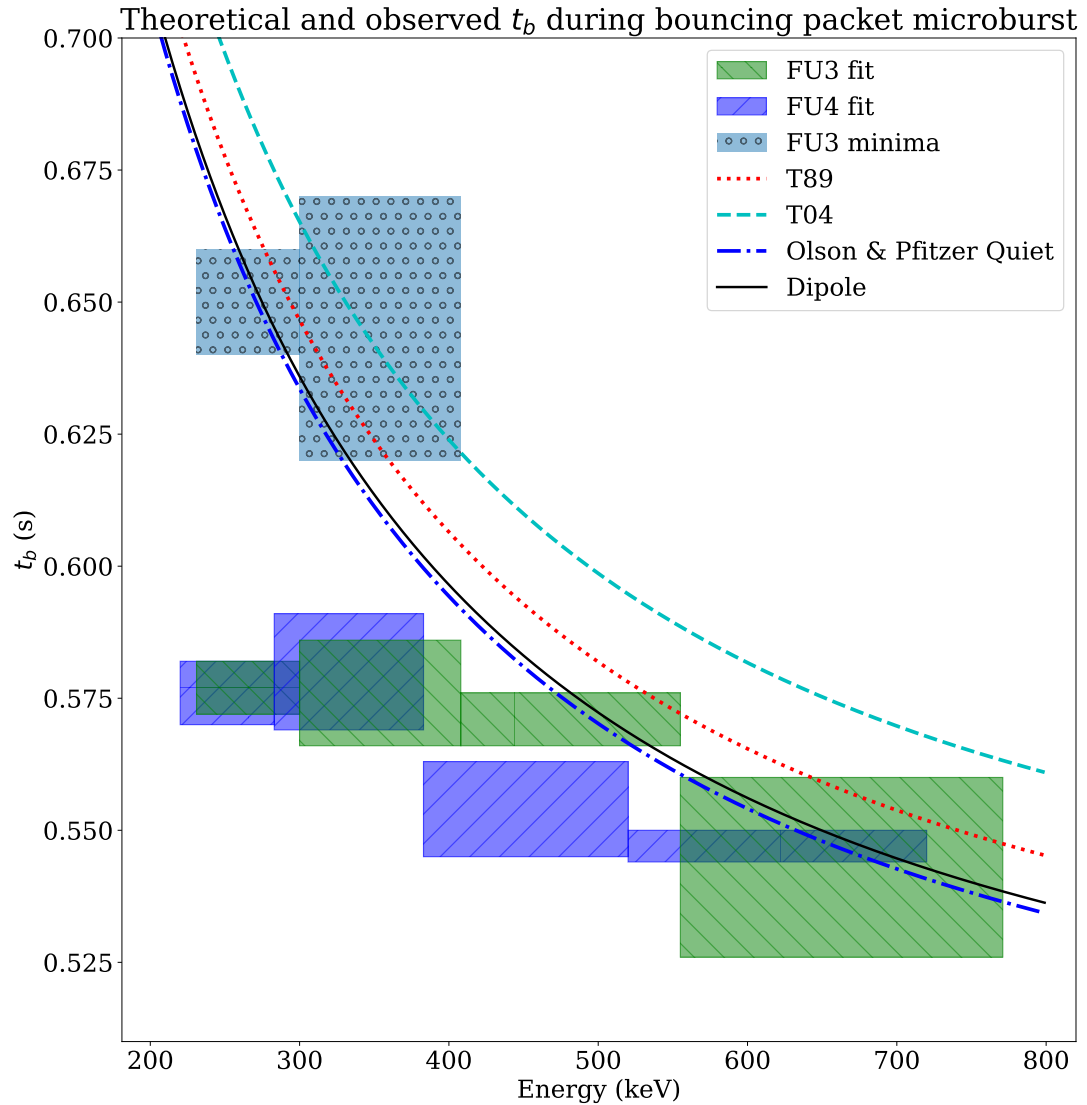


Figure 3.2: Observed and theoretical t_b for electrons of energies from 200 to 770 keV. The solid black line is t_b in a dipole magnetic field, derived in Schulz and Lanzerotti (1974). The red dotted and cyan dashed lines are the t_b derived using the T89, and T04 magnetic field models with IRBEM-Lib. Lastly, the blue dot-dash curve is the t_b derived using the Olson & Pfitzer Quiet model. The green and purple rectangles represent the observed t_b for FU3 and FU4 using a Gaussian fit, respectively. The blue rectangles represent the observed t_b calculated with the minima between the bounces. The width of the boxes represent the width of those energy channels, and the height represents the uncertainty from the fit.

1184 is consistent with higher energy peaks returning sooner. This dispersion consistency
 1185 further supports the assumption that the subsequent peaks are bounces, and not a
 1186 train of microbursts scattered by bouncing chorus.

1187 To compare the observed and modeled t_b , we superposed t_b curves for various
 1188 models including an analytical solution in a dipole (Schulz and Lanzerotti, 1974), and
 1189 numerical models: T89, Tsyganenko 2004 (T04) (Tsyganenko and Sitnov, 2005), and
 1190 Olson & Pfitzer Quiet (Olson and Pfitzer, 1982) in Fig. 3.2. The numerical t_b curves
 1191 were calculated using a wrapper for IRBEM-Lib. This code traces the magnetic field
 1192 line between mirror points, and calculates t_b assuming conservation of energy and the
 1193 first adiabatic invariant for electrons mirroring at FIREBIRD-II. With the empirical
 1194 t_b , the models agree within FIREBIRD-II's uncertainties, but the T04 model has the
 1195 largest discrepancy compared to the other models.

1196 Microburst Energy Spectra

1197 Next, we investigated the energy spectra of this microburst. The energy spectra
 1198 was modeled with an exponential that was fit to the peak flux derived from the
 1199 Gaussian fit parameters in section 3 to all but the highest energy channel. We found
 1200 that the E-folding energy, $E_0 \sim 100$ keV. This spectra is similar to spectra show
 1201 by Lee et al. (2005) from STSAT-1 and Datta et al. (1997) from sounding rocket
 1202 measurements. The energy spectra is soft for a typical microburst observed with
 1203 FIREBIRD-II and there was no statistically significant change in E_0 for subsequent
 1204 bounces.

1205 Microburst Scale Sizes

1206 Lastly, after we applied the time and separation corrections detailed in Appendix
 1207 B, we mapped the locations of FU3 and FU4 in Fig. 3.3. The locations where FU3 saw
 1208 peaks 1-5 and where FU4 saw peaks 1-4 are shown as P1-5 and P1-4, respectively.

1209 The lower bound on the latitudinal extent of the microburst was the difference in
 1210 latitude between P1 on FU3 and P4 on FU4 and was found to be 29 ± 1 km. The
 1211 uncertainty was estimated from the spacecraft separation uncertainty described in
 1212 Appendix B. This scale size is the largest reported by FIREBIRD-II.

1213 In section 3, we showed that the observed decaying peaks were likely due to
 1214 bouncing, so we assume that the observed electrons in subsequent bounces were the
 1215 drifted electrons from the initial microburst. Under this assumption, the scattered
 1216 electrons observed in the last bounce by FIREBIRD-II, must have drifted east from
 1217 their initial scattering longitude, allowing us to calculate the minimum longitudinal
 1218 scale size. Following geometrical arguments, the distance that electrons drift east in
 1219 a single bounce is a product of the circumference of the drift shell foot print, and the
 1220 fraction of the total drift orbit traversed in a single bounce and is given by,

$$d_{az} = 2\pi(R_E + A) \cos(\lambda) \frac{t_b}{\langle T_d \rangle} \quad (3.1)$$

where R_E is the Earth's radius, A is the spacecraft altitude, λ is the magnetic latitude,
 t_b is the electron bounce period, and $\langle T_d \rangle$ is the electron drift period. Parks (2003)
derived $\langle T_d \rangle$ to be,

$$\langle T_d \rangle \approx \begin{cases} 43.8/(L \cdot E) & \text{if } \alpha_0 = 90^\circ \\ 62.7/(L \cdot E) & \text{if } \alpha_0 = 0^\circ \end{cases} \quad (3.2)$$

1221 where E is the electron energy in MeV, L is the L shell, and α_0 is the equatorial pitch
 1222 angle. Electrons mirroring at FIREBIRD-II have $\alpha_0 \approx 3.7^\circ$ and so the $\alpha_0 = 0^\circ$ limit
 1223 was used.

1224 The microburst's longitudinal scale size is defined as the distance the highest
 1225 energy electrons drifted in the time between the observations of the first and last
 1226 peaks. This scale size is given by $D_{az} = n d_{az}$ where n is the number of bounces

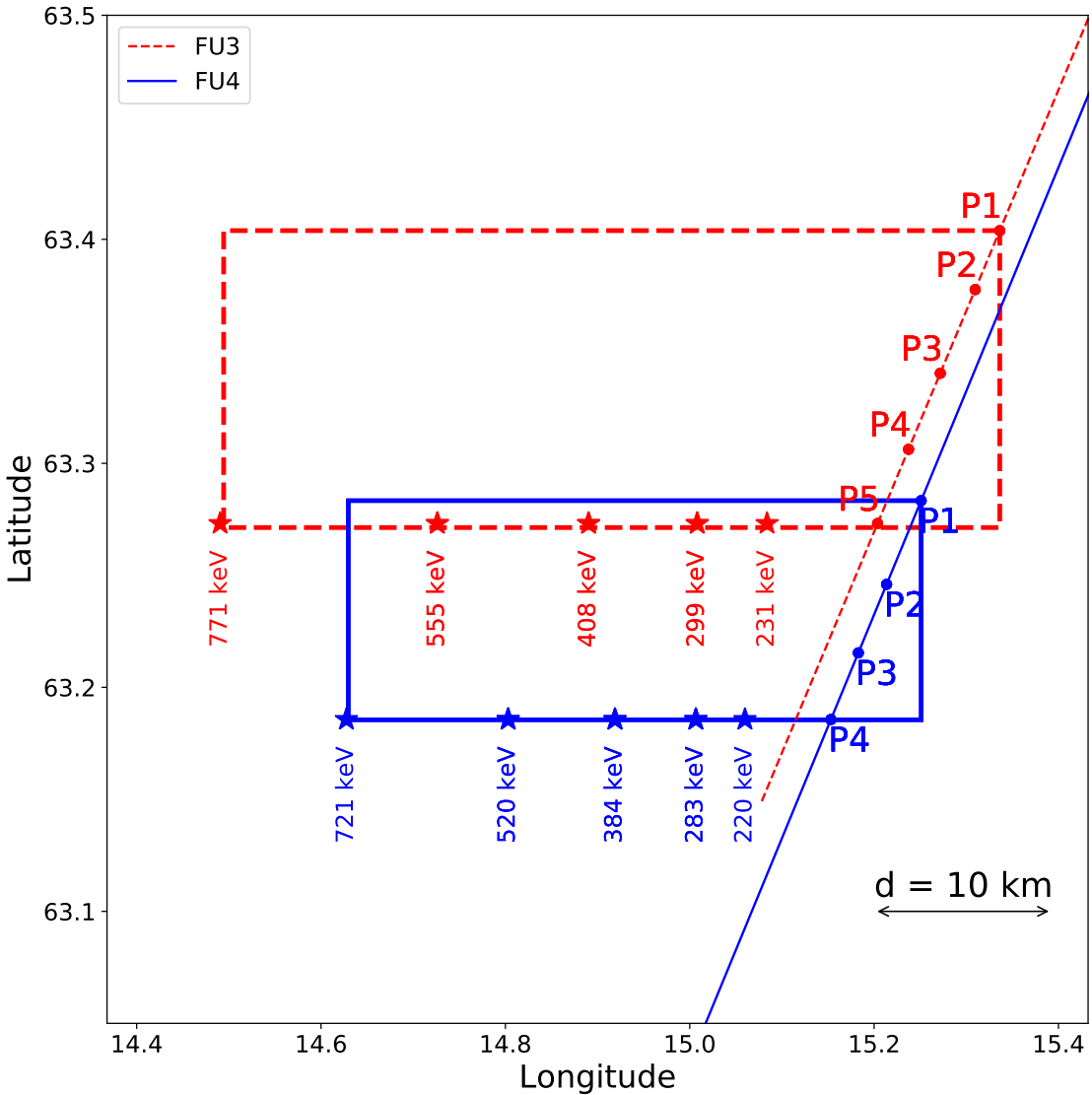


Figure 3.3: The topology of the FIREBIRD-II orbit and the multiple bounces of the microburst projected onto latitude and longitude with axis scaled to equal distance. Attributes relating to FU3 shown in red dashed lines, and FU4 with blue solid lines. The spacecraft path is shown with the diagonal lines, starting at the upper right corner. The labels P1-4 for FU4 and P1-5 for FU3 indicate where the spacecraft were when the N^{th} peak was seen in the lowest energy channel in the HiRes data. The stars with the accompanying energy labels represent the locations of the electrons with that energy that started at time of P1, and were seen at the last peak on each spacecraft. The rectangles represent the lower bound of the microburst scale size, assuming that the majority of the electrons were in the upper boundary of energy channel 4.

1227 observed. The stars in Fig. 3.3 (with labels corresponding to energy channel
 1228 boundaries) represent the locations when the microburst was observed at P1, such
 1229 that an electron of that energy would drift eastward to be seen at P5 for FU3 and P4
 1230 for FU4. Since FU3 observed more peaks it observed the larger longitudinal scale size
 1231 which is shown with the red dashed box in Fig. 3.3. FU3's fourth energy channel's
 1232 bounds are 555 keV and 771 keV, which correspond to longitudinal distances of 39 ± 1
 1233 km and 51 ± 1 , respectively. The uncertainty was estimated by propagating the
 1234 uncertainty in the bounce time Eq. 3.1. While the observed minimum longitudinal
 1235 scale size is dependent on FIREBIRD-II's energy channels, the true scale size may
 1236 not be.

1237 To investigate how the microburst scale size compares to the scale sizes of chorus
 1238 waves near the magnetic equator, the microburst's longitudinal and latitudinal scale
 1239 sizes and their uncertainties in LEO were mapped to the magnetic equator with T89.
 1240 The radial scale size (latitudinal scale mapped from LEO) was greater than 500 ± 10
 1241 km. The azimuthal scale size (longitudinal scale mapped from LEO) of 555 keV
 1242 electrons was greater than 450 ± 10 km and for the 771 keV electrons it was greater
 1243 than 530 ± 10 km. The lower bound microburst scale size is similar to the chorus
 1244 scale sizes derived by Agapitov et al. (2017, 2011), and is discussed below.

1245

Discussion and Conclusions

1246 We presented the first observation of a large microburst with multiple bounces
 1247 made possible by the twin FIREBIRD-II CubeSats. The microburst's lower bound
 1248 LEO latitudinal and longitudinal scale sizes of 29 ± 1 km and 51 ± 1 km make
 1249 it one of the largest observed. The microburst's LEO scale size was larger than
 1250 the latitudinal scale sizes of typical > 1 MeV microbursts reported in Blake et al.
 1251 (1996), approximately 10 times larger than reported in Dietrich et al. (2010), and

1252 approximately 2.6 times larger than other simultaneous microbursts observed by
 1253 FIREBIRD-II (Crew et al., 2016). Lastly, the scale sizes derived here were similar to
 1254 the scale sizes of \sim 15 keV microbursts observed with a high altitude balloon (Parks,
 1255 1967). No energy dependence on the minimum latitudinal scale size was observed,
 1256 while the observed energy dependence of the minimum longitudinal scale size is an
 1257 artifact of the technique we used to estimate their drift motion.

1258 The microburst scale size obtained in Section 3 and scaled to the geomagnetic
 1259 equator can be compared with the scales of chorus waves presumably responsible for
 1260 the rapid burst electron precipitation. Early direct estimates of the chorus source
 1261 scales were made by the coordinated measurement by ISEE-1, 2. The wave power
 1262 correlation scale was estimated to be about several hundred kilometers across the
 1263 background magnetic field (Gurnett et al., 1979). Furthermore, Santolik et al. (2003)
 1264 determined the correlation lengths of chorus-type whistler waves to be around 100
 1265 km based on multipoint CLUSTER Wide Band Data measurements near the chorus
 1266 source region at $L \approx 4$, during the magnetic storm of 18 April 2002. Agapitov et al.
 1267 (2017, 2011, 2010) recently showed that the spatial extent of chorus source region can
 1268 be larger, ranging from 600 km in the outer radiation belt to more than 1000 km in
 1269 the outer magnetosphere. The lower bound azimuthal and latitudinal scales obtained
 1270 in Section 3 and scaled to the magnetic equator, are similar to the whistler-mode
 1271 chorus source scale sizes reported in Agapitov et al. (2017, 2011).

1272 No wave measurements from nearby spacecraft were available at this time.
 1273 Nevertheless, during the hours before and after this observation, the Van Allen Probes'
 1274 (Mauk et al., 2013) Electric and Magnetic Field Instrument and Integrated Science
 1275 (Kletzing et al., 2013) observed strong wave power in the lower band chorus frequency
 1276 range, inside the outer radiation belt between 22 and 2 MLT. Furthermore, AE ~ 400
 1277 nT at this time, and relatively strong chorus waves were statistically more likely to

1278 be present at FIREBIRD-II's MLT (Li et al., 2009b).

1279 The empirically estimated and modeled t_b in this study agree within FIREBIRD-
 1280 II's uncertainties, confirming that the energy-dependent dispersion was due to
 1281 bouncing. The t_b curves are a proxy for field line length, and this agreement implies
 1282 that they are comparable. This is expected since the magnetosphere is not drastically
 1283 compressed at 8 MLT, but we expect a larger discrepancy near midnight, where the
 1284 magnetosphere is more stretched and difficult to accurately model. In future studies,
 1285 this analysis can be used as a diagnostic tool to validate field line lengths, and improve
 1286 magnetic field models.

1287 The similarity of the microburst and chorus source region scale sizes, as well
 1288 as magnetospheric location and conditions, further support the causal relationship
 1289 between microbursts and chorus.

1290

Acknowledgments

1291 This work was made possible with help from the FIREBIRD team, and the
 1292 members of the Space Sciences and Engineering Laboratory at Montana State
 1293 University for their hard work to make this mission a success. In addition, M.
 1294 Shumko acknowledges Drew Turner for his suggestions regarding the bounce period
 1295 calculations, and Dana Longcope for his proofreading feedback. The FIREBIRD-II
 1296 data are available at http://solar.physics.montana.edu/FIREBIRD_II/. This analysis
 1297 is supported by the National Science Foundation under Grant Numbers 0838034 and
 1298 1339414. Furthermore, the work of O. Agapitov was supported by the NASA grant
 1299 NNX16AF85G.

1300

CONCLUSION

1301 L^AT_EX produces documents that look great, automatically handles references and
1302 citations, and easily incorporates figures and tables. This is not a guide to L^AT_EX but
1303 rather an introduction to the MSU style. If you want more information about L^AT_EX
1304 many introductory guides can be found online.

- 1306 Abel, B. and Thorne, R. M. (1998). Electron scattering loss in earth's inner
1307 magnetosphere: 1. dominant physical processes. *Journal of Geophysical Research: Space Physics*, 103(A2):2385–2396.
- 1309 Agapitov, O., Blum, L. W., Mozer, F. S., Bonnell, J. W., and Wygant, J. (2017).
1310 Chorus whistler wave source scales as determined from multipoint van allen probe
1311 measurements. *Geophysical Research Letters*, pages n/a–n/a. 2017GL072701.
- 1312 Agapitov, O., Krasnoselskikh, V., Dudok de Wit, T., Khotyaintsev, Y., Pickett,
1313 J. S., Santolik, O., and Rolland, G. (2011). Multispacecraft observations of chorus
1314 emissions as a tool for the plasma density fluctuations' remote sensing. *Journal of Geophysical Research: Space Physics*, 116(A9):n/a–n/a. A09222.
- 1316 Agapitov, O., Krasnoselskikh, V., Zaliznyak, Y., Angelopoulos, V., Le Contel, O.,
1317 and Rolland, G. (2010). Chorus source region localization in the earth's outer
1318 magnetosphere using themis measurements. *Annales Geophysicae*, 28(6):1377–
1319 1386.
- 1320 Anderson, B., Shekhar, S., Millan, R., Crew, A., Spence, H., Klumpar, D., Blake, J.,
1321 O'Brien, T., and Turner, D. (2017). Spatial scale and duration of one microburst
1322 region on 13 August 2015. *Journal of Geophysical Research: Space Physics*.
- 1323 Anderson, K. A. and Milton, D. W. (1964). Balloon observations of X rays in the
1324 auroral zone: 3. High time resolution studies. *Journal of Geophysical Research*,
1325 69(21):4457–4479.
- 1326 Barcus, J., Brown, R., and Rosenberg, T. (1966). Spatial and temporal character of
1327 fast variations in auroral-zone x rays. *Journal of Geophysical Research*, 71(1):125–
1328 141.
- 1329 Baumjohann, W. and Treumann, R. A. (1997). *Basic space plasma physics*. World
1330 Scientific.
- 1331 Blake, J., Carranza, P., Claudepierre, S., Clemons, J., Crain, W., Dotan, Y.,
1332 Fennell, J., Fuentes, F., Galvan, R., George, J., et al. (2013). The magnetic electron
1333 ion spectrometer (MagEIS) instruments aboard the radiation belt storm probes
1334 (RBSP) spacecraft. *Space Science Reviews*, 179(1-4):383–421.
- 1335 Blake, J.,Looper, M., Baker, D., Nakamura, R., Klecker, B., and Hovestadt, D.
1336 (1996). New high temporal and spatial resolution measurements by sampex of the
1337 precipitation of relativistic electrons. *Advances in Space Research*, 18(8):171 – 186.
- 1338 Blake, J. B. and O'Brien, T. P. (2016). Observations of small-scale latitudinal
1339 structure in energetic electron precipitation. *Journal of Geophysical Research: Space Physics*, 121(4):3031–3035. 2015JA021815.

- 1341 Blum, L., Li, X., and Denton, M. (2015). Rapid MeV electron precipitation as
 1342 observed by SAMPEX/HILT during high-speed stream-driven storms. *Journal of*
 1343 *Geophysical Research: Space Physics*, 120(5):3783–3794. 2014JA020633.
- 1344 Bortnik, J., Thorne, R., and Inan, U. S. (2008). Nonlinear interaction of energetic
 1345 electrons with large amplitude chorus. *Geophysical Research Letters*, 35(21).
- 1346 Boscher, D., Bourdarie, S., O'Brien, P., Guild, T., and Shumko, M. (2012). Irbem-lib
 1347 library.
- 1348 Breneman, A., Crew, A., Sample, J., Klumpar, D., Johnson, A., Agapitov, O.,
 1349 Shumko, M., Turner, D., Santolik, O., Wygant, J., et al. (2017). Observations
 1350 directly linking relativistic electron microbursts to whistler mode chorus: Van allen
 1351 probes and FIREBIRD II. *Geophysical Research Letters*.
- 1352 Breneman, A. W., Halford, A., Millan, R., McCarthy, M., Fennell, J., Sample, J.,
 1353 Woodger, L., Hospodarsky, G., Wygant, J. R., Cattell, C. A., et al. (2015). Global-
 1354 scale coherence modulation of radiation-belt electron loss from plasmaspheric hiss.
 1355 *Nature*, 523(7559):193.
- 1356 Brown, R., Barcus, J., and Parsons, N. (1965). Balloon observations of auroral zone
 1357 x rays in conjugate regions. 2. microbursts and pulsations. *Journal of Geophysical*
 1358 *Research (U.S.)*.
- 1359 Capannolo, L., Li, W., Ma, Q., Shen, X.-C., Zhang, X.-J., Redmon, R., Rodriguez,
 1360 J., Engebretson, M., Kletzing, C., Kurth, W., et al. (2019). Energetic electron
 1361 precipitation: multi-event analysis of its spatial extent during emic wave activity.
 1362 *Journal of Geophysical Research: Space Physics*.
- 1363 Claudepierre, S., O'Brien, T.,Looper, M., Blake, J., Fennell, J., Roeder, J.,
 1364 Clemons, J., Mazur, J., Turner, D., Reeves, G., et al. (2019). A revised look
 1365 at relativistic electrons in the earth's inner radiation zone and slot region. *Journal*
 1366 *of Geophysical Research: Space Physics*, 124(2):934–951.
- 1367 Comess, M., Smith, D., Selesnick, R., Millan, R., and Sample, J. (2013). Duskside
 1368 relativistic electron precipitation as measured by sampex: A statistical survey.
 1369 *Journal of Geophysical Research: Space Physics*, 118(8):5050–5058.
- 1370 Crew, A. B., Spence, H. E., Blake, J. B., Klumpar, D. M., Larsen, B. A., O'Brien,
 1371 T. P., Driscoll, S., Handley, M., Legere, J., Longworth, S., Mashburn, K.,
 1372 Mosleh, E., Ryhajlo, N., Smith, S., Springer, L., and Widholm, M. (2016). First
 1373 multipoint in situ observations of electron microbursts: Initial results from the
 1374 NSF FIREBIRD II mission. *Journal of Geophysical Research: Space Physics*,
 1375 121(6):5272–5283. 2016JA022485.

- 1376 Datta, S., Skoug, R., McCarthy, M., and Parks, G. (1997). Modeling of microburst
 1377 electron precipitation using pitch angle diffusion theory. *Journal of Geophysical*
 1378 *Research: Space Physics*, 102(A8):17325–17333.
- 1379 Dietrich, S., Rodger, C. J., Clilverd, M. A., Bortnik, J., and Raita, T. (2010).
 1380 Relativistic microburst storm characteristics: Combined satellite and ground-based
 1381 observations. *Journal of Geophysical Research: Space Physics*, 115(A12).
- 1382 Douma, E., Rodger, C. J., Blum, L. W., and Clilverd, M. A. (2017). Occurrence
 1383 characteristics of relativistic electron microbursts from SAMPEX observations.
 1384 *Journal of Geophysical Research: Space Physics*, 122(8):8096–8107. 2017JA024067.
- 1385 Dungey, J. W. (1961). Interplanetary magnetic field and the auroral zones. *Phys.*
 1386 *Rev. Lett.*, 6:47–48.
- 1387 Fang, X., Randall, C. E., Lummerzheim, D., Wang, W., Lu, G., Solomon, S. C., and
 1388 Frahm, R. A. (2010). Parameterization of monoenergetic electron impact ionization.
 1389 *Geophysical Research Letters*, 37(22).
- 1390 Funsten, H., Skoug, R., Guthrie, A., MacDonald, E., Baldonado, J., Harper, R.,
 1391 Henderson, K., Kihara, K., Lake, J., Larsen, B., et al. (2013). Helium, Oxygen,
 1392 Proton, and Electron (HOPE) mass spectrometer for the radiation belt storm
 1393 probes mission. *Space Science Reviews*, 179(1-4):423–484.
- 1394 Greeley, A., Kanekal, S., Baker, D., Klecker, B., and Schiller, Q. (2019). Quantifying
 1395 the contribution of microbursts to global electron loss in the radiation belts. *Journal*
 1396 *of Geophysical Research: Space Physics*.
- 1397 Gurnett, D., Anderson, R., Scarf, F., Fredricks, R., and Smith, E. (1979). Initial
 1398 results from the isee-1 and-2 plasma wave investigation. *Space Science Reviews*,
 1399 23(1):103–122.
- 1400 Hendry, A. T., Rodger, C. J., and Clilverd, M. A. (2017). Evidence of sub-mev
 1401 emic-driven electron precipitation. *Geophysical Research Letters*, 44(3):1210–1218.
- 1402 Hoots, F. R. and Roehrich, R. L. (1980). Models for propagation of norad element
 1403 sets. Technical Report 3, Spacetrack.
- 1404 Horne, R., Glauert, S., Meredith, N., Boscher, D., Maget, V., Heynderickx, D., and
 1405 Pitchford, D. (2013). Space weather impacts on satellites and forecasting the earth's
 1406 electron radiation belts with spacecast. *Space Weather*, 11(4):169–186.
- 1407 Horne, R., Thorne, R., Meredith, N., and Anderson, R. (2003). Diffuse auroral
 1408 electron scattering by electron cyclotron harmonic and whistler mode waves during
 1409 an isolated substorm. *Journal of Geophysical Research: Space Physics*, 108(A7).

- 1410 Horne, R. B. and Thorne, R. M. (2003). Relativistic electron acceleration and
 1411 precipitation during resonant interactions with whistler-mode chorus. *Geophysical*
 1412 *Research Letters*, 30(10). 1527.
- 1413 Horne, R. B., Thorne, R. M., Shprits, Y. Y., Meredith, N. P., Glauert, S. A., Smith,
 1414 A. J., Kanekal, S. G., Baker, D. N., Engebretson, M. J., Posch, J. L., et al.
 1415 (2005). Wave acceleration of electrons in the van allen radiation belts. *Nature*,
 1416 437(7056):227.
- 1417 Kasahara, S., Miyoshi, Y., Yokota, S., Mitani, T., Kasahara, Y., Matsuda, S.,
 1418 Kumamoto, A., Matsuoka, A., Kazama, Y., Frey, H., et al. (2018). Pulsating
 1419 aurora from electron scattering by chorus waves. *Nature*, 554(7692):337.
- 1420 Kletzing, C., Kurth, W., Acuna, M., MacDowall, R., Torbert, R., Averkamp, T.,
 1421 Bodet, D., Bounds, S., Chutter, M., Connerney, J., et al. (2013). The electric and
 1422 magnetic field instrument suite and integrated science (EMFISIS) on RBSP. *Space*
 1423 *Science Reviews*, 179(1-4):127–181.
- 1424 Klumpar, D., Springer, L., Mosleh, E., Mashburn, K., Berardinelli, S., Gunderson,
 1425 A., Handly, M., Ryhajlo, N., Spence, H., Smith, S., Legere, J., Widholm, M.,
 1426 Longworth, S., Crew, A., Larsen, B., Blake, J., and Walmsley, N. (2015). Flight
 1427 system technologies enabling the twin-cubesat firebird-ii scientific mission.
- 1428 Lee, J. J., Parks, G. K., Lee, E., Tsurutani, B. T., Hwang, J., Cho, K. S., Kim, K.-H.,
 1429 Park, Y. D., Min, K. W., and McCarthy, M. P. (2012). Anisotropic pitch angle
 1430 distribution of 100 keV microburst electrons in the loss cone: measurements from
 1431 STSAT-1. *Annales Geophysicae*, 30(11):1567–1573.
- 1432 Lee, J.-J., Parks, G. K., Min, K. W., Kim, H. J., Park, J., Hwang, J., McCarthy,
 1433 M. P., Lee, E., Ryu, K. S., Lim, J. T., Sim, E. S., Lee, H. W., Kang, K. I., and
 1434 Park, H. Y. (2005). Energy spectra of 170–360 keV electron microbursts measured
 1435 by the korean STSAT-1. *Geophysical Research Letters*, 32(13). L13106.
- 1436 Li, W., Thorne, R., Angelopoulos, V., Bonnell, J., McFadden, J., Carlson, C.,
 1437 LeContel, O., Roux, A., Glassmeier, K., and Auster, H. (2009a). Evaluation of
 1438 whistler-mode chorus intensification on the nightside during an injection event
 1439 observed on the THEMIS spacecraft. *Journal of Geophysical Research: Space*
 1440 *Physics*, 114(A1).
- 1441 Li, W., Thorne, R., Bortnik, J., Tao, X., and Angelopoulos, V. (2012). Characteristics
 1442 of hiss-like and discrete whistler-mode emissions. *Geophysical Research Letters*,
 1443 39(18).
- 1444 Li, W., Thorne, R. M., Angelopoulos, V., Bortnik, J., Cully, C. M., Ni, B., LeContel,
 1445 O., Roux, A., Auster, U., and Magnes, W. (2009b). Global distribution of whistler-
 1446 mode chorus waves observed on the THEMIS spacecraft. *Geophysical Research*
 1447 *Letters*, 36(9). L09104.

- 1448 Li, X., Selesnick, R., Schiller, Q., Zhang, K., Zhao, H., Baker, D. N., and Temerin,
 1449 M. A. (2017). Measurement of electrons from albedo neutron decay and neutron
 1450 density in near-earth space. *Nature*, 552(7685):382.
- 1451 Lorentzen, K. R., Blake, J. B., Inan, U. S., and Bortnik, J. (2001a). Observations
 1452 of relativistic electron microbursts in association with VLF chorus. *Journal of*
 1453 *Geophysical Research: Space Physics*, 106(A4):6017–6027.
- 1454 Lorentzen, K. R.,Looper, M. D., and Blake, J. B. (2001b). Relativistic electron
 1455 microbursts during the GEM storms. *Geophysical Research Letters*, 28(13):2573–
 1456 2576.
- 1457 Lyons, L. R. and Thorne, R. M. (1973). Equilibrium structure of radiation belt
 1458 electrons. *Journal of Geophysical Research*, 78(13):2142–2149.
- 1459 Manweiler, J. W. and Zwiener, H. M. (2018). Science Operations Center (SOC)
 1460 RBSPICE Science Data Handbook Revision: e. Technical report, Fundamental
 1461 Technologies, LLC.
- 1462 Mauk, B., Fox, N. J., Kanekal, S., Kessel, R., Sibeck, D., and Ukhorskiy, A. (2013).
 1463 Science objectives and rationale for the radiation belt storm probes mission. *Space*
 1464 *Science Reviews*, 179(1-4):3–27.
- 1465 Meredith, N., Horne, R., Summers, D., Thorne, R., Iles, R., Heynderickx, D., and
 1466 Anderson, R. (2002). Evidence for acceleration of outer zone electrons to relativistic
 1467 energies by whistler mode chorus. In *Annales Geophysicae*, volume 20, pages 967–
 1468 979.
- 1469 Millan, R. and Thorne, R. (2007). Review of radiation belt relativistic electron losses.
 1470 *Journal of Atmospheric and Solar-Terrestrial Physics*, 69(3):362 – 377.
- 1471 Millan, R. M., Lin, R., Smith, D., Lorentzen, K., and McCarthy, M. (2002). X-
 1472 ray observations of mev electron precipitation with a balloon-borne germanium
 1473 spectrometer. *Geophysical research letters*, 29(24).
- 1474 Mitchell, D., Lanzerotti, L., Kim, C., Stokes, M., Ho, G., Cooper, S., Ukhorskiy, A.,
 1475 Manweiler, J., Jaskulek, S., Haggerty, D., et al. (2013). Radiation belt storm probes
 1476 ion composition experiment (RBSPICE). *Space Science Reviews*, 179(1-4):263–308.
- 1477 Mozer, F. S., Agapitov, O. V., Blake, J. B., and Vasko, I. Y. (2018). Simultaneous
 1478 observations of lower band chorus emissions at the equator and microburst
 1479 precipitating electrons in the ionosphere. *Geophysical Research Letters*.
- 1480 Nakamura, R., Baker, D. N., Blake, J. B., Kanekal, S., Klecker, B., and Hovestadt,
 1481 D. (1995). Relativistic electron precipitation enhancements near the outer edge of
 1482 the radiation belt. *Geophysical Research Letters*, 22(9):1129–1132.

- 1483 Nakamura, R., Isowa, M., Kamide, Y., Baker, D., Blake, J., and Looper, M. (2000).
 1484 Observations of relativistic electron microbursts in association with VLF chorus.
 1485 *J. Geophys. Res.*, 105:15875–15885.
- 1486 Nishimura, Y., Bortnik, J., Li, W., Thorne, R., Chen, L., Lyons, L., Angelopoulos,
 1487 V., Mende, S., Bonnell, J., Le Contel, O., et al. (2011). Multievent study of the
 1488 correlation between pulsating aurora and whistler mode chorus emissions. *Journal*
 1489 *of Geophysical Research: Space Physics*, 116(A11).
- 1490 O'Brien, T., Claudepierre, S., Blake, J., Fennell, J. F., Clemons, J., Roeder, J.,
 1491 Spence, H. E., Reeves, G., and Baker, D. (2014). An empirically observed pitch-
 1492 angle diffusion eigenmode in the earth's electron belt near $l^*= 5.0$. *Geophysical*
 1493 *Research Letters*, 41(2):251–258.
- 1494 O'Brien, T., Claudepierre, S., Guild, T., Fennell, J., Turner, D., Blake, J., Clemons,
 1495 J., and Roeder, J. (2016). Inner zone and slot electron radial diffusion revisited.
 1496 *Geophysical Research Letters*, 43(14):7301–7310.
- 1497 O'Brien, T. and Moldwin, M. (2003). Empirical plasmapause models from magnetic
 1498 indices. *Geophysical Research Letters*, 30(4).
- 1499 O'Brien, T. P., Looper, M. D., and Blake, J. B. (2004). Quantification of relativistic
 1500 electron microburst losses during the GEM storms. *Geophysical Research Letters*,
 1501 31(4). L04802.
- 1502 O'Brien, T. P., Lorentzen, K. R., Mann, I. R., Meredith, N. P., Blake, J. B., Fennell,
 1503 J. F., Looper, M. D., Milling, D. K., and Anderson, R. R. (2003). Energization of
 1504 relativistic electrons in the presence of ULF power and MeV microbursts: Evidence
 1505 for dual ULF and VLF acceleration. *Journal of Geophysical Research: Space*
 1506 *Physics*, 108(A8).
- 1507 Olson, W. P. and Pfitzer, K. A. (1982). A dynamic model of the magnetospheric
 1508 magnetic and electric fields for july 29, 1977. *Journal of Geophysical Research:*
 1509 *Space Physics*, 87(A8):5943–5948.
- 1510 Ozaki, M., Miyoshi, Y., Shiokawa, K., Hosokawa, K., Oyama, S.-i., Kataoka, R.,
 1511 Ebihara, Y., Ogawa, Y., Kasahara, Y., Yagitani, S., et al. (2019). Visualization of
 1512 rapid electron precipitation via chorus element wave-particle interactions. *Nature*
 1513 *communications*, 10(1):257.
- 1514 Ozaki, M., Yagitani, S., Ishizaka, K., Shiokawa, K., Miyoshi, Y., Kadokura, A.,
 1515 Yamagishi, H., Kataoka, R., Ieda, A., Ebihara, Y., Sato, N., and Nagano, I. (2012).
 1516 Observed correlation between pulsating aurora and chorus waves at Syowa Station
 1517 in Antarctica: A case study. *Journal of Geophysical Research: Space Physics*,
 1518 117(A8).

- 1519 Parks, G. (2003). *Physics Of Space Plasmas: An Introduction, Second Edition.*
 1520 Westview Press.
- 1521 Parks, G. K. (1967). Spatial characteristics of auroral-zone X-ray microbursts. *Journal
 1522 of Geophysical Research*, 72(1):215–226.
- 1523 Reeves, G., Spence, H. E., Henderson, M., Morley, S., Friedel, R., Funsten, H., Baker,
 1524 D., Kanekal, S., Blake, J., Fennell, J., et al. (2013). Electron acceleration in the
 1525 heart of the van allen radiation belts. *Science*, 341(6149):991–994.
- 1526 Reeves, G. D., McAdams, K. L., Friedel, R. H. W., and O'Brien, T. P. (2003). Ac-
 1527 celeration and loss of relativistic electrons during geomagnetic storms. *Geophysical
 1528 Research Letters*, 30(10):n/a–n/a. 1529.
- 1529 Santolik, O., Gurnett, D., Pickett, J., Parrot, M., and Cornilleau-Wehrlin, N. (2003).
 1530 Spatio-temporal structure of storm-time chorus. *Journal of Geophysical Research:
 1531 Space Physics*, 108(A7).
- 1532 Santolk, O., Parrot, M., and Lefevre, F. (2003). Singular value decomposition
 1533 methods for wave propagation analysis. *Radio Science*, 38(1):n/a–n/a. 1010.
- 1534 Schulz, M. and Lanzerotti, L. J. (1974). *Particle Diffusion in the Radiation Belts.*
 1535 Springer.
- 1536 Selesnick, R. S., Blake, J. B., and Mewaldt, R. A. (2003). Atmospheric losses of
 1537 radiation belt electrons. *Journal of Geophysical Research: Space Physics*, 108(A12).
 1538 1468.
- 1539 Shprits, Y. Y., Meredith, N. P., and Thorne, R. M. (2007). Parameterization
 1540 of radiation belt electron loss timescales due to interactions with chorus waves.
 1541 *Geophysical Research Letters*, 34(11):n/a–n/a. L11110.
- 1542 Shprits, Y. Y. and Thorne, R. M. (2004). Time dependent radial diffusion modeling
 1543 of relativistic electrons with realistic loss rates. *Geophysical Research Letters*,
 1544 31(8):n/a–n/a. L08805.
- 1545 Spence, H. E., Blake, J. B., Crew, A. B., Driscoll, S., Klumpar, D. M., Larsen,
 1546 B. A., Legere, J., Longworth, S., Mosleh, E., O'Brien, T. P., Smith, S., Springer,
 1547 L., and Widholm, M. (2012). Focusing on size and energy dependence of electron
 1548 microbursts from the van allen radiation belts. *Space Weather*, 10(11).
- 1549 Summers, D., Thorne, R. M., and Xiao, F. (1998). Relativistic theory of wave-particle
 1550 resonant diffusion with application to electron acceleration in the magnetosphere.
 1551 *Journal of Geophysical Research: Space Physics*, 103(A9):20487–20500.

- 1552 Takahashi, K. and Denton, R. E. (2007). Magnetospheric seismology using multi-
 1553 harmonic toroidal waves observed at geosynchronous orbit. *Journal of Geophysical*
 1554 *Research: Space Physics*, 112(A5).
- 1555 Thorne, R. M. (2010). Radiation belt dynamics: The importance of wave-particle
 1556 interactions. *Geophysical Research Letters*, 37(22). L22107.
- 1557 Thorne, R. M. and Andreoli, L. J. (1981). *Mechanisms for Intense Relativistic*
 1558 *Electron Precipitation*, pages 381–394. Springer Netherlands, Dordrecht.
- 1559 Thorne, R. M., O'Brien, T. P., Shprits, Y. Y., Summers, D., and Horne, R. B. (2005).
 1560 Timescale for MeV electron microburst loss during geomagnetic storms. *Journal*
 1561 *of Geophysical Research: Space Physics*, 110(A9). A09202.
- 1562 Trefall, H., Bjordal, J., Ullaland, S., and Stadsnes, J. (1966). On the extension of
 1563 auroral-zone x-ray microbursts. *Journal of Atmospheric and Terrestrial Physics*,
 1564 28(2):225–233.
- 1565 Tsurutani, B. T. and Lakhina, G. S. (1997). Some basic concepts of wave-particle
 1566 interactions in collisionless plasmas. *Reviews of Geophysics*, 35(4):491–501.
- 1567 Tsyganenko, N. (1989). A solution of the chapman-ferraro problem for an ellipsoidal
 1568 magnetopause. *Planetary and Space Science*, 37(9):1037 – 1046.
- 1569 Tsyganenko, N. A. and Sitnov, M. I. (2005). Modeling the dynamics of the inner
 1570 magnetosphere during strong geomagnetic storms. *Journal of Geophysical Research:*
 1571 *Space Physics*, 110(A3).
- 1572 Turner, D., Claudepierre, S., Fennell, J., O'Brien, T., Blake, J., Lemon, C.,
 1573 Gkioulidou, M., Takahashi, K., Reeves, G., Thaller, S., et al. (2015). Energetic
 1574 electron injections deep into the inner magnetosphere associated with substorm
 1575 activity. *Geophysical Research Letters*, 42(7):2079–2087.
- 1576 Ukhorskiy, A. Y., Anderson, B. J., Brandt, P. C., and Tsyganenko, N. A. (2006).
 1577 Storm time evolution of the outer radiation belt: Transport and losses. *Journal of*
 1578 *Geophysical Research: Space Physics*, 111(A11):n/a–n/a. A11S03.
- 1579 Van Allen, J. A. (1959). The geomagnetically trapped corpuscular radiation. *Journal*
 1580 *of Geophysical Research*, 64(11):1683–1689.
- 1581 Vernov, S. and Chudakov, A. (1960). Investigation of radiation in outer space. In
 1582 *International Cosmic Ray Conference*, volume 3, page 19.
- 1583 Walker, A. D. M. (1993). *Plasma waves in the magnetosphere*, volume 24. Springer
 1584 Science & Business Media.

- 1585 Woodger, L., Halford, A., Millan, R., McCarthy, M., Smith, D., Bowers, G., Sample,
1586 J., Anderson, B., and Liang, X. (2015). A summary of the BARREL campaigns:
1587 Technique for studying electron precipitation. *Journal of Geophysical Research: Space Physics*, 120(6):4922–4935.
1588

APPENDIX: APPENDIX A

1590 This appendix contains Figs. A.1 and A.2. Figure A.1 shows evidence that
1591 supports our claim that the “hiss-like” chorus wave observed at 11:17:03 UT with
1592 EMFISIS WFR instrument on RBSP-A was parallel propagating. The polar angle
1593 of the wave vector and the supporting planarity of the magnetic field polarization
1594 shown in Fig. A.1 was calculated using the singular value decomposition (SVD)
1595 method (Santolk et al., 2003).

1596 Figure A.2 supports the claim that RBSPICE-A observed a 10-80% increase in
1597 the count rates at the microburst times and pitch angles. Figure A.2 shows the ratio
1598 of the RBSPICE-A’s EBR count rates during the four microbursts to the quiet time
1599 one spin before, at the same pitch angles.

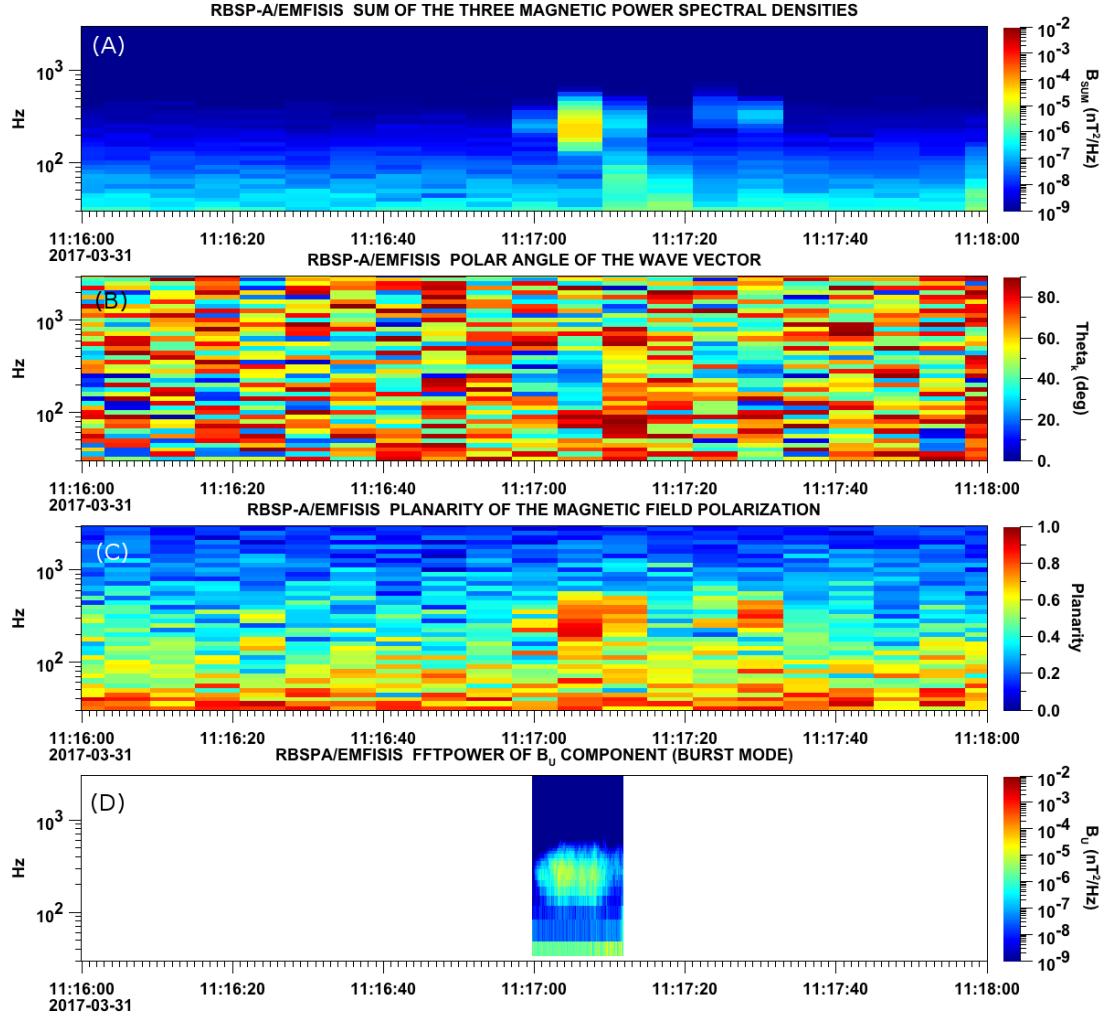


Figure A.1: Panel (A) shows the magnetic power spectral density as a function of frequency and time from the EMFISIS WFR instrument on board RBSP-A. The “hiss-like” wave used for the resonant diffusion analysis was observed starting at 11:17:03 UT. In the same format as panel (A), panel (B) shows the polar angle of the wave vector for this time period. The wave of interest had a normal wave vector, $\theta_k < 30^\circ$. Since the results in panel (B) are valid only for high planarity, panel (C) shows planarity in the same format as panels (A) and (B). The wave of interest was found to have a planarity of > 0.8 . Lastly, panel (D) shows the available burst mode data.

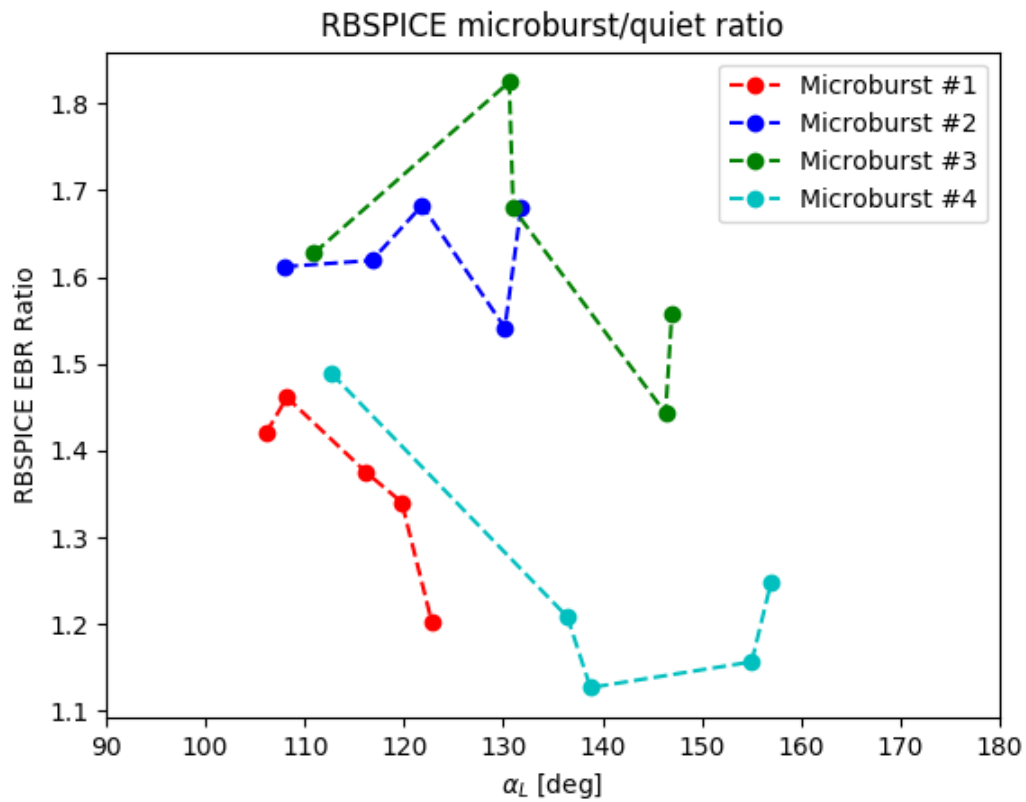


Figure A.2: Ratio of the RBSPICE EBR at microburst times indicated with the black vertical arrows in Fig. 2, to the EBR at the same pitch angles one spin prior (quiet time). The microburst flux was enhanced by 10-80% across $100^\circ < \alpha_L < 160^\circ$ PA, and appear to be peaked closer to $\alpha_L = 90^\circ$.

1600

APPENDIX: APPENDIX B

1601
1602

This appendix describes the method we used to calculate the time difference and separation between FU3 and FU4 at 06:12 UT on February 2nd, 2015.

1603

Time and position correction1604
1605

We used the following method to calculate the clock difference, δt_c and separation, d between FU3 and FU4 at 06:12 UT on February 2nd, 2015.

1606
1607
1608
1609
1610
1611
1612
1613

The relative clock difference was calculated with a cross-correlation time lag analysis on uniquely-identified trains of microbursts that hit both spacecraft simultaneously. Four time periods with coincident microbursts were hand-picked on February 2nd, 2015 and are shown in Figs. B.1-B.4, panels (a) and (b). The cross-correlation time lag analysis was applied to the HiRes time series in panels (a) and (b), and the resulting normalized cross-correlation coefficient as a function of time is shown in panel (c). To validate the peak lag identified in panel (c), FU3's time series was shifted by that lag and is shown in panel (d).

1614
1615
1616
1617
1618
1619

The clock differences from the simultaneous microbursts in Figs. B.1-B.4 were linearly fit to account for the relative clock drift (≈ 20 ms/hour at this time), giving a value of $\delta t_c = 2.28 \pm 0.12$ s at the time of the microburst analyzed here. This time shift was applied to the HiRes data in Fig. 1. A clock difference of $\delta t_c = 2.45^{+0.51}_{-0.98}$ s was independently calculated with the FIREBIRD-II telemetry beacon time stamps that were downlinked during operational passes.

1620
1621
1622
1623
1624
1625
1626
1627
1628
1629
1630
1631
1632

We calculate the spacecraft separation, by applying same the cross-correlation time lag analysis on structures assumed to be spatial and are shown in Figs. B.5 and B.6. The lag from the peak cross-correlation between these events is a sum of the clock difference and time lag due to the spacecraft separation. We interpret the time lag due to the spacecraft separation as the time difference between when the leading satellite observed a stationary spatial feature, to when the trailing satellite observed the same stationary spatial feature. With the method described above, we find the spatial time lag to be $\delta t_d = 2.64 \pm 0.12$ s (after we account for the clock difference and its uncertainty). To convert from a spatial time lag to a spacecraft separation, we calculate the satellite velocity. We calculate the velocity using a Two Line Element (TLE), a data format containing the orbit parameters that are used for orbit propagation. With the TLE derived spacecraft velocity, $v = 7.57$ km/s, the spacecraft separation was $d = 19.9 \pm 0.9$ km.

1633
1634
1635
1636

An independent method to calculate the spacecraft separation was developed. The separation was calculated using TLEs. The TLE from February 2nd was anomalous and was not used in this analysis. Instead, seven TLEs released up to five days after the microburst event were backpropagated, using the SGP-4 algorithm

1637 (Hoots and Roehrich, 1980) that calculates orbital state vectors with perturbations
1638 such as Earth's atmosphere, as well as gravitational effects from the moon and sun.
1639 Then the predicted spacecraft separations at the time of the microburst event were
1640 averaged to derive a separation of $d = 18.4 \pm 1.5$ km. These two methods give
1641 similar separations, which implies that the stationary event assumption used in the
1642 cross-correlation time lag analysis is reasonable.

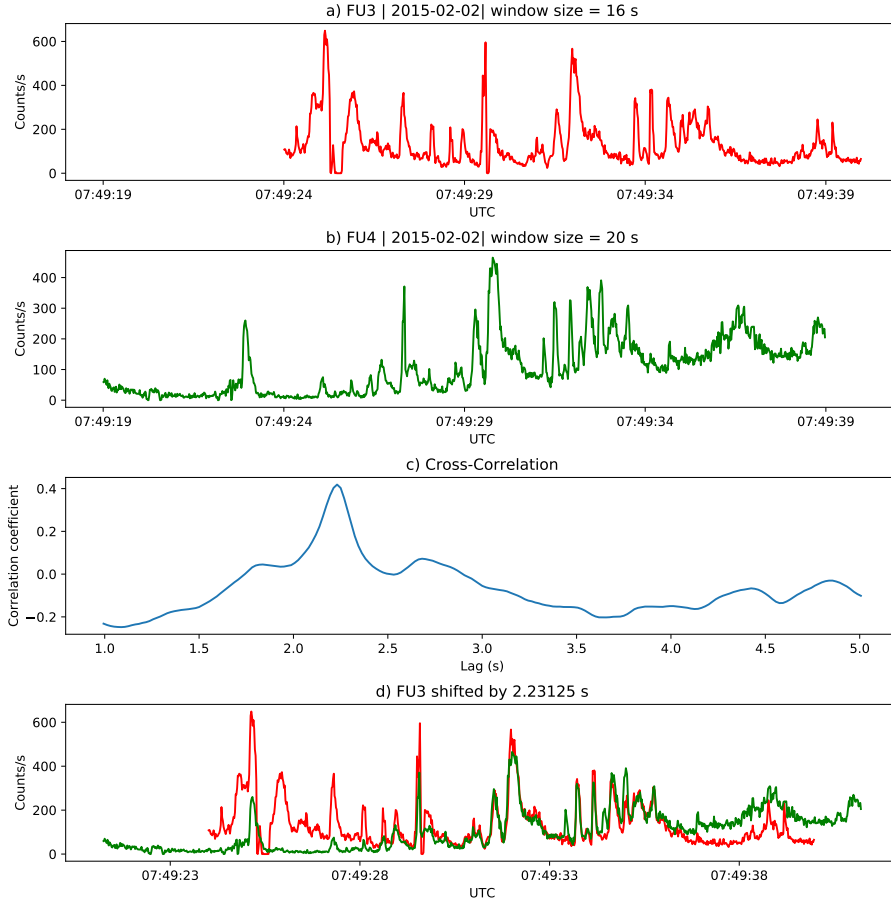


Figure B.1: Cross-correlation time lag analysis applied to a train of microbursts. Panel (a) and (b) show the count rate from the lowest energy channel. Panel (c) shows the cross-correlation coefficient as a function of time lag. Panel (d) shows the shifted timeseries. Clock difference was 2.23 s.

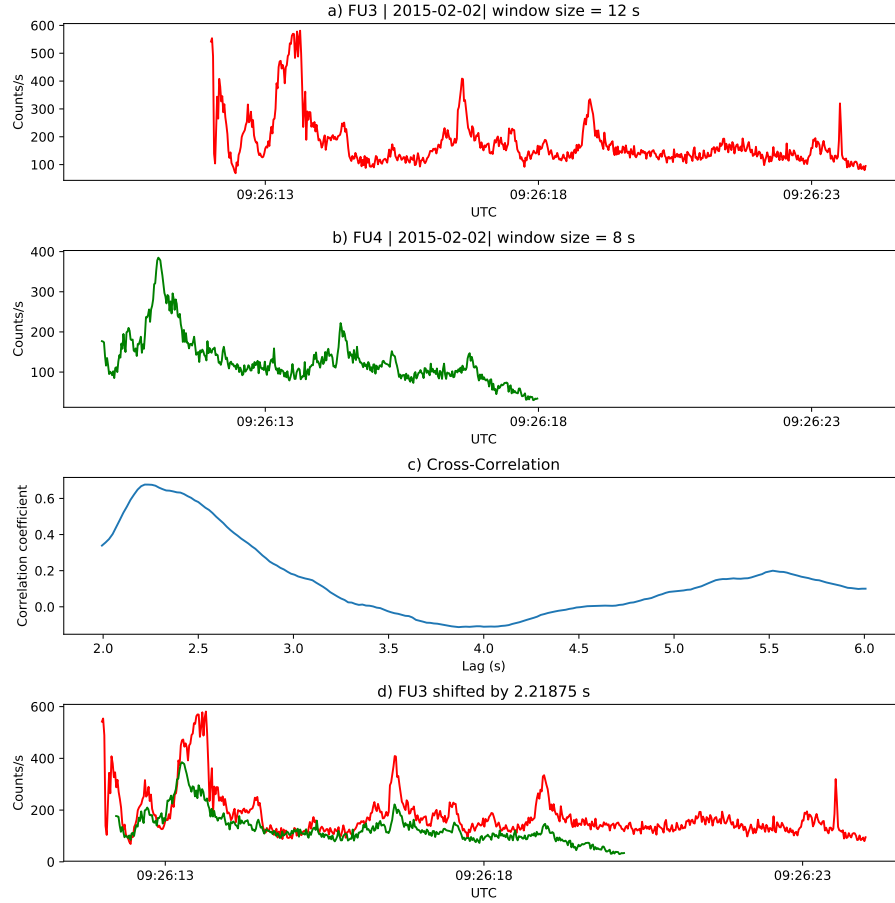


Figure B.2: Same analysis as Fig. B.1 on a different time period. Clock difference was 2.21 s.

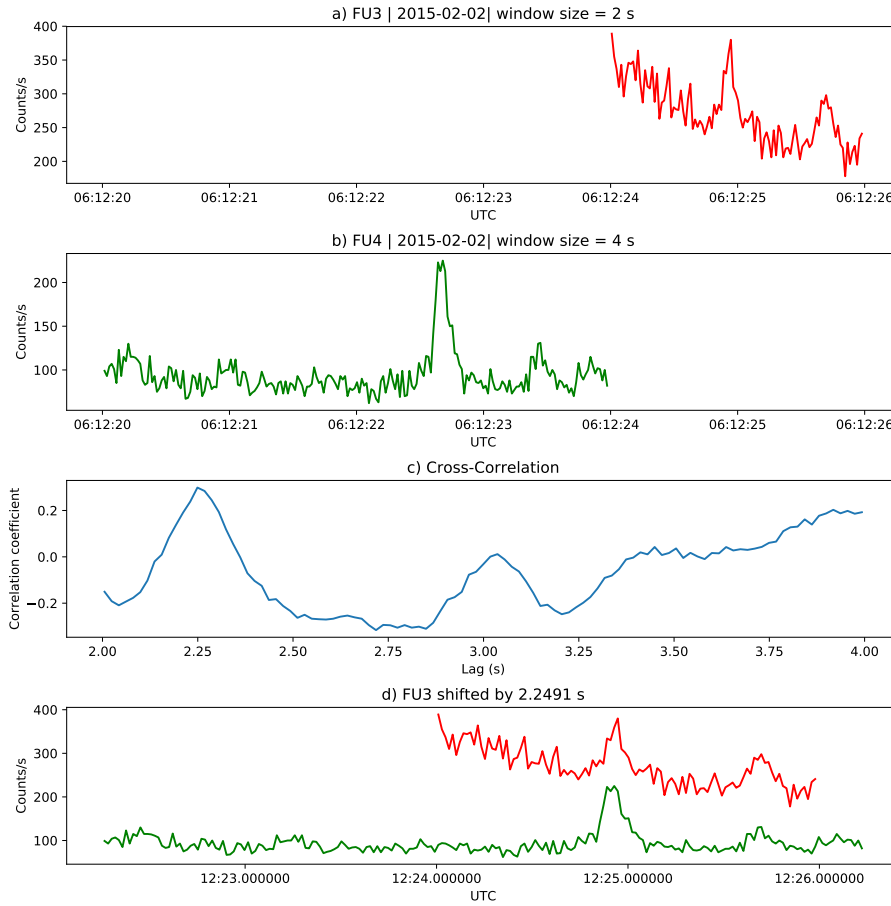


Figure B.3: Same analysis as Fig. B.1 on a different time period. Clock difference was 2.25 s.

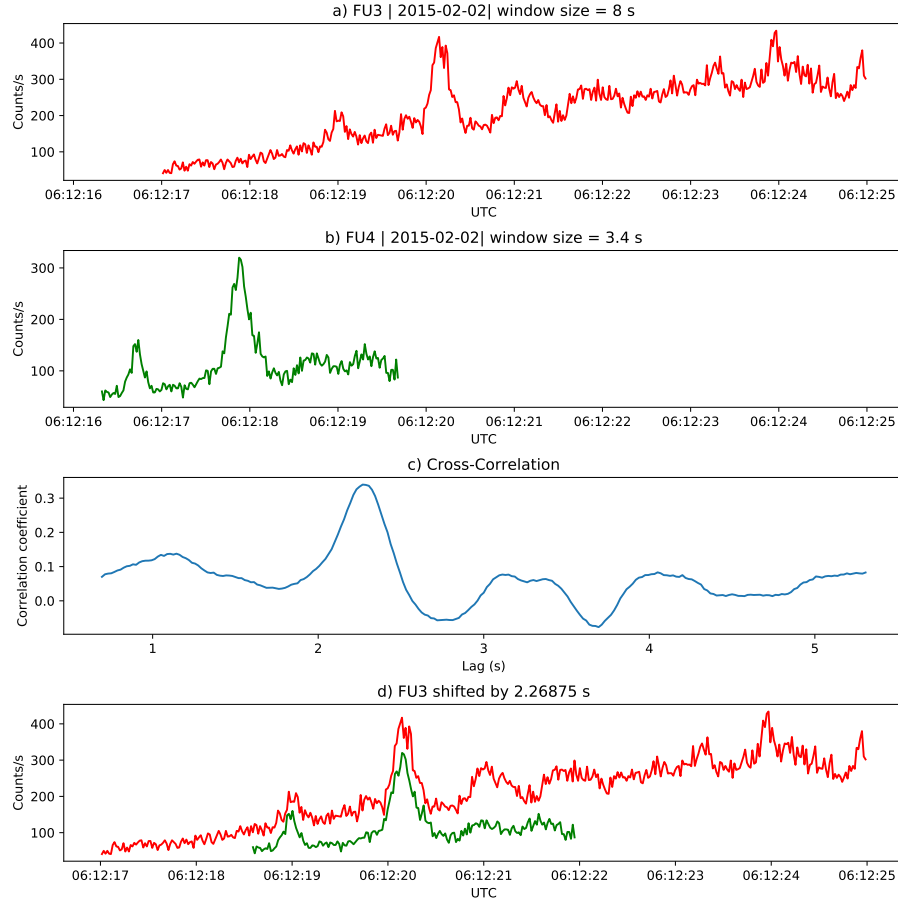


Figure B.4: Same analysis as Fig. B.1 on a different time period. Clock difference was 2.27 s.

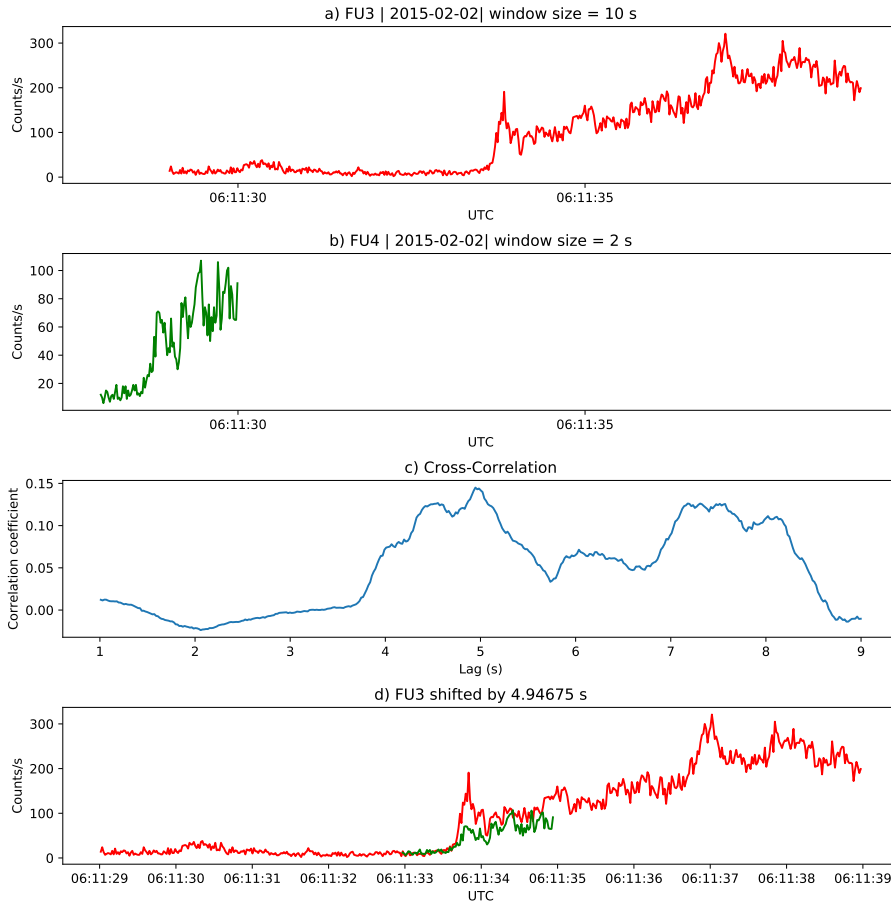


Figure B.5: Same cross-correlation time lag analysis applied to stationary spatial structures. The cross-correlation lag between these events is a sum of the clock difference and time lag due to the spacecraft separation. The lag derived at this time was 4.95 s.

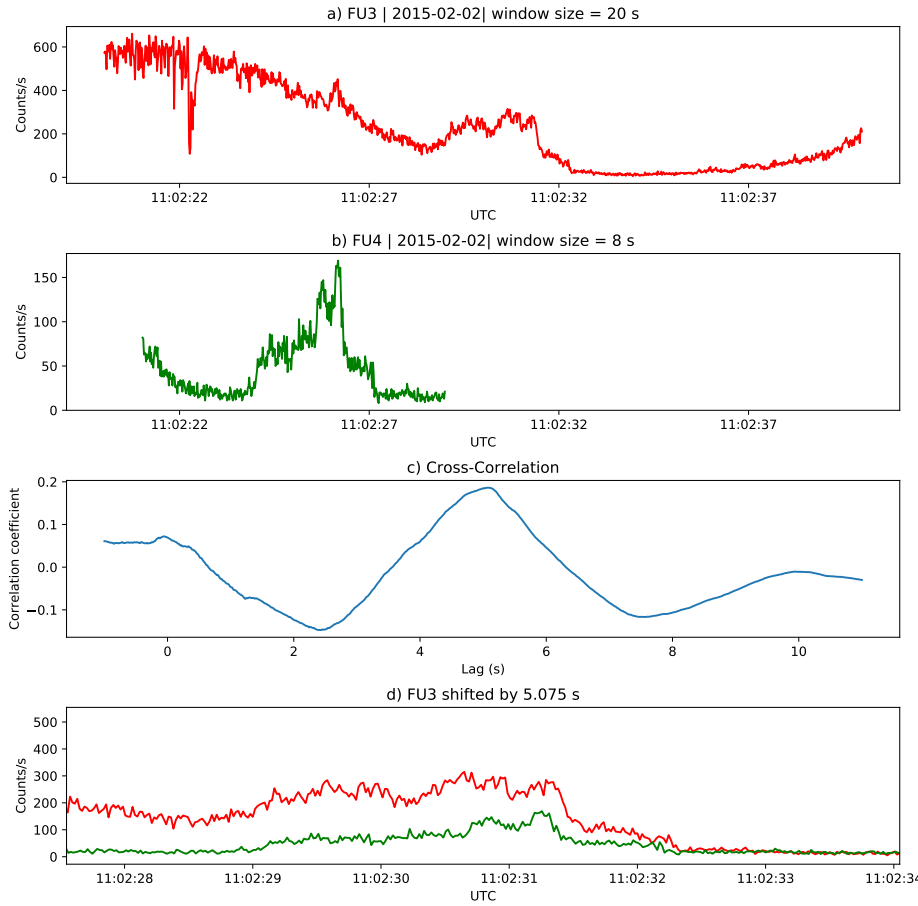


Figure B.6: Same analysis as Fig. B.5 applied to a different stationary spatial feature. The lag derived at this time was 5.01 s.